**Final Report
COVER PAGE**

Federal Agency to which Report is submitted: DOE EERE – Wind & Water Power Program

Recipient: General Electric Global Research Center
Award Number: DE-EE0001367
Project Title: Wind Turbine Manufacturing Process Monitoring
Project Period: Dec, 2009 to September, 2011

Principle Investigator:
Waseem Faidi, Ph.D.
General Electric Global Research Center
1 Research Circle, Niskayuna, NY 12309 (518-387-7095)
faidi@research.ge.com

Report Submitted by:
Waseem Faidi, Ph.D.
General Electric Global Research Center
1 Research Circle, Niskayuna, NY 12309 (518-387-7095)
faidi@research.ge.com

Date of Report: October 31, 2011
Covering Period: Dec 1, 2009 to September 30, 2011
Report Frequency: Final

Working Partners:
University of Michigan
Anthony M. Waas, Professor
3044 FXB, Aerospace Engineering Department, University of Michigan, Ann Arbor, MI 48109
(734-764-8227)
dcw@engin.umich.edu

University of Delaware
Suresh G. Advani, George W. Laird Professor
Associate Director of Composite Center
Mechanical Engineering Department, University of Delaware, Newark, DE 19716 (302-831-8975)
advani@udel.edu
Oak Ridge National Lab
Bob Norris
Polymer Matrix Composites Group Leader
Box 2008, MS 6053 (Mail), 1 Bethel Valley Road, Bldg 5800, Room A-103, Oak Ridge, TN
37831-6053 (865-576-1179)
norrisrejr@ornl.gov

Cost-Sharing Partners: General Electric Global Research Center

Contacts:
B.J. Malloy
Contract Administrator
1 Research Circle, Niskayuna, NY 12309 (518-387-7850)
malloy@crd.ge.com

DOE Project Team: DOE HQ Program Manager – Jose Zayas
DOE Field Contract Officer – Pamela Brodie
DOE Field Grants Management Specialist - David Welsh
DOE Field Project Officer – Nick Johnson
DOE/CNJV Project Monitor – Shaun Jensen

X _____

Waseem Faidi, Ph.D.
Manager, Nondestructive Evaluation Lab

ACCOMPLISHMENTS

Project Objective:
To develop a practical inline inspection that could be used in combination with automated composite material placement equipment to economically manufacture high performance and reliable carbon composite wind turbine blade spar caps. The approach technical feasibility and cost benefit will be assessed to provide a solid basis for further development and implementation in the wind turbine industry.

Project Goals:
The program is focused on the following technology development
- Develop in-line monitoring methods, using optical metrology and ultrasound inspection, and perform a demonstration in the lab. This includes development of the approach and performing appropriate demonstration in the lab.
- Develop methods to predict composite strength reduction due to defects
- Develop process models to predict defects from leading indicators found in the uncured composites.

Goal Status:

Task 1 Inline Inspection

Task 1.1 Optical metrology for fiber waves detection
The focus of this task is to develop a method to detect defects formed during the lay-up of carbon composites. The system is designed to generate real time data related to the structure of the lay-up, which can be used for process control, or quality monitoring. This task targets detection out of plane wrinkles of height of 0.5 mm or greater and in-plane wrinkles.

A system consisting of a laser line and smart camera to generate three-dimensional measurements for out-of-plane wrinkle detection and white-light for conventional two-dimensional photography for in-plane wrinkle and other surface-related features detection, see Figure 1. The system was, first, built and tested in the lab using a two-dimensional scanner to simulate an automated carbon composites manufacturing machine. Next, an appropriate automated manufacturing machine which has been developed under internal GE efforts at GRC – Munich was identified to provide an additional opportunity. The optical scanner system packing and controls were modified to enable its integration to the GRC – Munich machine. The reduced footprint of the three-dimensional system required lens and laser optics changes. The 8-mm camera lens has a large amount of "fish-eye" distortion to be corrected. Without the correction, a flat plate would look more like a bowl in three-dimensional space. Correction results are shown in Figure **2**. The correction look up table (LUT) is loaded into the camera for improved performance. Then, the modified system was tested in the lab using manually laid up uncured carbon composites plies.
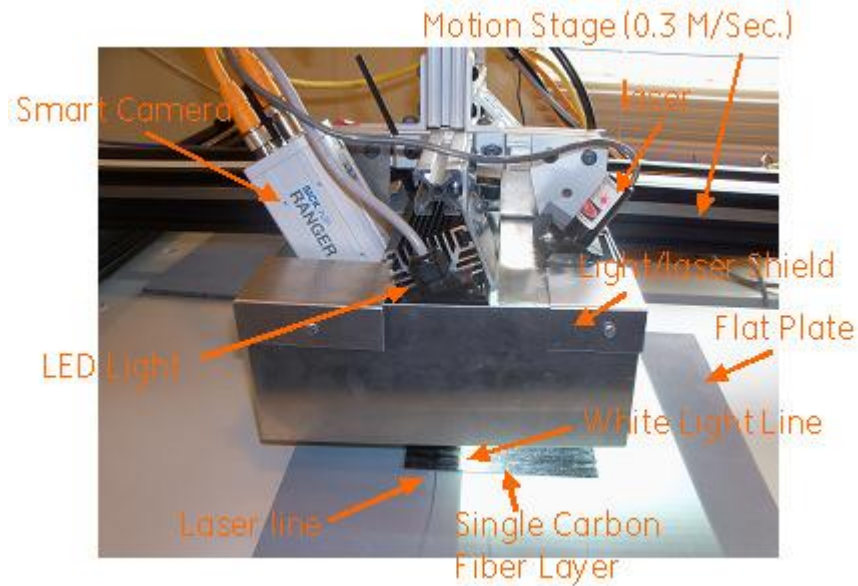
Figure 1   Multi-scan camera, LED light, and laser with light shield

Figure 2   Camera and laser distortion correction results

Finally, the scanner was installed and integrated to the GRC – Munich machine and eight 7-m long layers of carbon composites material were laid down. Artificial defects were placed between three different layers; see plan is in Figure 4. The defect consisted of wires, washers, and spheres of different sizes and insertion locations. Measurements were performed during the lay-up as well as on a section of the laid-up sparcap after it were cured. The collected data was processed generating the images in Figure 5.
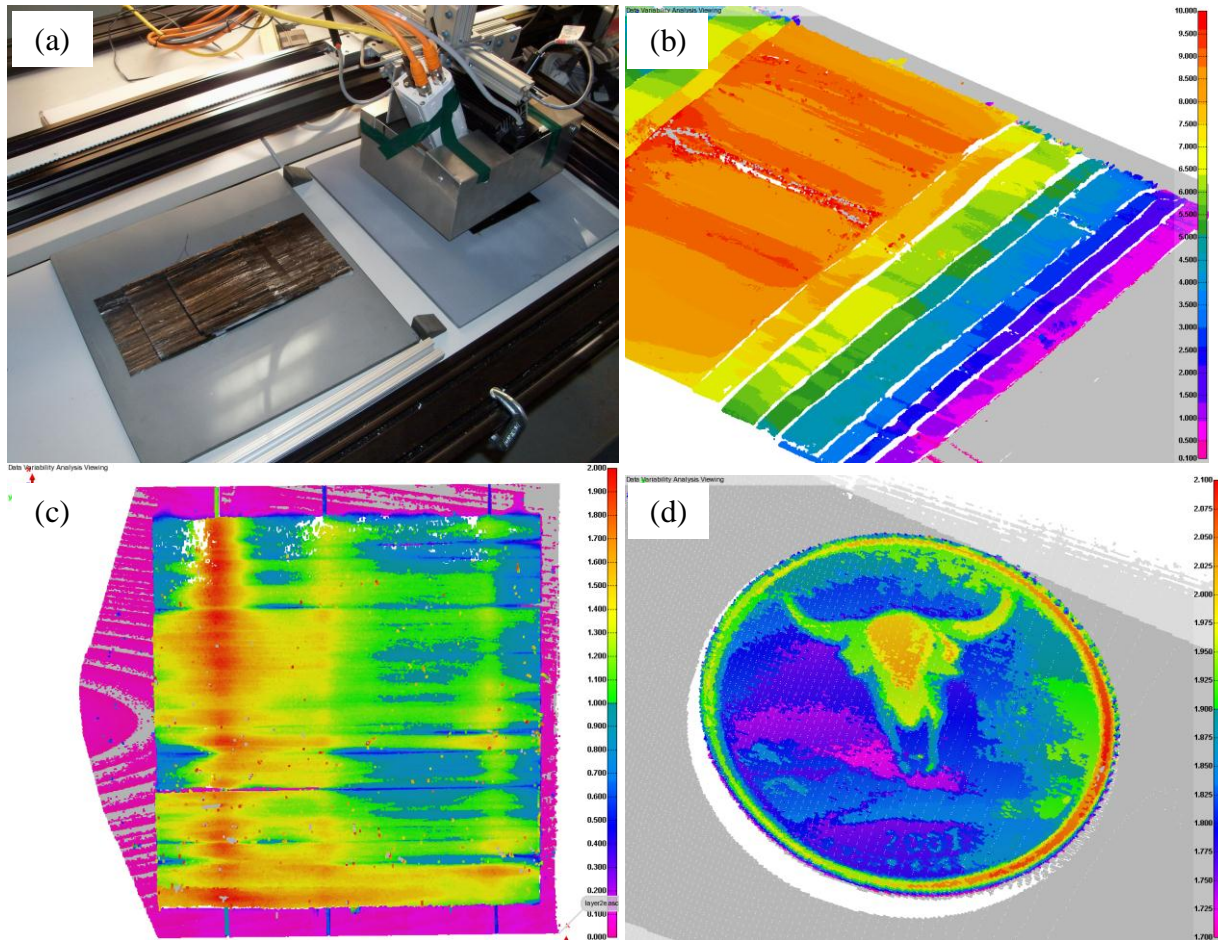
Figure 3   (a) Manual lay-up testing using the lab scanner, and images of (b) ply drops showing a sub-mm resolution capability, (b) AWG22, 26,30 wire inserts simulating out-of-plane wrinkles, and (d) a quarter dollar showing features in the order of a 100 microns.

Few observations were made, the uncured material intrinsic surface variation were large and prevented the detection of the smallest defects. For example, the 0.5-mm and 0.81-mm wires were detected easily in the cured section, where the surface variations were small, but only the 1-mm diameter wires were detected in the uncured materials, see Figure 6. Additionally, the wrinkle from that 1-mm diameter large diameter wire appeared two layers later, indicating a lift-off in the material immediately after lay-up. The wire was inserted before Layer 1, but was not visible until Layer 3 (Figure 5). This also explains why it was not visible in Figure 6. The washer and sphere defects had similar delayed visibilities.

As for the two-dimensional measurement, several algorithms were tried to detect defects in the, all of which required common image processing (i.e. Selecting the region of interest ,Figure 7).

Adaptive Thresholding (Figure 8): Computes the local standard deviation of the image by processing it by blocks of given size, then apply an empirical threshold to decide whether the

block is homogeneous (background) or inhomogeneous (defect). Each block then takes the value 0 or 1 to create a binary map of the defects. This is the technique we have selected for

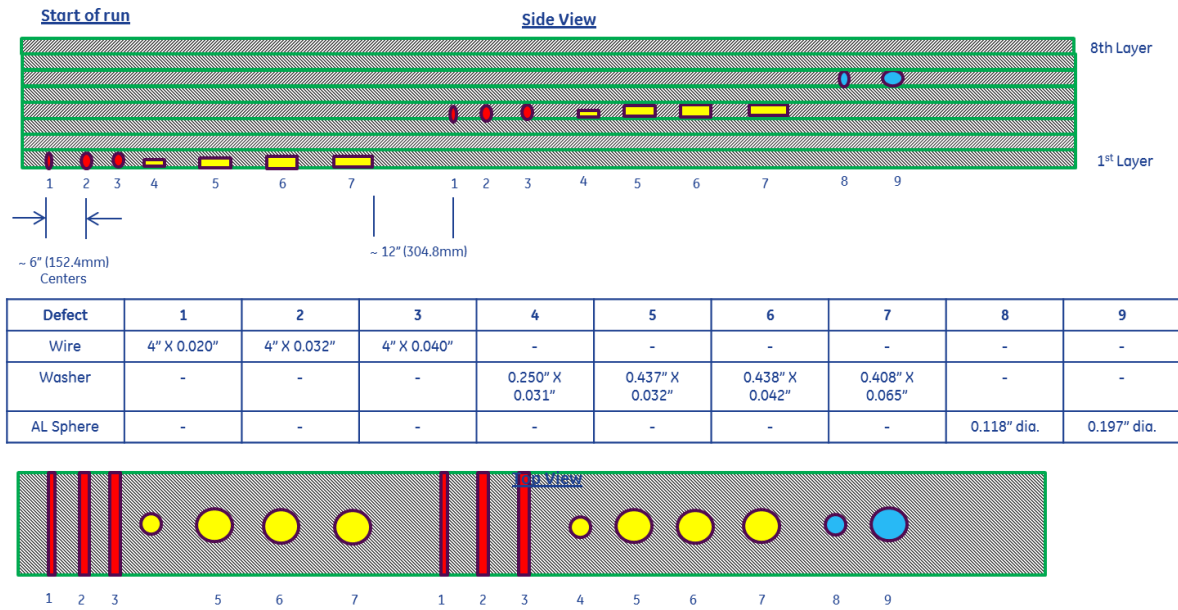| Defect	1	2	3	4	5	6	7	8	9
Wire	4" X 0.020"	4" X 0.032"	4" X 0.040"	-	-	-	-	-	-
Washer	-	-	-	0.250" X 0.031"	0.437" X 0.032"	0.438" X 0.042"	0.408" X 0.065"	-	-
AL Sphere	-	-	-	-	-	-	-	0.118" dia.	0.197" dia.

Figure 4   Defect type, size, and placement plan
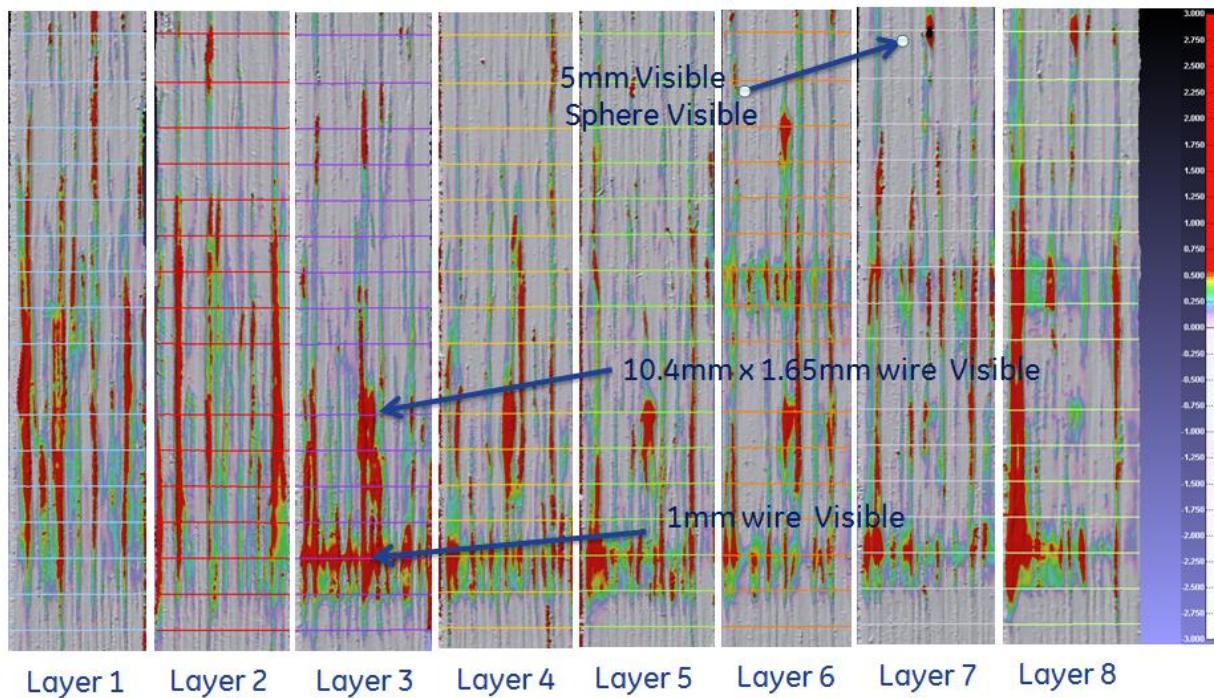

Figure 5   Detection of inserted flaws at each layer in the uncured materials
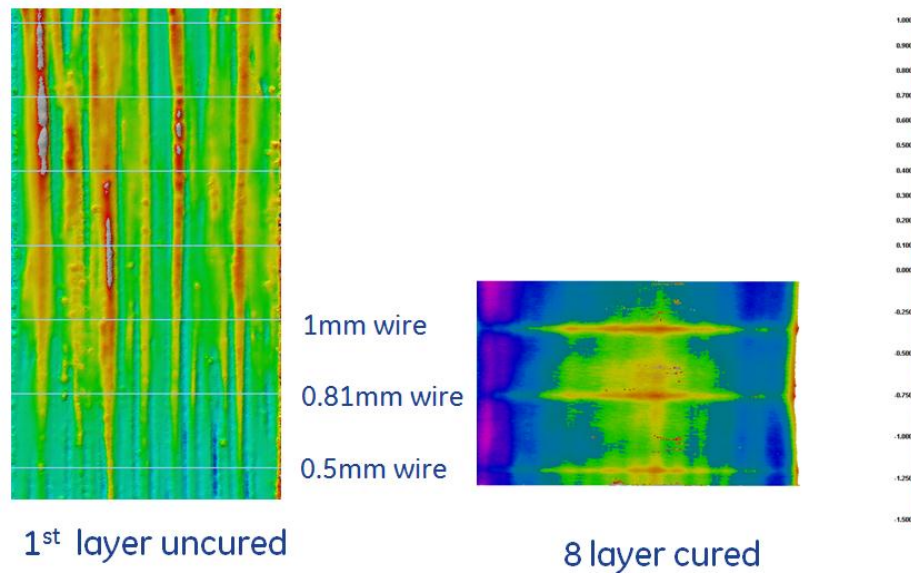
Figure 6   Artificial wrinkles created with different size wires in cured/uncured parts

this problem. The size of each block in the image is 8x8 pixels, but the standard deviation calculation is done on a 16x16 pixels patch in order to smooth the output result.

Local entropy: the standard deviation calculation was replaced with a local entropy calculation. The results were not as good as expected due to a low SNR.
Fractal encoding: fractal encoding is a self-similarity technique that tries to represent an image with a set of texture patches extracted from the same image or from another image. A modification of the algorithm allows also finding all unique patches present in the image, patches that can be used to reconstruct the image. The idea behind that is to find patches containing a defect since they will have a unique pattern.
Weibull features: consists of computing two parameters of a Weibull fit for the distribution of image gradients in local regions, and apply a classifier to distinguish between background and defects. This algorithm should work very well if the contrast defect/background was a little bit better.

Under a GE internal effort, the hardware will be updated to use the more precise machine motor encoders (instead of the compaction roller encoder) and then image a sub-scale sparcap during lay-up.
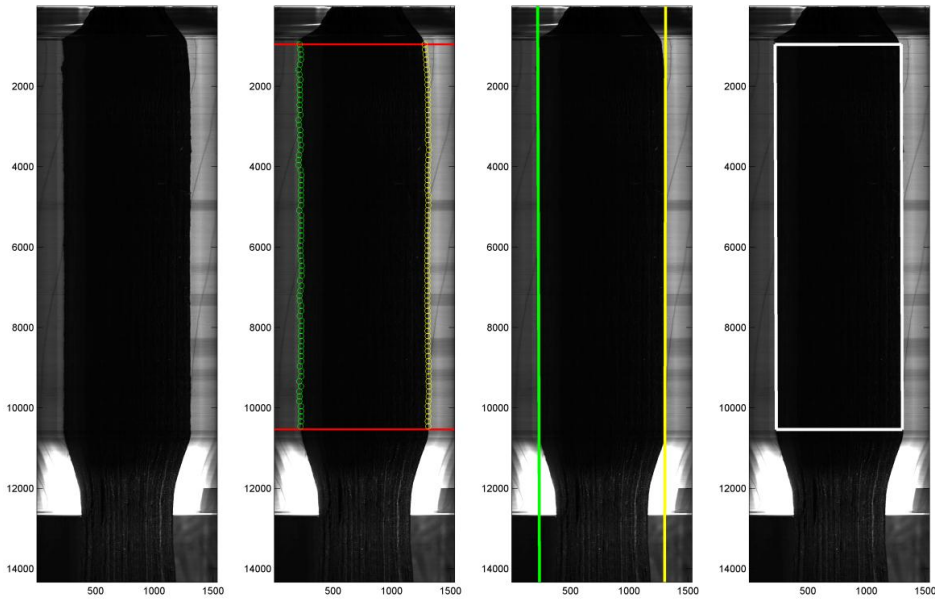
Figure 7   Extracting the region-of-interest: (from left to right) original image, selection of upper and lower limits marked in red and computation of the local edges, approximation of the edges with lines, computation of the maximal rectangle fitting the selected polygon.
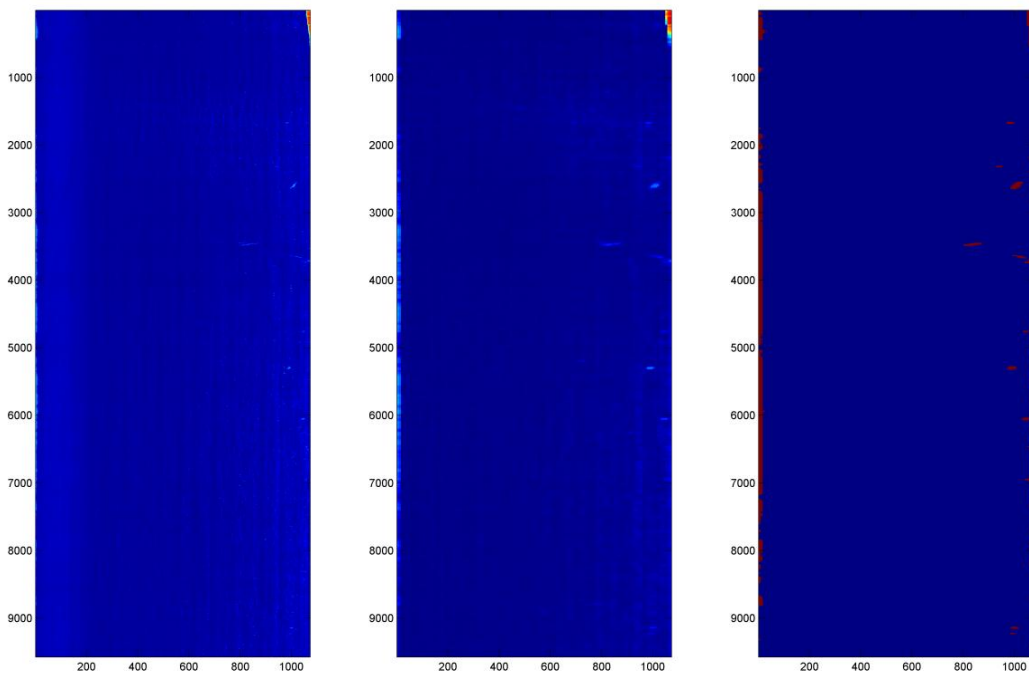

Figure 8   Abnormalities identification: (from left to right) original image, image of local standard deviations, binarization using a threshold selected per experimentation

Task 1.2 Ultrasound for porosity and delaminations detection
The scope of this sub-task is to develop noncontact ultrasound measurement to assess the quality of the uncured composite tape before it is laid-up. A team exercise was carried out to identify the potential failure modes of the impregnation process in order to assure that control process are in place for them. As an outcome to the exercise, variations in the resin content was identified as the potential risk that ultrasound would help control.

Initially, submersed ultrasound measurements were done on an uncured carbon composites specimen. In order to support the specimen during the measurements and to prevent water from infiltrating into the specimen, the specimen was placed on an aluminum plate and vacuum bagged before submerging in the water tank. The scans were done using three 1-MHz ultrasound probes of different focusing characteristics, namely, focused with F number (probe focal length to diameter ratio) of 3, flat, and focused with F number of 2.6 The reflected ultrasound signal from the backwall of the aluminum plate were gated to generate c-scan images of the specimen. Figure 9 shows the s-can images obtained using the three probes. As shown in the figure, the ultrasound signal transmitted through the specimen varied spatially indicating variations in the compositions of the specimen. These variations were primarily identical in the images generated using the three probes.

1MHz F/3 (F=3", dia=1")   1MHz flat (dia=1")   1MHz F/2.6 (F=2", dia=0.75")
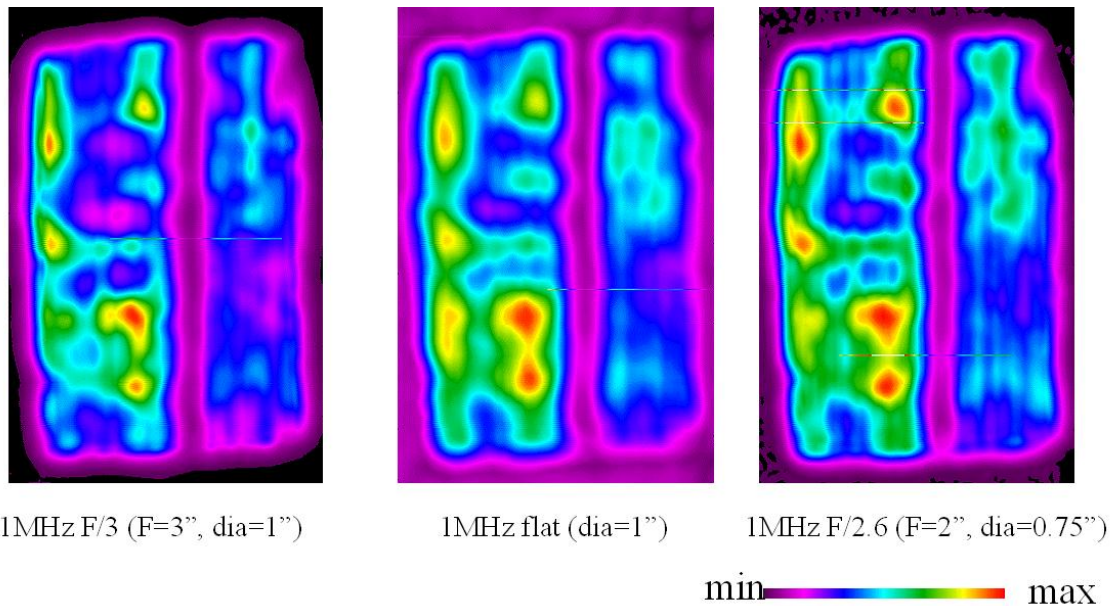
Figure 9   Ultrasound c-scans of the uncured carbon composite specimen with three different ultrasound probes

Next, the specimen was cured under nominal curing conditions and scanned with ultrasound again. Since the cured specimen could sustain its own weight, it was not mounted directly on the aluminum plate, instead was placed on stand-offs above the

plate. In this case, the front wall signal of the aluminum plate was gated to generate the c-scan images shown in Figure 10. The majority of the special variations observed in the uncured specimen (Figure 9) disappeared after the specimen was cured (Figure 10). However, the vertical line seen in center of the uncured specimen persisted to a significantly less degree after curing. One plausible explanation is that the line represented a resin poor region that led to higher porosity in the cured part.

1MHz F/3 (F=3", dia=1")   1MHz flat (dia=1")   1MHz F/2.6 (F=2", dia=0.75")
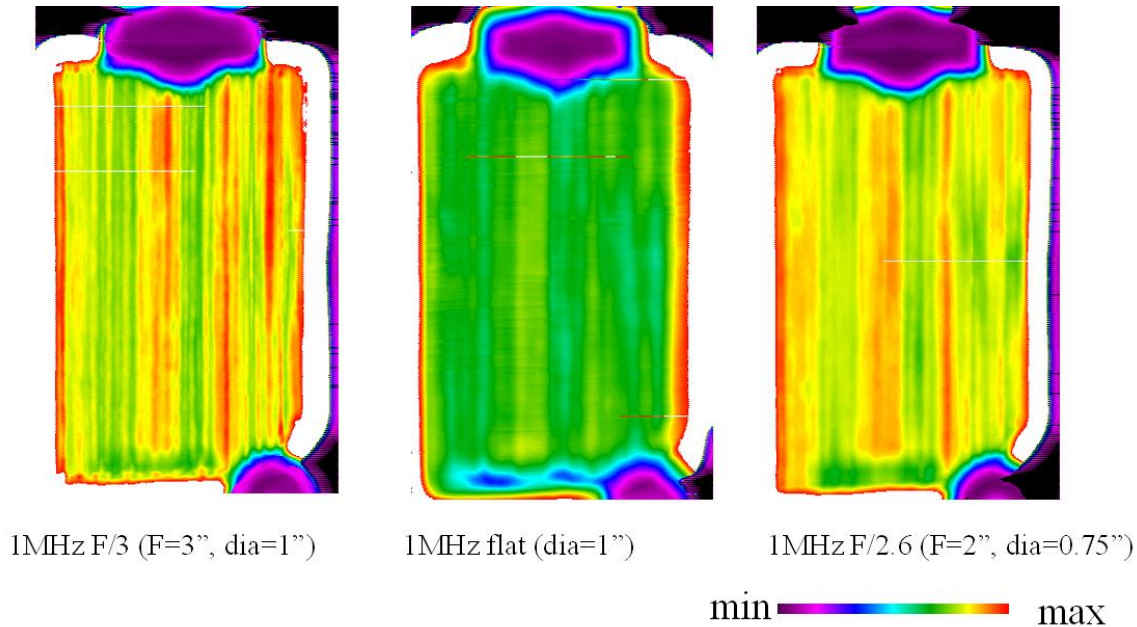
min ▬▬▬▬▬ max

Figure 10   Ultrasound c-scans of the cured carbon composite specimen with three different ultrasound probes

Then, a through-transmission ultrasound measurement system was developed, which could potentially fit on the automated carbon manufacturing machine in GRC Munich. This included two main developments, namely, designing the ultrasound probe to provide the required sensitivity to the tape resin content, and making the instrumentation compact so that it could be integrated to the machine. Utlran Group, the supplier for the ultrasound probes used in the bench top experiments, was contacted to help with the probe development effort. A design was reached to use a single transmitter probe and array probe as a receiver to cover the tape width, as Shown in Figure 11. Figure 12 shows the receiver probe. Instead of the four active elements, shown in blue, the transmitter probe will have one big active element.

Carbon composites samples with three different resin contents were made, namely, 20%, 35%, and 40%, using the automated carbon manufacturing machine. The samples were shipped uncured and measured using the bench-top ultrasound system. The probes used were air-coupled 1-inch diameter, 350 kHz. The signal amplitudes are

shown in Figure 13.For each resin content, ten points we were measured on two 100 × 150 mm samples.
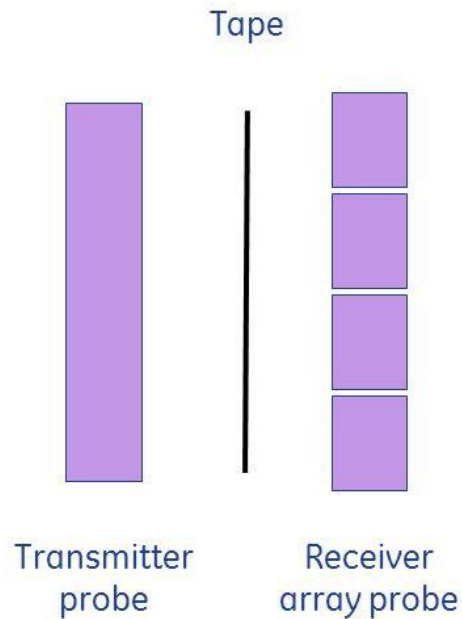

Figure 11   Through Transmission ultrasound probe schematic
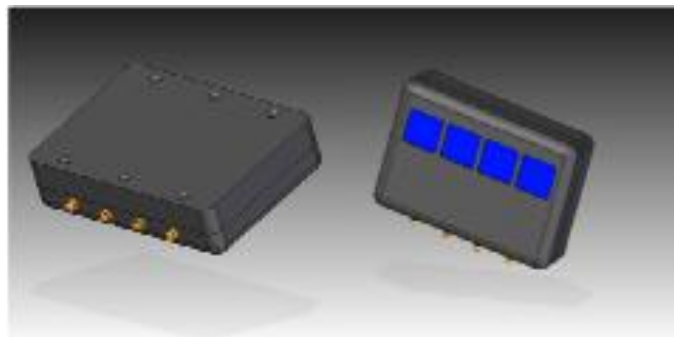

Figure 12   Front and back of the receiver air-couple ultrasound probe

The measurements were also repeated at higher temperatures, namely at 40 and 50 °C, to simulate the conditions in the automated manufacturing environment. The measurement for both elevated temperature cases were similar. The 40 °C case results are shown in Figure
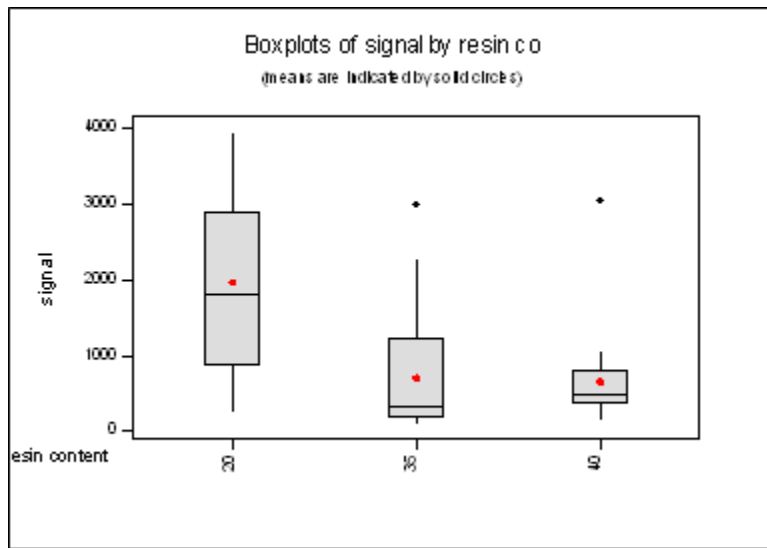
Figure 13   Signal amplitude of the transmitted ultrasound signal of the three different resin content samples (kHz)
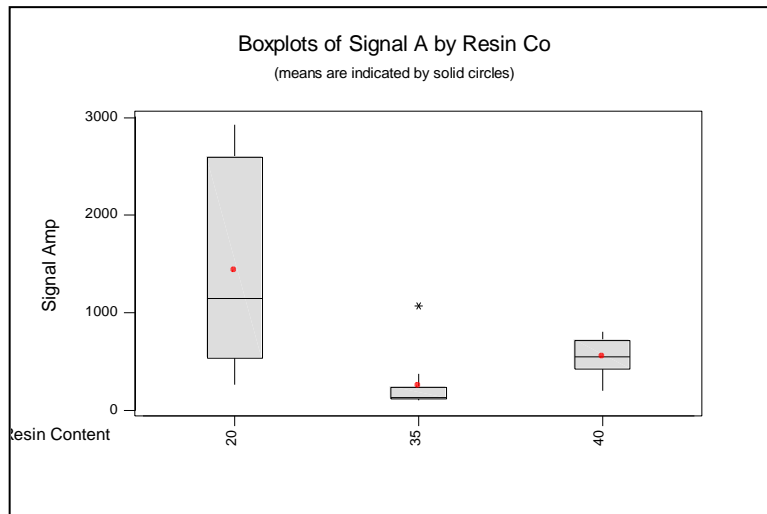

Figure 14   same as Figure 13, except that the measurements were done at 40 °C.

The installation of the ultrasound system on the GRC – Munich machined was not completed due to delays in specific machine components. However, the team was able to test the ultrasound measurement system using a simpler set up on site at GRC – Niskayuna. The set up consisted of a smaller tape, and so modifications had to be made on the ultrasound probes to enable the test. The measurements from that set-up showed similar trends as the ones observed in the bench top tests. Tests on the GRC-Munich machine will be performed later under a GE internal effort.

Task 2 Effects of Defects

Wind turbine blades are one of the largest structures being built primarily out of fiber reinforced composites. The increasing blade length for higher energy capture and ever increasing need to get lighter will increase the usage of advanced composites in the wind blade. Reliability requirements make it necessary that we understand the impact of various manufacturing process defects on the ultimate material strength of fiber composites for the design limiting load case of compression loading. It is well known that fiber composite compressive strength is highly sensitive to fiber misalignments [1-3]. In thick unidirectional (UD) composites fiber waviness could arise during ply layup and curing or due to some manufacturing process deviations. These have been known to cause a significant drop in the compressive strength. This is even more critical for carbon unidirectional composites as carbon composites are typically used in strength limited design applications. So any reduction from the expected strength response of material due to defects can lead to failure of the component [4-10].

The main objective of this task as part of the inline NDE project was to develop failure models for defective carbon composite material parts. Typical defects that have been identified for this purpose are the waves in unidirectional lamina, delaminations and voids in laminates. The GE‐GRC team was collaborating with Prof. Waas at the University of Michigan, Ann Arbor to develop fracture cohesive models for understanding delaminations and also for conducting experiments on wavy defect carbon composite coupons. The modeling for the wavy coupons was developed by the GRC team. The task comprised both experimental and modeling work and a brief description of each is given below in the following sections.

A test plan was developed to understand the impact of waviness in carbon composites under compressive loading. Similarly fracture mode-I and mode-II tests were planned to determine the mode-I and II strain energy release rates. Following is the break down of the experimental space for understanding the wavy defect impact on UD carbon strength in compression and fracture testing to understand the UD carbon material fracture properties.

    I.   Wavy coupon test plan

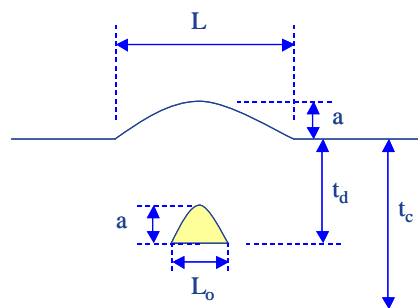Figure 15   Fiber wave defect schematic

The different type of sample needed are described as follows, see Figure 15 for details,
1. Pure resin samples
   a. Tensile test samples of pure resin conforming to ASTM standard or any relevant standard

      b. Compressive test samples
2. Compressive defect coupons
      a. UD coupons with defects of various dimensions
      a/tc = 0.1, 0.15, 0.3; L/a = 4,16,32,48

5 samples for each defect making a total of 60 samples. Inserting a pre-manufactured resin insert into the coupons before the layup will make the defects. The coupons dimensions are 15 mm (thick) by 15 mm (wide) and the coupon length will be the "wavelength of defect" + 10 mm on either side + a grip length.

    II. Cohesive fracture model development and delamination testing

1. Fracture mechanics testing for mode-I and mode-II delamination toughness values in carbon composites as per ASTM standards
      a. # of samples: 5 per test type (total 10)
2. Testing to obtain interlaminar shear strength (3 coupons) or literature if available
3. Develop cohesive zone parameters for the carbon composites
4. Validation

A parametric finite element micromechanical model taking into account the carbon fiber orthotropy was developed to capture the defect wave geometrical parameters. The finite element model consisted of alternating fiber and matrix layers (Figure **16**). The geometry of the wave was modeled using a cosine function. Local coordinate systems were defined along the fiber elements so as to orient the element coordinate systems to be parallel to the material orthotropic coordinate system.

The finite element simulations were conducted using the fully elastic-plastic response of the resin and using non-linear geometry settings. The modified newton-raphson approach was used to simulate the response of the nonlinear model.

Compressive loading simulation of perfectly straight fiber and matrix layers would lead to no limit load type of response. To obtain a limit load under compressive loading, typically the finite element model is given a small perturbation initially and then loaded. The small initial imperfection acts to create a local instability in the fiber/resin layers of the micromechanical model. This leads to a peak load for a given imperfection. In the current modeling the initial imperfection is caused by the presence of the wave as shown in Figure 16.
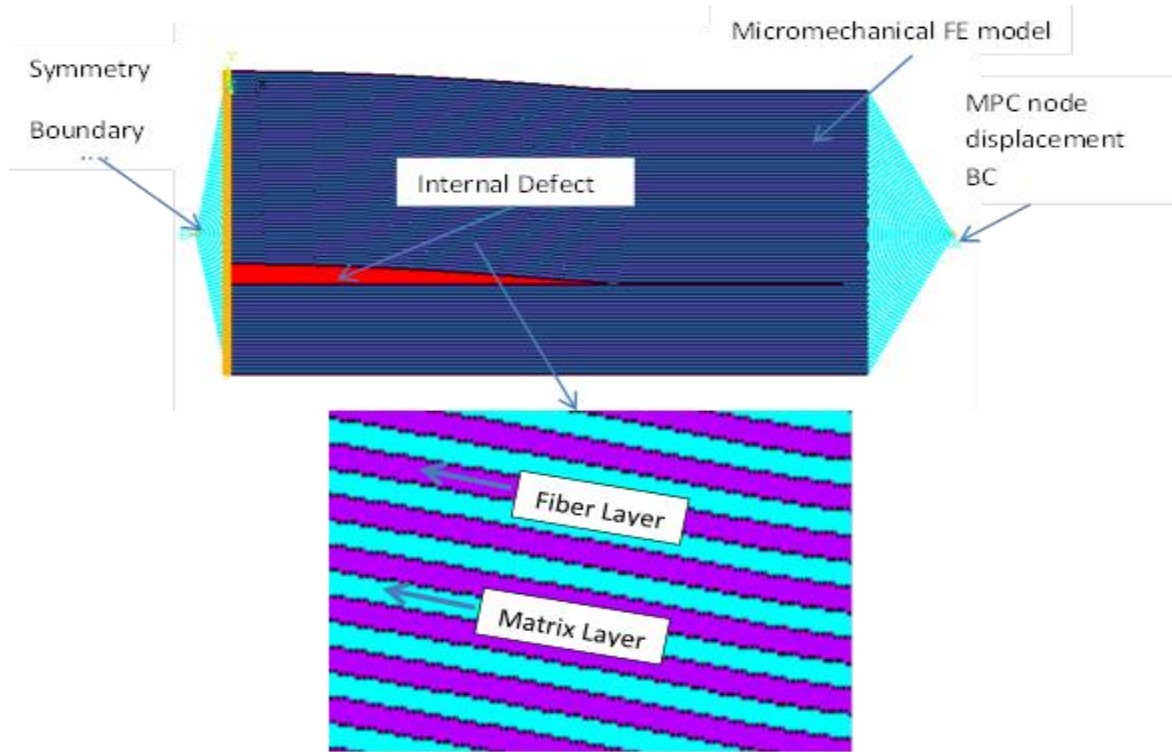
Figure 16   Micromechanical finite element model showing the individual fiber and matrix layers and boundary conditions used in compressive loading simulations.

The test data for both the wavy defect coupons and fracture tests were collated and analyzed. This data was used to validate the models. In the following sections both the cohesive model development and wavy defect modeling results are presented.

I.   Cohesive fracture model development and delamination testing

The fracture mechanics tests were performed on the carbon coupons for pure mode-I and pure mode-II. Mode-I fracture properties were obtained from double cantilever beam tests. The load-displacement response of the different samples and individual strain energy release rates for both DCB and ENF are shown in Figure 17 and Figure 18.
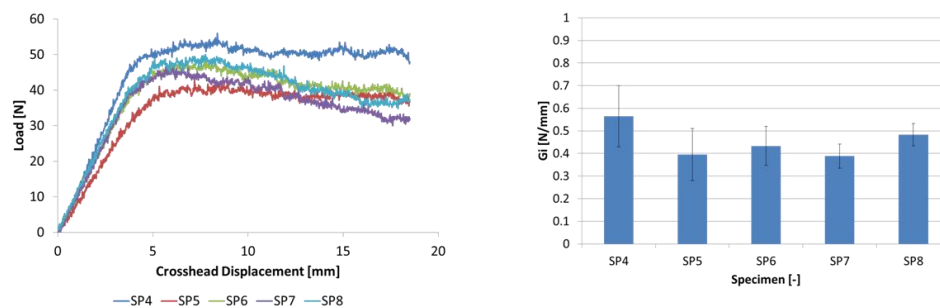

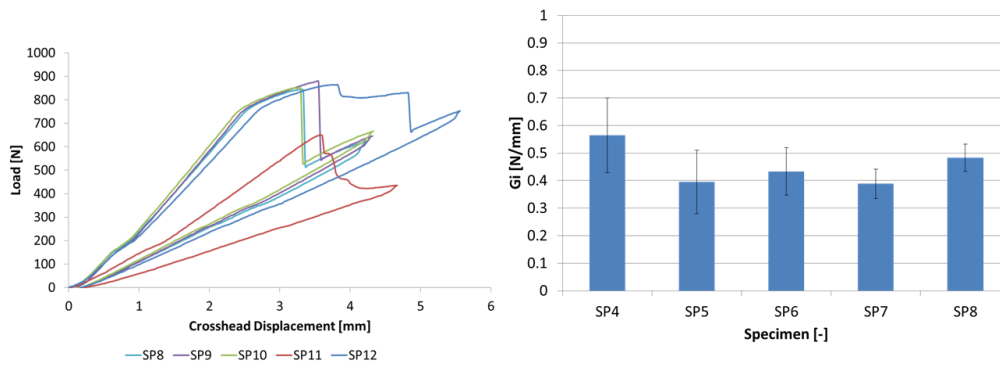Figure 17   DCB test data of carbon coupons

Figure 18   ENF test data for mode-II strain energy release rate values

The average strain energy release rate values and the corresponding standard deviations were calculated for the corresponding modes of fracture and are given in Table 1.

Table 1   Mode-I and mode-II fracture strain energy release rate values for carbon composite

RESULTS	Gi [N/mm]	Gii [N/mm]
Carbon panel (UD)	0.45 +/-0.105	0.63 +/- 0.044

The values of strain energy release rate obtained from the tests for these materials are similar to values obtained for carbon prepreg materials.

For the cohesive model development, DCZM elements were used in ABAQUS at the Univ. of Michigan, Ann Arbor. The mode-I and mode-II strain energy release rates obtained from experiments was used as input to the cohesive model. One of the samples from mode-I and II test data was used to obtain the critical normal stress (σc) and critical shear stress (tc) by matching the numerical simulation peak load to the experimental peak load obtained from coupon testing.

The following cohesive parameters were developed for the carbon composite material tested at the University of Michigan, Ann Arbor.

     –   Gic = 0.45 N/mm | σc = 4.7 MPa
     –   Giic = 0.63 N/mm | тc = 9 MPa

These model parameters were used to simulate the response for remaining coupons and are shown in Figure 19.
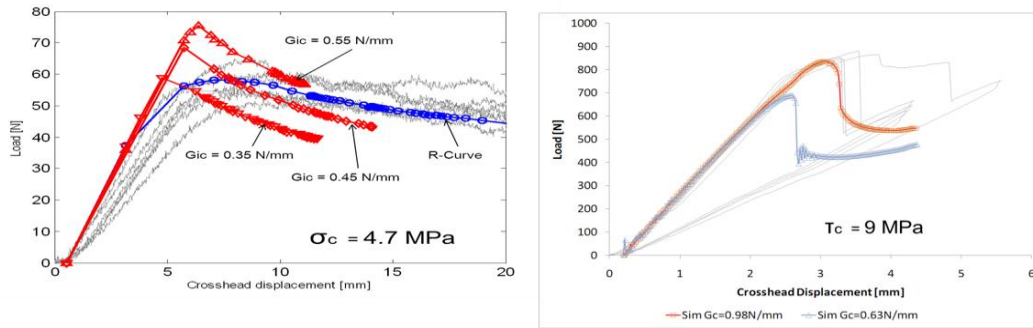
Figure 19   Cohesive model comparison with DCB and ENF test data

II.   Micromechanical modeling and comparison with test data

A parametric finite element micromechanical model taking into account the carbon fiber orthotropy was developed to capture the defect wave geometrical parameters. The results were then validated with test data and used for strength prediction.

A comparison with the model run for a test case with orthotropic fiber properties and isotropic fiber properties is shown in Table 2. The impact of orthotropy is not significant but the peak load is higher than the case of isotropic fiber. However, for further analysis fiber orthotropy will be taken into account, as the carbon fiber being used in the composite coupons is orthotropic in nature.

Table 2   Effect of fiber orthotropy on the predicted compressive peak load using micromechanics

|	Peak Load (N)	Displ (mm)
Ortho	665	0.0127
Iso	683	0.0128

The micromechanics finite element model needs the pure resin stress-strain response as an input to predict the compressive strength. To obtain the response, pure resin testing was done in tension to obtain the stress strain response of the resin system being used in the carbon composites and is shown in Table 3.

Table 3   Pure resin tensile strength and modulus values

Specimen	Area(mm^2)	Failure Stress(Mpa)	Modulus (MPa)
AT_1	55.11	65.08	5213.50
AT_2	55.05	58.58	5245.30
AT_3	55.19	51.61	5251.10
AT_4	54.99	47.14	5402.70
AT_5	54.87	60.09	5028.30
Average	55.04	56.50	5228.18
Std.Dev	0.12	7.12	133.64

The coupons from carbon prepreg material were fabricated with a nominal thickness of 15 mm and wavy defects were introduced using pre-cured resin inserts of specific thickness. Optical speckle based strain measurement technique was used to measure the specimen strain in real-time during testing. In Figure 21a, a typical force-displacement plot is shown, at the peak load point of failure it can be seen that there is localization of strain and near simultaneous splitting of layers. The Figure 21b shows the variation of the peak compressive strength as a function of

the wave defect aspect ratio. The data was normalized with respect to the strength of the shallowest defect coupon (L/a=47.7). The spread in the data points is partially due to the fact that each data point has a slightly different defect height, which also seems to impact the
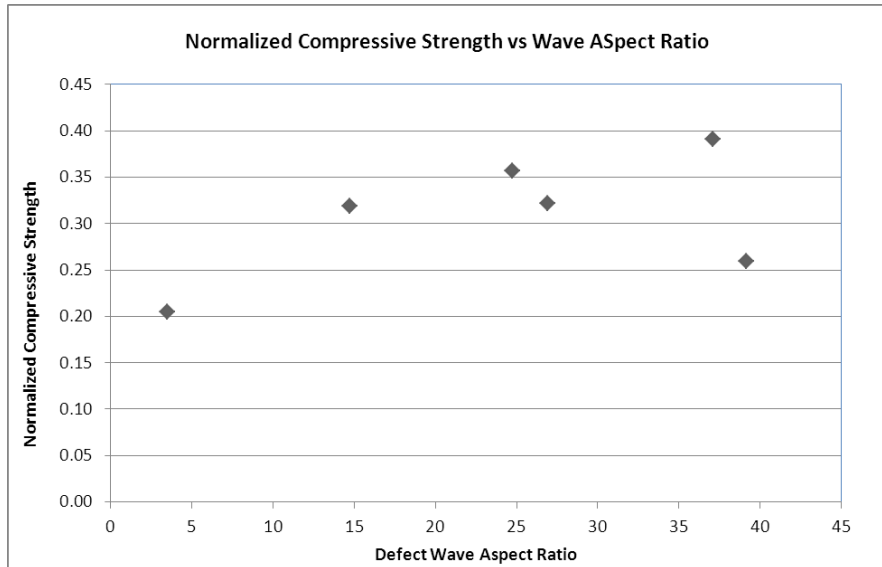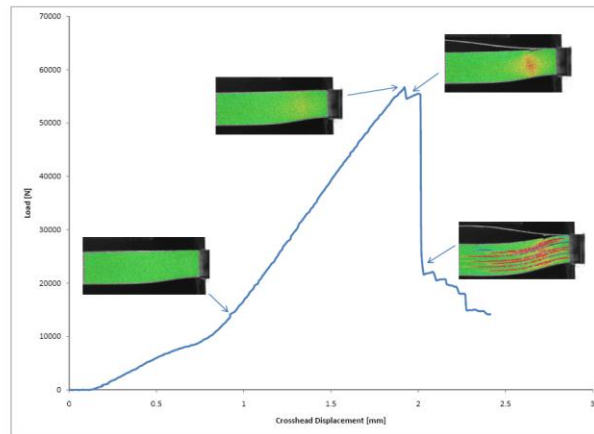

strength.

Figure 20   Typical force-displacement of coupon with corresponding optical strain images at pre-failure and failure and normalized failure stress as a function of wave aspect ratio

The micromechanics model was evaluated for the resin system tested above by changing the defect geometric parameters over a wide range. A DOE was constructed and the numerical model was used to simulate the defects over the range specified in the DOE table.

The model is being analyzed at specific DOE points and a transfer function will be developed relating the compressive strength to the defect geometry. Figure 21 shows the predicted peak compressive strength as a function of the defect wave aspect ratio. All these peak strengths were predicted for the case of td/tc = 0.95 (defect is located at the bottom) and the wave height to thickness is 0.3.
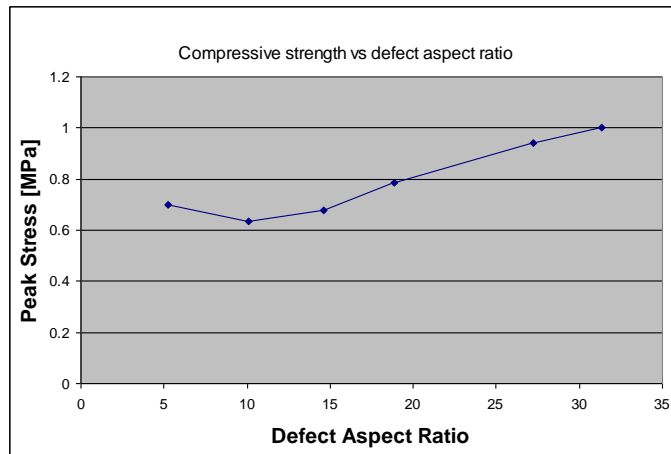
Figure 21   Compressive strength as a function of the defect aspect ratio (the defect location is at the bottom and the defect height to coupon ratio is 0.3)
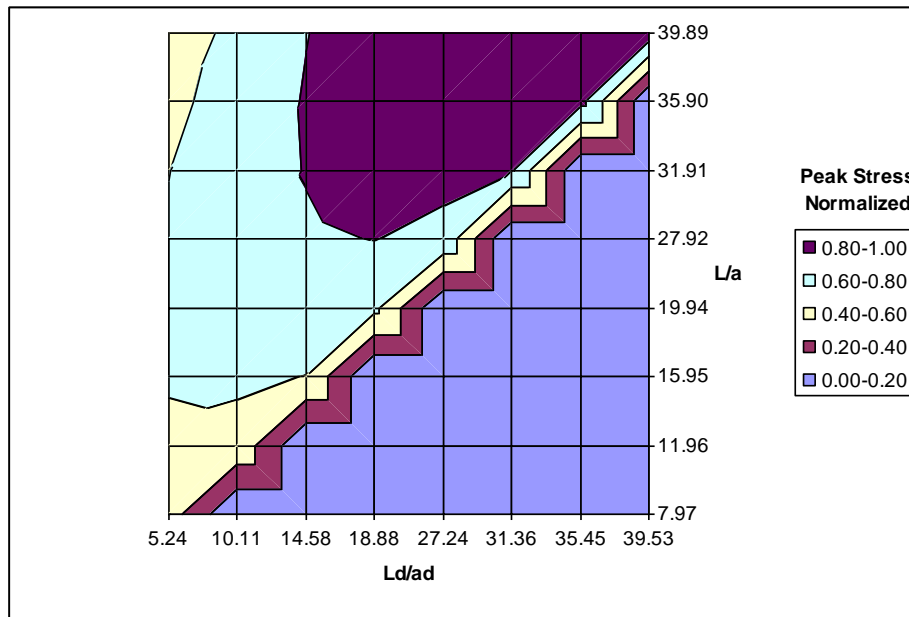
Figure 22   Surface plot showing the variation of defect compressive strength as a function of aspect ratio of internal defect and the external visible defect for defect height to thickness ratio of 0.3 and defect location ratio of 0.95

The coupons from carbon prepreg material were fabricated with a nominal thickness of 15 mm and wavy defects were introduced using procured resin inserts of specific thickness. Optical speckle based strain measurement technique was used to measure the specimen strain in realtime during testing. Figure 21 shows the typical optical strain patterns at the point of failure for the various coupons in the DOE space. The failure was a combination of kink band and splitting of layers. For some shallow defect coupons where the total coupon length was long, the

failure load was preceded by significant macro-scale bending of the coupon. So for these coupons the peak load recorded in the test could be significantly lower than the actual peak load for such shallow defects.
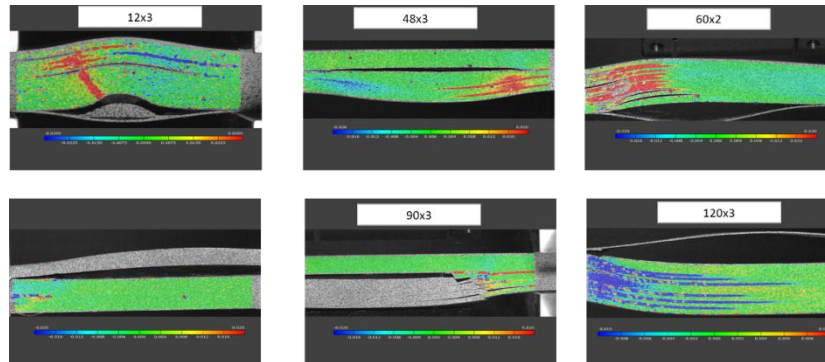

Figure 23   Typical force-displacement of coupon with corresponding optical strain images at pre-failure and failure and normalized failure stress as a function of wave aspect ratio

The micromechanics based numerical model can capture the localized micro-buckling leading to kinking type of failure. However, some of the failure modes seen in the coupons indicate a mix of splitting and globalized buckling leading to kink banding, which are not captured in the micromechanical modeling approach.

The carbon prepreg coupons were tested under pure compression. The coupons were measured for the defect size and locations. FE models were created of similar defects and run under simulated pure compressive loading. Figure 24 shows the model results of predicted failure points superposed over the test data points. The failure was a combination of kink band and splitting of layers.
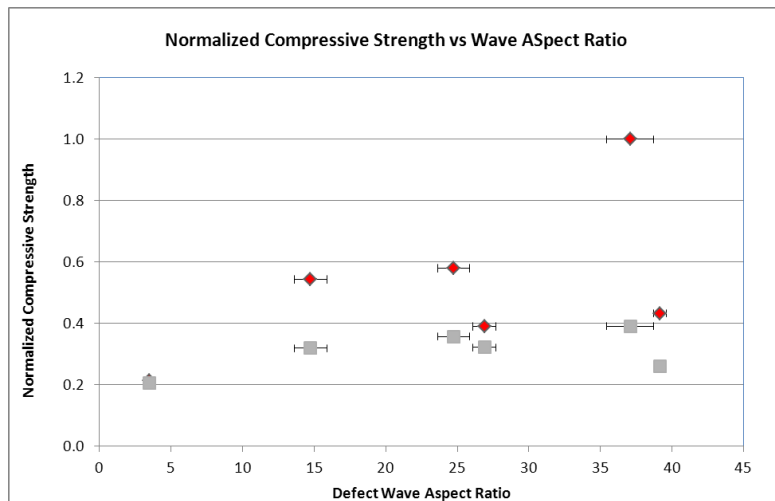

Figure 24   Comparison of defect physics model prediction (red boxes) with test coupon data (grey boxes)

Analysis of the results indicated that the model with the given inputs matches the trend of the test data in the lower end of defect aspect ratio (sharper waves). In the shallow waves for one of the cases the model over-predicts the test data point by a significant amount. One possible explanation is that the test coupon failure happened by splitting around defects and the current model does not have the capability to capture splitting type of failure. Also, another source of variability is the resin material input which is based on the resin properties of Aerotuf. The resin system used in the current coupons is supposed to be chemically similar to the Aerotuf but a different brand. We do not have mechanical test data of this newer resin system to input into the model. The micromechanics kinking model is able to capture the trends but has some significant difference in predicted load versus test data when the failure mode changes from kinking to splitting.

To understand the reasons for deviation between model predictions and test data, the model predictions were used to compare against another set of carbon wavy composite coupons with aspect ratios slightly more severe than the previous set of data. This validation is shown in Figure 25. The micromechanics based kinking model predictions compared well against the second set of data. The test data also indicated that the second set of data consistently failed in kinking mode of failure.
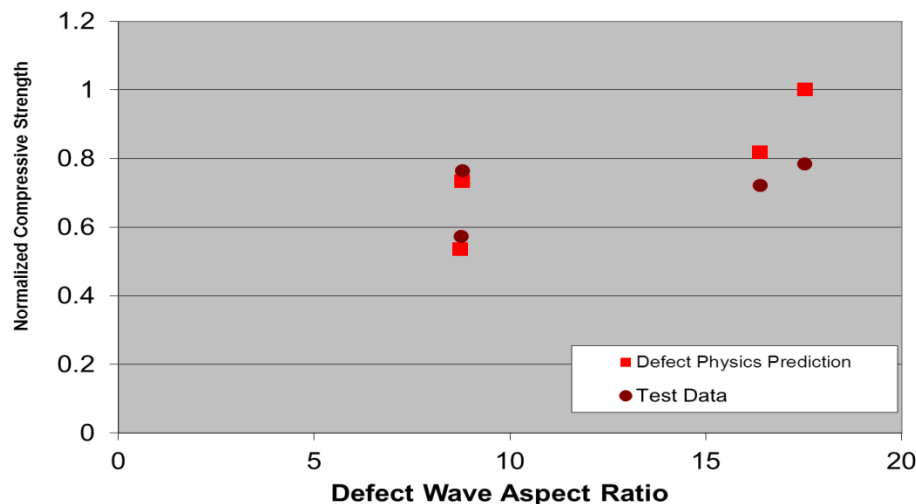
Figure 25   Micromechanics based kinking model predictions compared to experimental wavy carbon composites

The micromechanical model was also used to understand the impact of various defect geometric parameters on the predicted peak load response or the compressive strength. The model was used to determine the peak predicted compressive stress for various defect geometries ranging from very shallow wave aspect ratios to very sharp aspect ratio waves. Similarly the wave height to thickness ratio was also varied to study the impact of this defect geometry parameter on the predicted peak compressive stress. The results from the parametric study are shown in Figure 26.

Figure 26   Parametric study of various defect geometries using the micromechanical finite element based kink band prediction model

The results from the parametric study indicate that both the defect wave aspect ratio and the defect wave height ratio play significant role in the strength knockdown from the nominal compressive strength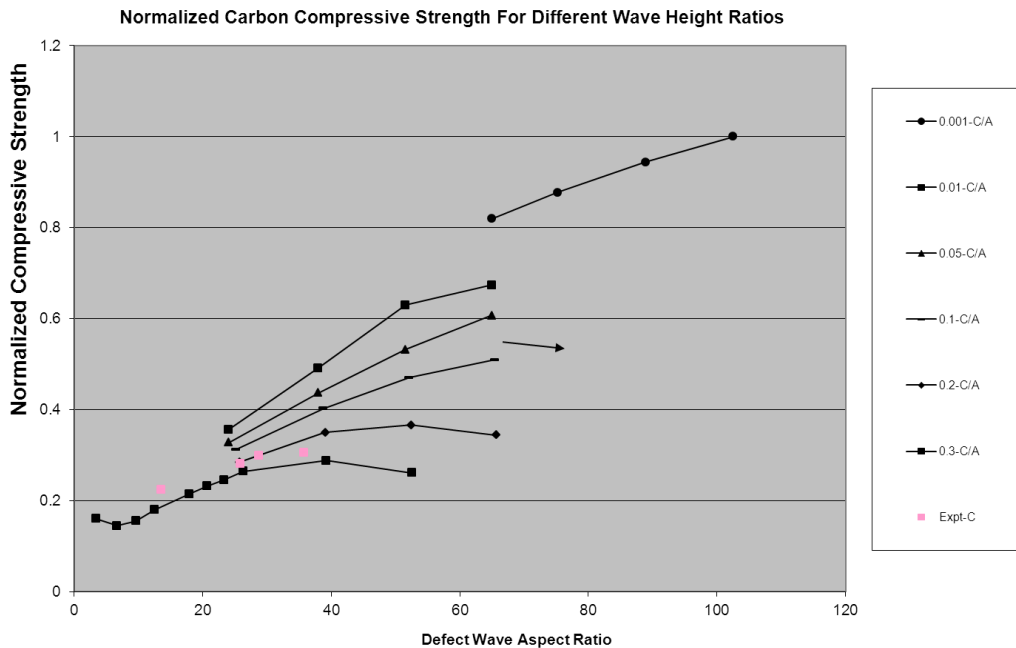 of defect free composite coupons. In fact a coupon with a very thick wave i.e., wave height ratio is very large, can never reach the original defect free coupon compressive strength even if the wave aspect ratio becomes very large (very shallow wave). This trend can be seen from the plot that at a given wave height ratio (ex. 0.3) the compressive strength tends to initially increase and then plateau with increasing aspect ratio. So to achieve higher compressive strengths, the wave height has to be small as well as the aspect ratio has to be shallow.

Conclusions

The current study as part of the inline inspection NDE program clearly indicated the significant impact of the defects like waviness on the compressive strength of unidirectional carbon composites. Mechanism based failure models like the nonlinear micromechanical finite element models seem to capture the dependency of the compressive strength on the defect geometry parameters. Further refinements to the model could be added to include other failure mechanisms observed in some of the test coupons. A single numerical model combining the cohesive failure model and the instability model could theoretically capture both the failure

modes and could significantly improve the versatility of the model in predicting the compressive failure strength under either of the failure mode.

Similarly in testing of the shallow defect coupons, the coupons tended to show a large amount of macroscopic global bending before failing. It is felt that this global bending mode is causing premature failure of the carbon coupons with shallow defects and thus indicating a lower strength than what it would normally fail at if the global bending mode was suppressed during the testing. Further improvements to the modeling strategy could also be made to include a global-local type of model to capture the localized instability mode with the local micromechanical model and a large scale global model to capture the global buckling mode as observed in the shallow defect coupons. This could lead to better match between the model predictions and the experimental data for these types of failure modes.

Recommended next steps
The current mechanics based modeling for impact of defects on compressive strength is applicable to post cured composites with known indications of defects. Another area of potential application of instability based modeling could be during the curing process. At that stage a combined approach including process modeling and a mechanics based failure model could indicate the dependency of process parameters and the likelihood of defect initiation during curing phase. This could be used to fine tune the process not only from the point of cure kinetics but also from a view to minimize the defect initiation and generation.

Task 3 Composites Process Modeling
The project goal as established by the GE Global Research Center (GE-GRC) is the establishment of process models for an automated tape layup system using composite material thermoset prepreg tapes. The process models are to be used to predict material defects from leading indicators during the on-line consolidation processing of thermoset prepregs. The system is designed to use carbon fiber and epoxy resin to produce wind turbine blade spar caps. Of particular interest is the understanding of how voids and other material defects form and propagate. The formation and transport of voids in composite materials remains a key research area in composite manufacturing science. Knowledge of how voids form and propagate throughout a composite material continuum during processing is key to minimizing failure due to the presence of void-initiated stress concentrations under load for a wide variety of composite applications (e.g. wind turbine blades). This research focuses on modeling void formation and transport in an on-line consolidation process of thermoset prepreg composite material tapes (e.g. carbon fiber + epoxy). The modeling is motivated to address optimization of the "green state" composite properties and processing parameters to reduce or eliminate "cured state" defects, such as porosity, de-lamination, and wrinkle-related defects. Figure 27 highlights the definitions of "green state" and "cured state" with respect to the system's processing steps.

Green State

| Tow Prepreg | Tape Prepreg | Tape Layup | Ply Buildup | Bagging | Vacuum |

Cured State

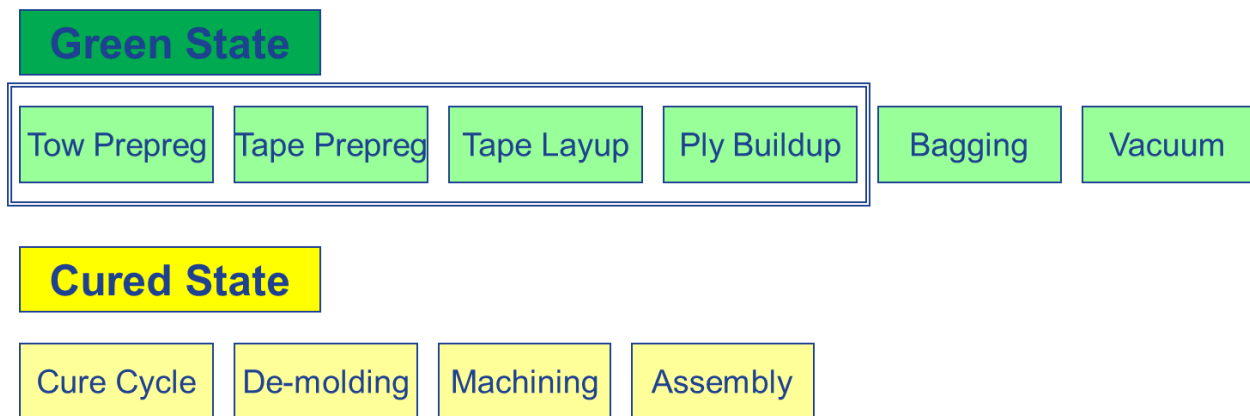| Cure Cycle | De-molding | Machining | Assembly |

Figure 27   Definitions of "Green State" and "Cured State" with respect to processing **steps**

The green state is defined as from the point where the resin and fiber are brought together to the point when the resin is cured to more than 5% degree of cure. The process modeling will be scoped during this regime, because it is here where defects can be detected and corrected, since fibers, resin, and defects have the ability to be moved before curing. The process models will be concentrated on in-line inspection values from tow pre-preg to ply-buildup such that inspection values can be fed into the process models to gauge understanding of the process in real time. The process models will also correlate measured inspection values to some of the defects after cure, such that one will have an understanding of the final cured state of the material and have the ability to trace processing modifications to changes in the final cured material. This work is supported by the Department of Energy under Award DE-EE0001367.

The process modeling tasks are to be performed by the University of Delaware (UD) – Center of Composite Materials (CCM). Figure 28 displays a program plan to be executed by UD-CCM. The figure highlights examples of in-line inspection parameters that the process modeling will examine and utilize to generate results that improve the understanding of the noted cured state defects (e.g. porosity, delamination, and wrinkling). The process modeling will be distributed into four distinct tasks. Figure 29 shows model schematics for each task. Task 1 will determine changes in tape width given an initial tape width to optimize the width in between tapes (or tape gap width) to mitigate composite wrinkling. The initial width, void, fiber, and resin content will be the input, while the model takes into consideration the roller pressure, tow speed, and resin viscosity. This work will be based on wet thermoplastic tape layup work done previously by Dr. Suresh G. Advani. Task 2 will determine parameters related to resin penetration into a fiber tow (e.g. permeability, time, radius, pressure) and determine what area of voids are tolerable with an applied vacuum. The resin impregnation at the tow level will be inspected and the model will determine how much of it is acceptable for full impregnation during the cure cycle. Task 3 will determine a one-dimensional model for flow in a delaminated area. The inter-ply is going to be inspected and the model will determine the critical gap length that can be filled with resin during the cure cycle and not result in a delamination. Task 4 will determine the critical wrinkle radius for successful vacuum compaction of a wrinkle. The initial wrinkle radius is going to be measured by inspection and the model will determine the critical radius that can be compacted during vacuum compaction. The following sections provide detailed formulation for each model

followed by a section on modeling synthesis that describes the full automated tape placement process model utilizing each task model.
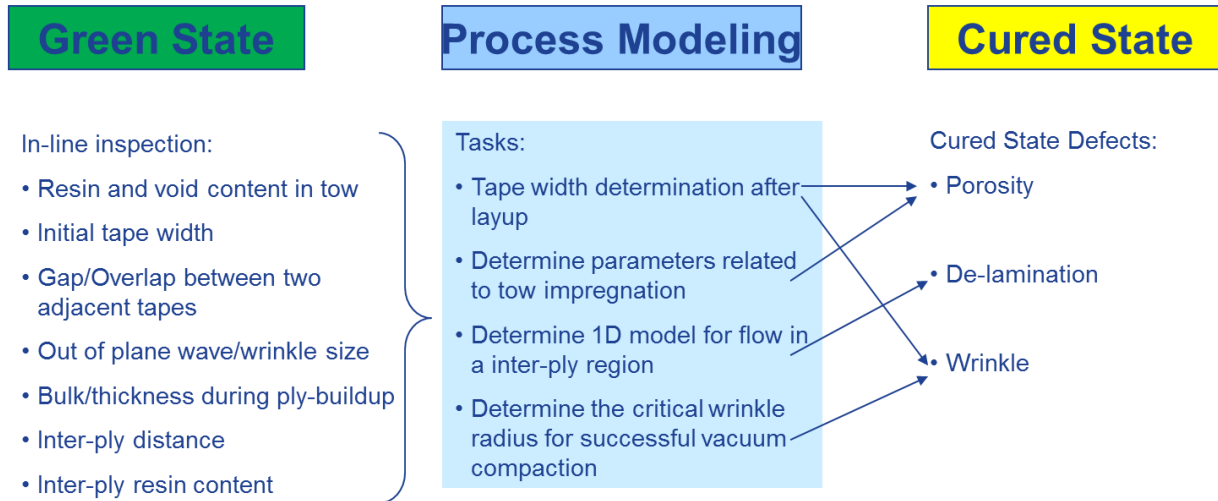

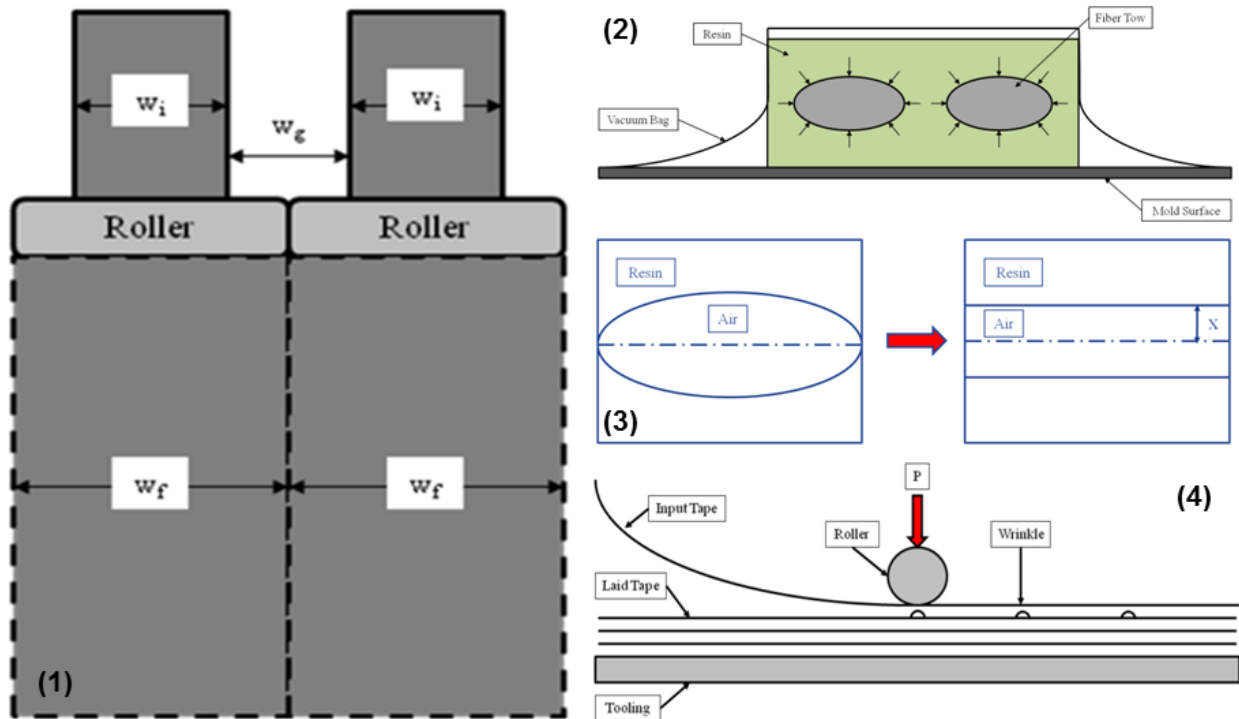Figure 28   GE-GRC and UD-CCM Program Plan

Figure 29   Process model schematics annotated with corresponding task number

Model 1: Tape Consolidation

The goal of Model 1 is to determine the change in tape width, while given the initial tape width to optimize the width in between tapes (or tape gap width) in order to mitigate composite wrinkling in an automated tape layup process. The materials being laid are a carbon fiber and epoxy prepreg system. Modeling is focused on the green state of the process, which includes the tow prepreg, tape prepreg, tape layup, and ply buildup steps before vacuum bagging and application. The process is being used to produce a wind turbine blade spar cap. The initial width, void content, fiber content, and resin content would be inputs to the model. The model would take into consideration the roller pressure, speed, and resin viscosity. This work is based on previous wet thermoplastic tape layup work by Dr. Suresh Advani [11].

The approach that will be used in modeling the tape process will be based on a squeeze-flow type model. The fiber + resin + void system will be considered as a single homogeneous viscous fluid continuum, due to the high viscosity of the carbon fiber – epoxy prepreg system under consideration. The rheological properties of the continuum are dependent on composite properties such as temperature, fiber volume fraction, and void content.
Figure **30** display various consolidation model process schematics labeled with input variables.
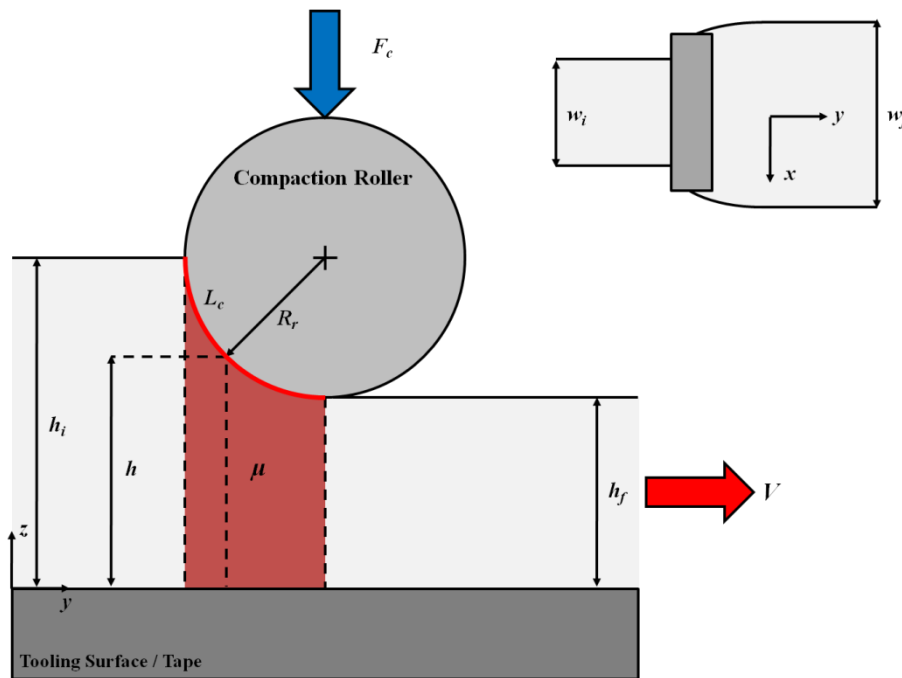
Figure 30   Consolidation process model schematics – input variables

As shown in Figure 30, the consolidation process model involves tows of given initial heights, h_i, and widths, w_i, that enter the regions under the compaction roller. The coordinate system is defined where x is in the width direction, y is in the direction of tow movement, and z is in the thickness direction. The tow speed, V, is given. As tows move under the compaction roller, the height and width change final values, h_i and w_i, respectively. Physically, the consolidation force compresses the voids and changes the heights and width of the tow. The tow dimension in the y

direction is observed to be much larger that the x and z directions; therefore, flow in the y direction may be neglected. Also, due to high matrix viscosity, the flow may be treated as a creeping motion and internal effects can be ignored.

To begin the analysis, the continuity and momentum equations that govern the fluid continuum of fiber + resin + voids are written for the motion under the compaction roller, while neglecting inertia and body force terms.

$$\frac{\partial \rho}{\partial t} + \frac{\partial}{\partial x}(\rho v_x) + \frac{\partial}{\partial z}(\rho v_z) = 0 \tag{1.1}$$

$$\frac{\partial P}{\partial x} = \frac{\partial}{\partial x}\left(\mu\left[2\frac{\partial v_x}{\partial x}\right]\right) + \frac{\partial}{\partial z}\left(\mu\left[2\frac{\partial v_x}{\partial z} + \frac{\partial v_z}{\partial x}\right]\right) \tag{1.2}$$

$$\frac{\partial P}{\partial z} = \frac{\partial}{\partial x}\left(\mu\left[\frac{\partial v_x}{\partial z} + \frac{\partial v_z}{\partial x}\right]\right) + \frac{\partial}{\partial z}\left(\mu\left[2\frac{\partial v_z}{\partial z}\right]\right) \tag{1.3}$$

Note the following fluid continuum parameters present in the equations: density ρ, viscosity μ, pressure P, and velocity v. Typically actual tows have a much smaller thickness (e.g. 0.006") than width (e.g. 0.25"). This allows one to assume that the dominant velocity gradient term within the momentum equations is shear strain through the thickness, $\partial v_x / \partial z$ and its derivative with respect to z. The momentum equations (1.2) and (1.3) can be simplified to the following results.

$$\frac{\partial P}{\partial x} = \frac{\partial}{\partial z}\left(\mu\frac{\partial v_x}{\partial z}\right) \tag{1.4a}$$

$$\frac{\partial P}{\partial z} = 0 \tag{1.4b}$$

Integration of equation (1.4b) shows that $P = P(x)$. The continuity equation (1.1) can be simplified by assuming a Newtonian constitutive law. It is also assumed that the continuum density is affected only by local pressure. Depending on how the continuity equation is simplified will determine the complexity of the modeling. The isothermal incompressible case will be considered first to simplify the analysis for later more complicated cases.

The analysis will proceed by solving for the velocity in the x direction as a function of z. To begin, the continuity equation (1.1) will be simplified assuming a constant density for the incompressible case.

$$\frac{\partial \rho}{\partial t} + \frac{\partial}{\partial x}(\rho v_x) + \frac{\partial}{\partial z}(\rho v_z) = 0$$

$$\boxed{\frac{\partial}{\partial x}(v_x) + \frac{\partial}{\partial z}(v_z) = 0}$$

This equation can be integrated with respect to z first to solve the equation:

$$\int_0^h \left[\frac{\partial}{\partial x}(v_x)\right] dz + \int_0^h \left[\frac{\partial}{\partial z}(v_z)\right] dz = 0$$

$$\boxed{\int_0^h \left[\frac{\partial}{\partial x}(v_x)\right] dz + v_z|_{z=0}^{z=h} = 0} \tag{1.5}$$

Note: $v_z|_{z=0} = 0$, $v_z|_{z=h} = \dot{h}$

Equation (1.5) can be simplified by the following change in order of derivative and integration:

$$\int_0^h \left[\frac{\partial}{\partial x}(v_x)\right] dz + v_z|_{z=0}^{z=h} = 0$$

$$\boxed{\frac{\partial}{\partial x}\left(\int_0^h v_x\, dz\right) + \dot{h} = 0} \tag{1.6}$$

Next, return to equation (1.4a) and simply to get an expression for v_x (note dummy variable of integration, ξ):

$$\frac{\partial P}{\partial x} = \frac{\partial}{\partial z}\left(\mu\frac{\partial v_x}{\partial z}\right)$$

$$\xrightarrow{\int dz} \mu\left[\frac{\partial v_x}{\partial z}\right] = z\frac{\partial P}{\partial x} + C_1(x)$$

$$\xrightarrow{\int dz} v_x(z) = v_x(0) + \frac{\partial P}{\partial x}\int_0^z \frac{\xi}{\mu}\,d\xi + C_1(x)\int_0^z \frac{1}{\mu}\,d\xi$$

$$\boxed{v_x(z) = v_x(0) + \frac{\partial P}{\partial x}\left(\frac{z^2}{2\mu}\right) + C_1(x)\left(\frac{z}{\mu}\right)} \tag{1.7}$$

To solve for the integration constants in equation (1.7), an assumption of no slip boundary conditions will be made at the tooling surface (metallic or previously laid tape). Figure 31 displays a schematic with these boundary conditions shown with respect to the model.
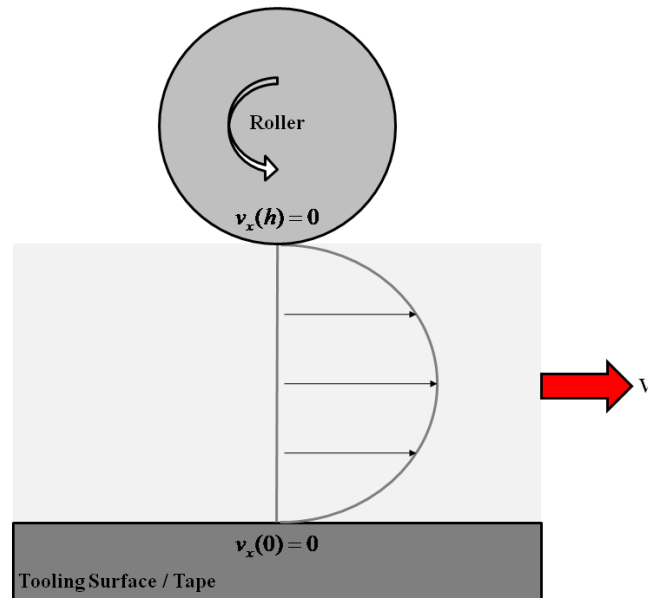
Figure 31   No-slip velocity boundary conditions schematic

Applying the boundary conditions to equation (1.7):

$v_x(0) = 0$:

$$0 = v_x(0) + 0 + 0$$

$$\boxed{v_x(0) = 0}$$

$v_x(h) = 0$:

$$0 = \frac{\partial P}{\partial x}\left(\frac{h^2}{2\mu}\right) + C_1(x)\left(\frac{h}{\mu}\right)$$

$$\boxed{C_1(x) = -\frac{\partial P}{\partial x}\left(\frac{h}{2}\right)}$$

With these relations, equation (1.7) can be simplified through the following steps to get an expression for the fiber-resin continuum velocity:

$$v_x(z) = \frac{\partial P}{\partial x}\left(\frac{z^2}{2\mu}\right) - \frac{\partial P}{\partial x}\left(\frac{h}{2}\right)\left(\frac{z}{\mu}\right)$$

$$v_x(z) = \frac{\partial P}{\partial x}\left[\left(\frac{z^2}{2\mu}\right) - \frac{zh}{2\mu}\right]$$

$$v_x(z) = \frac{\partial P}{\partial x}\left[\frac{1}{2\mu}(z^2 - zh)\right] \tag{1.8}$$

An expression for the pressure of the fiber-resin continuum can be found using equation (1.8) to eliminate the velocity term in equation (1.6). This will allow the equation to be integrated in terms of pressure only and not velocity.

$$\frac{\partial}{\partial x}\left(\int_0^h v_x\, dz\right) + \dot{h} = 0$$

$$\frac{\partial}{\partial x}\left(\int_0^h \left(\frac{\partial P}{\partial x}\left[\frac{1}{2\mu}(z^2 - zh)\right]\right) dz\right) = -\dot{h}$$

$$\frac{\partial}{\partial x}\left(\frac{\partial P}{\partial x}\frac{1}{2\mu}\int_0^h (z^2 - zh)\, dz\right) = -\dot{h}$$

$$\frac{\partial}{\partial x}\left(\frac{\partial P}{\partial x}\frac{1}{2\mu}\left(\frac{-h^3}{6}\right)\right) = -\dot{h}$$

$$\frac{\partial^2 P}{\partial x^2} = \frac{12\dot{h}\mu}{h^3} \tag{1.9}$$

Equation (1.9) can be integrated to yield an expression for pressure as a function of tape width (x direction).

$$\frac{\partial^2 P}{\partial x^2} = \frac{12\dot{h}\mu}{h^3}$$

$$\xrightarrow{\int dx} \frac{\partial P}{\partial x} = \frac{12\dot{h}\mu}{h^3}x + C_2$$

$$\xrightarrow{\int dx} P(x) = \frac{6\dot{h}\mu}{h^3}x^2 + C_2 x + C_3$$

The following pressure boundary conditions will be applied to solve for the integration constants in the following equation. These conditions are based on the fact that the fiber-resin continuum pressure is equal to the atmospheric pressure at the outside edges of the tape, and the fact that flow is not expected to take place outside constrained edges of tows (i.e. pressure gradient is zero).

$$\frac{\partial P(0)}{\partial x} = 0:$$

$$0 = 0 + C_2 \rightarrow \boxed{C_2 = 0}$$

$P(w) = 0:$

$$0 = \frac{6\dot{h}\mu}{h^3}w^2 + C_3 \rightarrow \boxed{C_3 = \frac{-6\dot{h}\mu w^2}{h^3}}$$

With the pressure boundary conditions applied, an expression for fiber-resin continuum pressure can be written.

$$\boxed{P(x) = \frac{6\dot{h}\mu}{h^3}(x^2 - w^2)} \tag{1.10}$$

In addition, one can take the derivative with respect to x of equation (1.10) and substitute it into equation (1.8) to eliminate the pressure gradient term in the velocity expression to yield the following result.

$$\boxed{v_x(x,z) = \frac{12x\dot{h}\mu}{h^3}\left[\frac{1}{2\mu}(z^2 - zh)\right]} \tag{1.11}$$

To calculate the compaction force from the roller, one can integrate the pressure expression across the width and along the contact length. This operation will make optimization of the process model easier, since compaction force is typically easier to measure versus fluid pressure.

$$F_c = 2\int_0^{L_c}\int_0^w P(x,y)dxdy$$

$$F_c = 2\int_0^{L_c}\int_0^w \frac{6\dot{h}\mu}{h^3}(x^2 - w^2)dxdy \tag{1.12}$$

Note the following geometric parameters from the roller and tape geometry:

Initial tape height $= h_i$

Final tape height $= h_f$

Roller radius $= R_r$

Contact length:

$$L_c = \left[R_r^2 - (R_r - h_i + h_f)^2\right]^{\frac{1}{2}}$$

Instantaneous height:

$$h = R_r + h_f - [R_r^2 - (L_c - y)^2]^{\frac{1}{2}}$$

Closing speed:

$$\dot{h} = \frac{dh}{dt} = -V \frac{\left[R_r^2 - (R_r - h + h_f)^2\right]^{\frac{1}{2}}}{(R_r - h + h_f)}$$

In addition, the incompressible fluid assumption ensures a conservation of mass and volume. It can be shown that:

$$wh = \text{constant} = C = w_i h_i = w_f h_f \qquad (1.13)$$

Or,

$$w = \frac{w_i h_i}{h} = \frac{w_f h_f}{h}$$

Equation (1.12) can be integrated with respect to x:

$$F_c = 2 \int_0^{L_c} \int_0^w \frac{6\dot{h}\mu}{h^3}(x^2 - w^2)dxdy; \ w = \frac{w_i h_i}{h}$$

$$F_c = 2 \int_0^{L_c} \frac{6\dot{h}\mu}{h^3}\left(\frac{-2h_i^3 w_i^3}{3h^3}\right)dy$$

$$F_c = -8\mu h_i^3 w_i^3 \int_0^{L_c} \frac{\dot{h}}{h^6}dy \qquad (1.14)$$

To evaluate the integral in equation (1.14) with respect to y, note the following chain rule relationship for $\dot{h}$:

$$\dot{h} = \frac{dh}{dt} = \frac{dh}{dy}\frac{dy}{dt} = V\frac{dh}{dy}$$

Substitution into equation (1.14) can lead to an expression of the compaction force and the effective viscosity of the fiber-resin continuum.

$$F_c = -8\mu h_i^3 w_i^3 \int_0^{L_c} \frac{\dot{h}}{h^6}dy$$

$$F_c = -8\mu h_i^3 w_i^3 \int_{h=y(0)}^{h=y(L_c)} \frac{V\dfrac{dh}{dy}}{h^6}dy$$

$$F_c = -8\mu h_i^3 w_i^3 \int_{h_i}^{h_f} \frac{V}{h^6}\, dh$$

$$F_c = -8\mu h_i^3 w_i^3 V \left[\frac{1}{5h_i^5} - \frac{1}{5h_f^5}\right]$$

$$\boxed{F_c = -\frac{8\mu w_i^3 V}{5}\left(\frac{h_f^5 - h_i^5}{h_i^2 h_f^5}\right)} \tag{1.15}$$

Or,

$$\boxed{\mu = -\frac{5}{8}\frac{F_c}{w_i^3 V}\left(\frac{h_i^2 h_f^5}{h_f^5 - h_i^5}\right)} \tag{1.16}$$

Equation (1.16) can be used to find the effective fiber-resin continuum viscosity that can be applied to various compaction forces and tow speeds. Equation (1.15) can be rewritten to express the compaction ratio, h_f/h_i, as a function of material parameters (e.g. compaction forces, tow speeds, material viscosity) using a nondimensional parameter, Π_{ii}:

$$\Pi_{ii} \equiv \frac{5}{8}\frac{F_{eff}\, h_i^2}{\mu V w_i^3} \tag{1.17}$$

Thus,

$$1 - \left(\frac{h_i}{h_f}\right)^5 = -\Pi_{ii}$$

$$\boxed{\frac{h_f}{h_i} = (1 + \Pi_{ii})^{-\frac{1}{5}}} \tag{1.18}$$

The dimensionless parameter, Π_{ii}, can vary from 0 to ∞ depending on the parameters of the problem. It provides a basis for comparing multiple process parameters to the chosen compaction ratio. Figure 32, Figure 33, and Figure 34 display various plots that show how the compaction ratio varies with changes in tow speed, effective viscosity, and compaction force using equation (1.18). It can be seen from Figure 32 that there is a large growth and settling out asymptotically of the compaction ratio as tow speed is increased. From a design perspective, one can choose a tow speed from the settled out region for maximum compaction ratio. A similar curve is seen in Figure 33 for effective viscosity. Essentially, higher viscosity regions lead the compaction ratio to settle out towards some nominal asymptotic value. The compaction force appears to have an inverse effect on the compaction ratio compared to tow speed and effective viscosity. From a design perspective, it appears that increasing the compaction force can greatly decrease the compaction ratio and that minimal compaction force is key to high compaction ratio; however, some compaction force is necessary to consolidate fibers physically. By tweaking the parameters of tow speed, effective viscosity, and compaction force, one can

arrive to an optimized compaction ratio for a tape consolation process. Finally, once the compaction ratio is determined, the final tape width can be found using equation (1.13), based on conservation of mass and volume.

$$w_f = w_i \left(\frac{h_f}{h_i}\right)^{-1} = w_i (1 + \Pi_{ii})^{\frac{1}{5}}$$
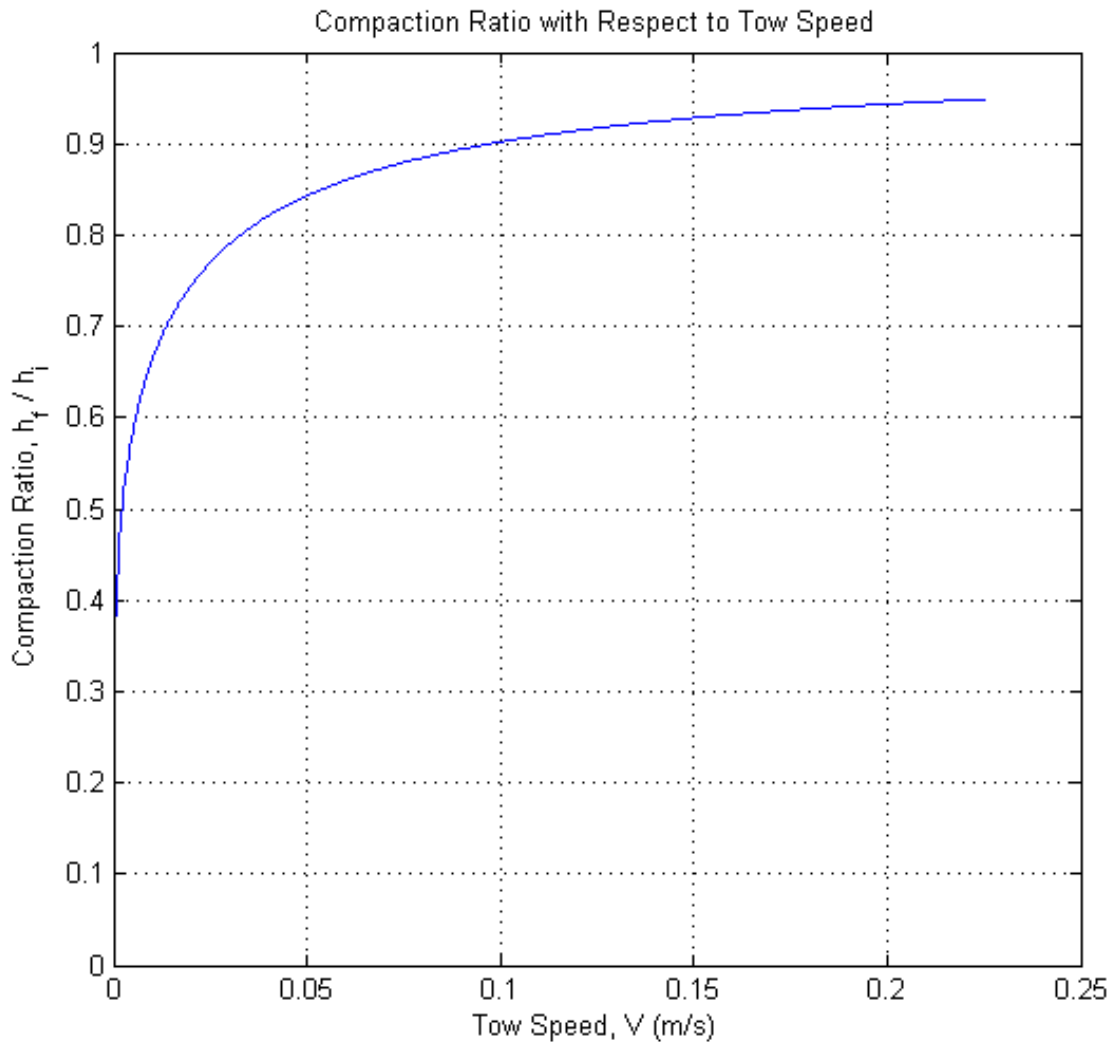
(1.19)

Figure 32　　Compaction Ratio with respect to Tow Speed
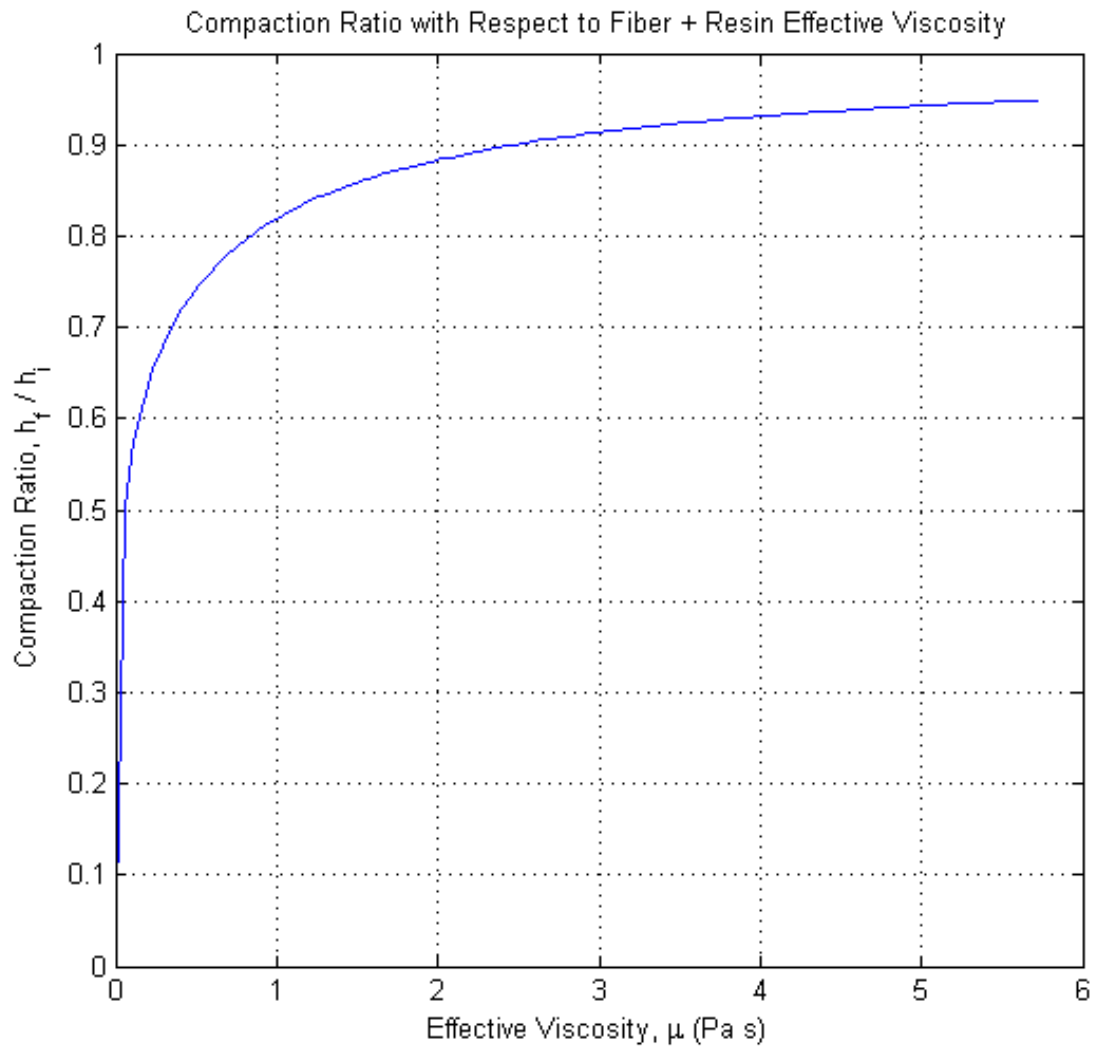
Figure 33   Compaction Ratio with respect to Effective Viscosity
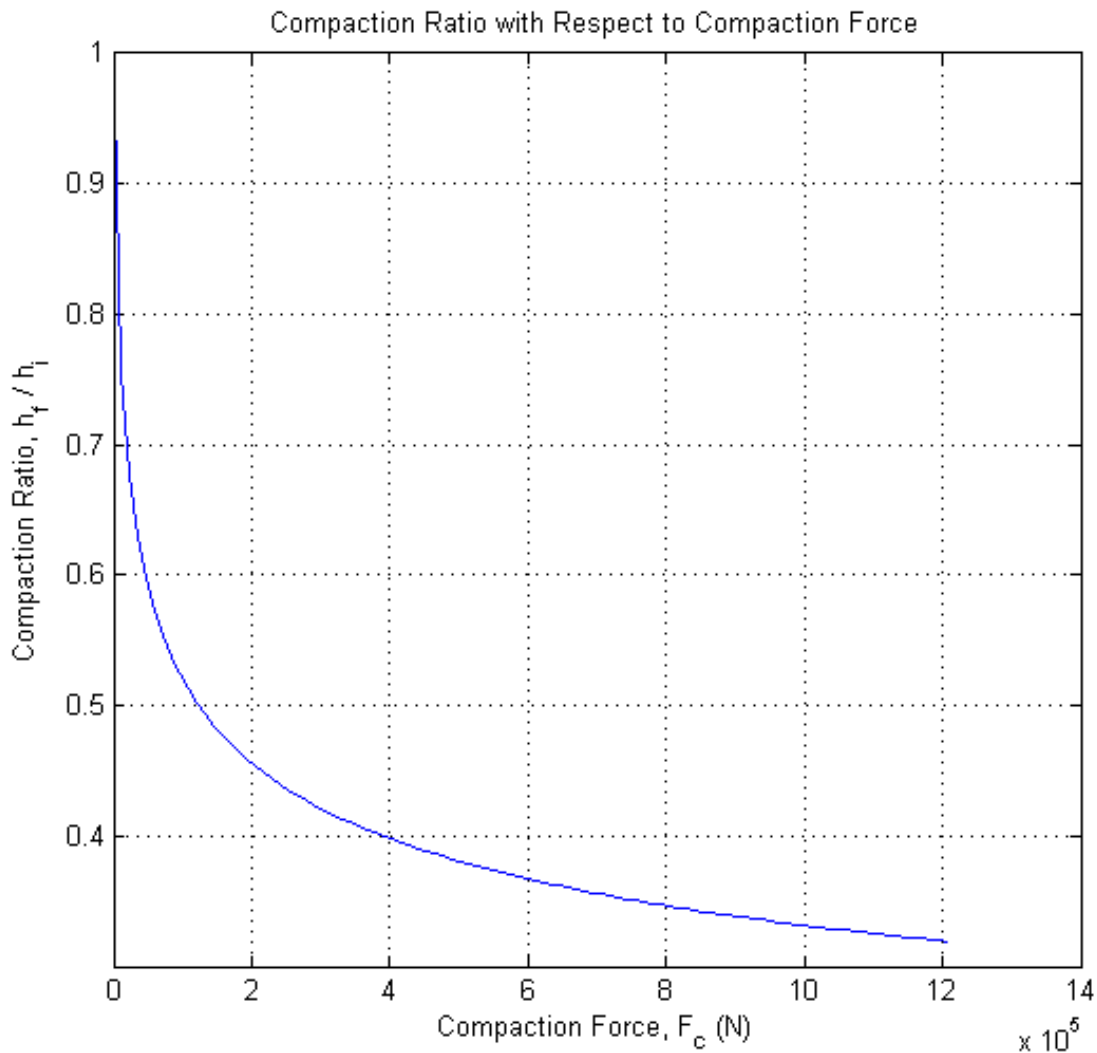
Figure 34   Contact Ratio with respect to Compaction Force

A modification to the isothermal incompressible tape width model has been made to accommodate for the non-uniform pressure distribution under the compaction roller. Intuitively, the pressure distribution in the fiber/resin fluid continuum would be maximum directly underneath the centerline of the roller axis, for which maximum force in the z-direction is applied; however, the z-component of the applied compaction force decreases as one travels away from the centerline of the roller axis along the contact length. To accommodate for this decrease in the z-direction compaction force component, one can introduce a parametric angle, θ, and integrate all the z-direction compaction force components applied to the fluid along the contact length. Figure 35 displays a schematic of the roller compaction force modification.

Figure 35   Roller compaction force modification

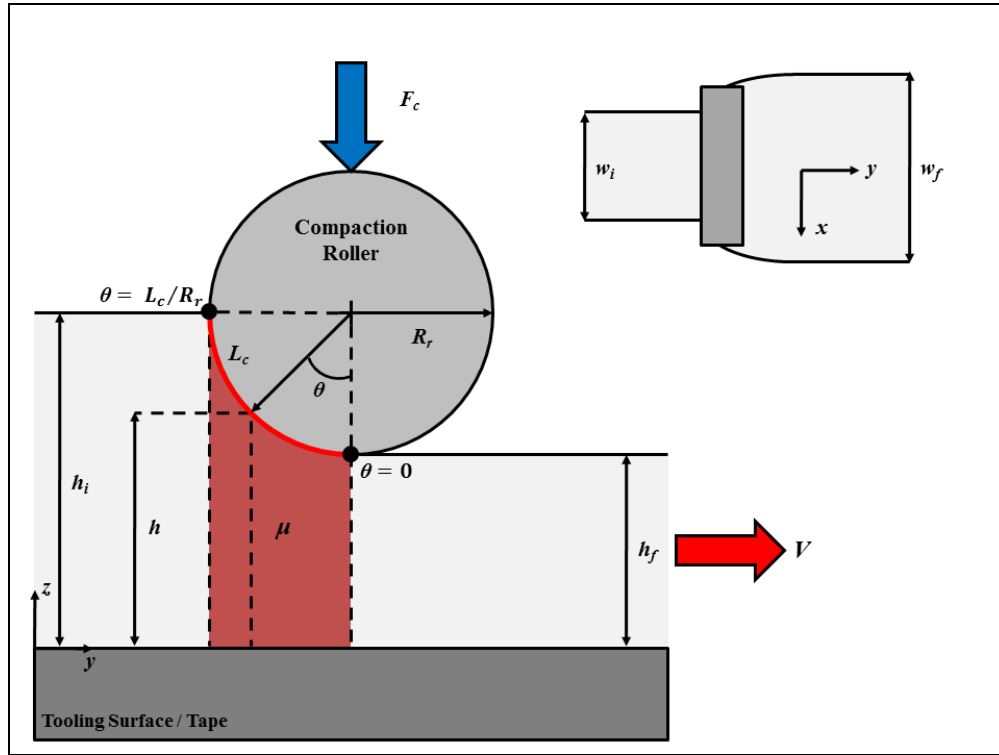Since the roller is of a circular geometry, one can parameterize the endpoints of the contact length by noting that the contact length forms a circular arc and using the simple circular arc length formula to find the maximum parametric angle to integrate to:

$$L_c = R_r \theta \tag{1.20}$$

$$\theta = L_c / R_r \tag{1.21}$$

With this known maximum contact angle, one can use it to integrate all of the z-component compaction forces along the contact length to obtain an effective contact force, F_{eff}:

$$F_{eff} = \int_0^{L_c/R_r} F_c \cos\theta \, d\theta$$

$$F_{eff} = F_c \sin(L_c / R_r) \tag{1.22}$$

This formula provides a modification (F_{eff}) that can be substituted directly in the isothermal incompressible analysis for F_c in order to account for the changing pressure distribution throughout the contact length underneath the roller. The following data included in Table **4** demonstrate how the modification changes the contact force values for input into the isothermal incompressible model. Note F_c is calculated using the formula from the previous isothermal incompressible tape width analysis:

Table 4   Compaction force modification sample values

h_i	0.0010 m
h_f	0.00079 m
R_r	0.05 m
w_i	0.1052 m
P	300 N/in
V	0.2250 m/s
L_c	0.0051 m (calculated)
F_c	1242.4 N (calculated)
F_{eff}	126.3171 N (calculated)

When F_{eff} is substituted into the isothermal incompressible model for F_c, the calculated effective viscosity of the fluid, μ, is modified as well since the compaction force is used in its calculation. Use of the compaction force modification does not change the generated processing dimensionless parameter, Π_{ii}, significantly. This is due to the fact that in the calculation of Π_{ii}, changes made by F_{eff} are balanced by subsequent changes in μ, which leads to similar values compared to the case of calculating Π_{ii} with the unmodified F_c value. The modification does provide a better understanding of the physics of the non-uniform pressure distribution of the fluid continuum underneath the roller throughout the entire contact length.

To account for the presence of voids in the prepreg tape system, the isothermal incompressible tape width model can be modified based on conservation of mass relationships. Figure 36 displays a schematic of the void physics conservation of mass system.
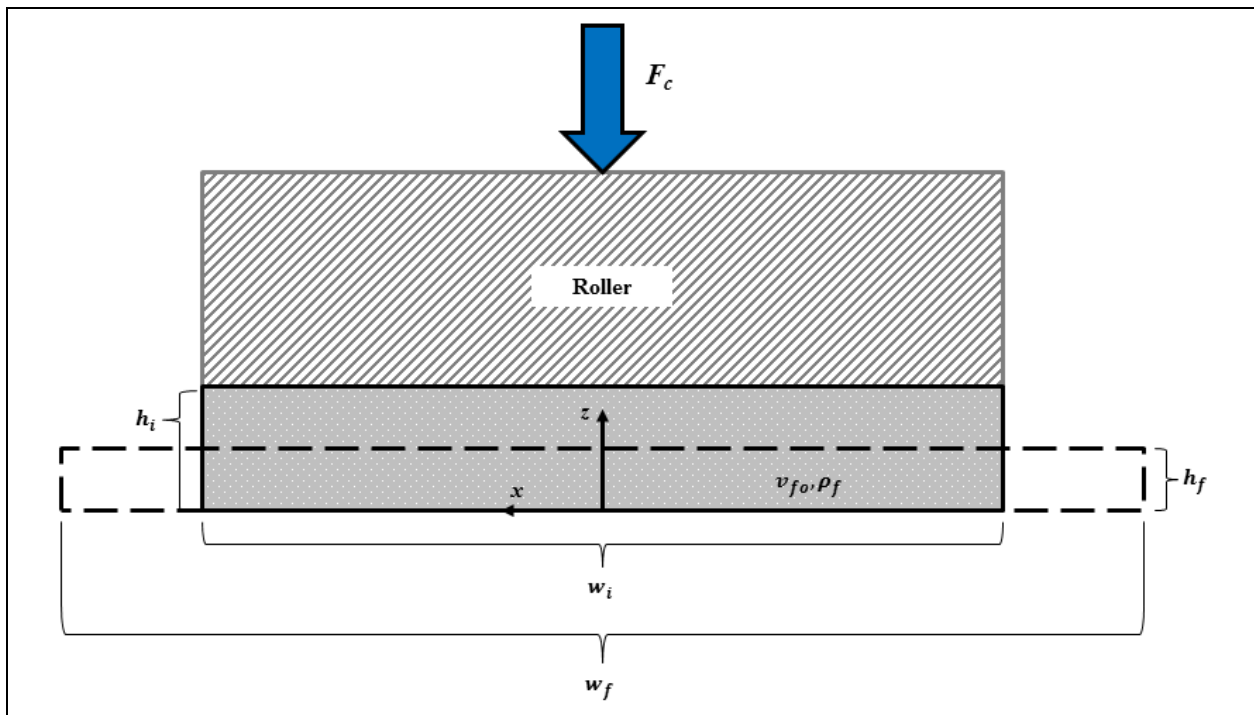

Figure 36   Void physics mass conservation schematic

In the figure, a cross-section of the x-z plane is observed directly underneath the centerline of the roller. As the system experiences compaction force, the cross-sectional shape changes from a rectangle with an initial height and width (h_i, w_i) to a rectangle with a different final height and width (h_f, w_f). To account for the presence of voids, one can assume that the spherically-modeled voids absorb resin while under pressure, get compressed, or are pushed out of the tape. Void compression is the most likely phenomenon. The volume compressed is occupied by the resin. The following illustrates the result of performing a mass balance on the cross-section within the tape before and after compaction force application:

$$m_{in} = m_{out} + m_{abs}$$

$$\rho_f Vol_{in} = \rho_f Vol_{out} + \rho_f Vol_{voids} \tag{1.23}$$

Assume a volume of fluid with a unit thickness, t, and represent the void fraction of the tape with v_{fo}, and the density of the fiber + resin fluid continuum as ρ_f:

$$\rho_f(w_i * h_i * t) = \rho_f(w_f * h_f * t) + \rho_f[(w_f * h_f * t) * v_{fo}]$$

$$w_i h_i = w_f h_f + w_f h_f v_{fo}$$

$$w_i h_i = w_f h_f(1 + v_{fo}) \tag{1.24}$$

Here v_{fo} is the volume fraction of the compressed voids. So if the initial void fraction is v_{fi} and if the final compressed volume is v_{ff}, then $v_{fo} = v_{fi} - v_{ff}$. This relationship yields the same result as with the isothermal incompressible case with the addition of the $(1 + v_{fo})$ term to account for the presence of voids within the tape. For example, if one assumes a reasonable value for the void fraction or experimentally determines the void fraction, one can use the model to solve for the final tape with, given the initial width and the compaction ratio predicted by the isothermal incompressible case analysis with the following formula:

$$w_f = w_i \left[\left(\frac{h_f}{h_i} \right)(1 + v_{fo}) \right]^{-1} \tag{1.25}$$

Table 5 provides some example experimental data along with % error to showcase the validity of the model:

Table 5   Analytical and experimental comparison of final width calculation

h_i	1.05 mm
h_f	0.79 mm
w_i	105.19 mm
v_{fo}	0.30
w_f (calculated)	107.55 mm
w_f (experimental)	109.17 mm
% error	1.49 %

Overall, the inclusion of the void fraction term can provide more realistic estimates of the final tape width when added to the isothermal incompressible model.

A process model has been presented that predicts consolidation and final tape dimensions during the on-line consolidation of thermoset prepregs. The model considers geometric, material, and process parameters with the goal of exploring the influence of process parameters. Results show how the compaction ration varies with changes in effective viscosity of prepreg, tow speed, and applied compaction force. Voids are found to be inversely proportional to the compaction ratio. Once can extend this model to introduce pre-existing voids in the prepreg by treating the materials as a compressible medium.

Model 2: Tape Impregnation

Knowledge of how voids form and propagate during processing is important for minimizing structural failures in composite materials. Voids initiate stress concentrations when subjected to loads. The overall goal of this research is to develop process models to predict defects (e.g. voids) from leading indicators during on-line consolidation processing of partially impregnated thermoset prepregs. These thermoset prepreg consists of continuous glass or carbon fibers that are partially covered with resins such as epoxies. They have pockets of dry fibers within the prepreg without the resin. The goal during the processing of such materials is to get the resin to cover all the fibers without any dry regions or voids. This is usually done in two steps. The 'green state' of the prepreg refers to when the tape is placed on the tool at room temperature introducing partial consolidation of the various layers. Step two is when the entire assembly is placed in an autoclave or an oven and subjected to heat and pressure to completely consolidate and cure the composite. Figure 37 introduces a schematic of the step one of the on-line consolidation process that is the focus of this paper.
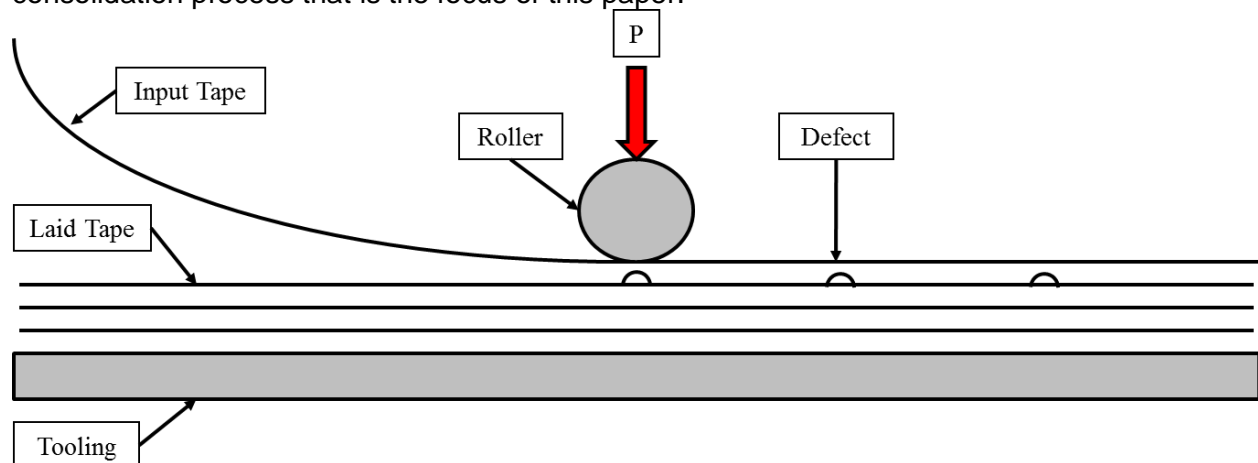
Figure 37   An on-line composite prepreg tape consolidation process schematic

When a tape is placed over a substrate or on a previously placed tape layer as shown in Figure 37 using a consolidation roller, the resin within the partially impregnated prepreg will redistribute under the roller pressure reducing the regions of fibers uncovered by resin (voids). In this work we will model the resin impregnation as a function of roller pressure, speed and resin viscosity during the green state of the process. Two main phenomena of (i) resin impregnation in fiber tows and (ii) consolidation of fiber tows will be considered. The model will seek to determine the degree of resin impregnation of the tape due to the roller compaction. Presented results are

based on sample values representative of typical carbon/epoxy prepreg tape system. This work is based on previous wet thermoplastic tape layup research as described in [11] and expansion of compression resin transfer molding (CRTM) work found in [12].

It is of significant research interest to study the microscale resin impregnation that occurs when composite prepreg tapes are under compaction during processing. In this work, the goal is to determine parameters related to resin penetration into the partially impregnated fiber tow and quantify the remaining unfilled region of fiber tows as a function of resin viscosity, roller pressure and roller speed. This type of analysis is of practical research interest, because partially impregnated composite prepregs are a significant portion of available prepregs on the market and are frequently used for composite applications for their contained optimized net resin content. Figure 38 displays a sample of a partially impregnated unidirectional composite prepreg tape. Of particular interest is the distinction between the resin rich top and bottom surfaces (e.g. "shiny" surfaces of the tape within the figure) versus the fibrous dry center of the tape that must be impregnated during processing and cure.
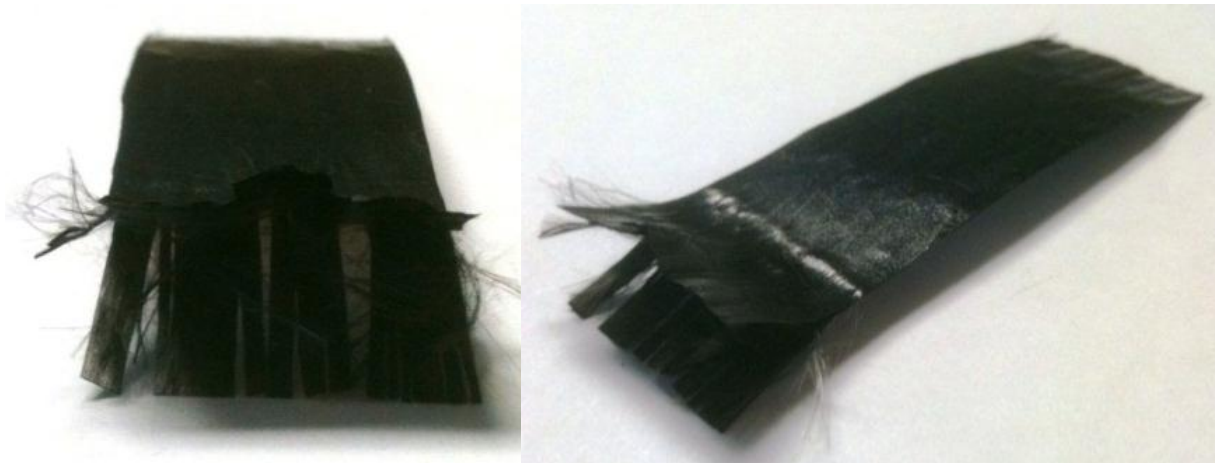

Figure 38   Partially impregnated composite prepreg tape sample with resin rich top and bottom surfaces (e.g. "shiny" surfaces of the tape within the figure) versus the fibrous dry center

Parameters that would be relevant for this process are tape thickness, tape displacement, average fiber volume fraction, average through thickness permeability, and compaction time. The model has been simplified and considers a single tow unit cell cross-section of tape that is directly located underneath the roller, with a unit cell consisting of a single dry tow surrounded by a resin shell. Figure 39 displays a schematic of the roller-tape system under consideration here, with a tow unit cell shown. The unit cell approach permits for an adaptable solution for a variety of tape architectures (e.g. woven materials) and boundary conditions (e.g. tape-tape, tape tooling); however, the scope of this work will be limited to the unidirectional tape system.
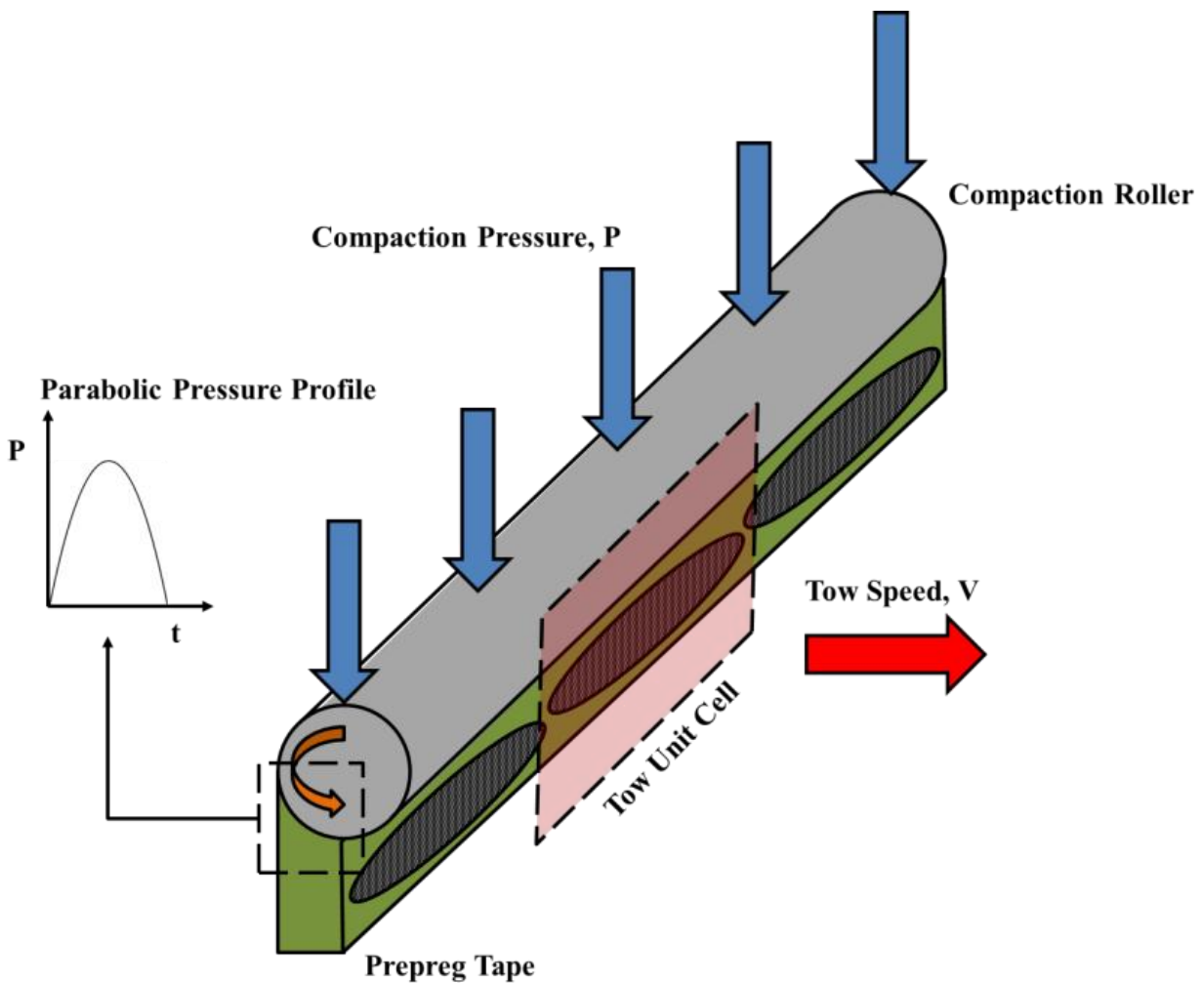
Figure 39   Schematic of a simplified roller – tape model with a tow unit cell

As shown in Figure 39, the model assumes an ellipsoidal fiber tow unit cell impregnation can be approximated as a 1D rectangular fiber unit cell impregnation. A symmetric solution approach is taken to mitigate the ellipsoidal tow cross section assumption, such that data is calculated with respect to the top or bottom of the tape cross section to the centerline of the tape cross section. In addition, the model accounts for the pressure distribution from the roller by the application of a parabolic pressure profile as a function of time. This model is based on process modeling research conducted within compression resin transfer molding (CRTM) as described in [12]. Figure 40 displays a modeling schematic for the tape impregnation process model based on the single unit cell. The CRTM process model in [12] is based on three processing phases that can be adapted for the composite tape placement processes: Phase 1: A given amount of resin injected into a partially closed mold containing a dry fiber preform which in our process is the resin that is layered on top of the dry tape (fibers) prior to rolling; Phase 2: The closure of the mold until it is in contact with the fiber preform displacing all the resin into the preform, which in our process is the initial roller compaction; Phase 3: Further mold closure to the desired thickness of the part compacting the fiber preform and redistributing the resin, which in our process is the final roller compaction. These processing phases are established within the context of the tape placement processing described in this work.
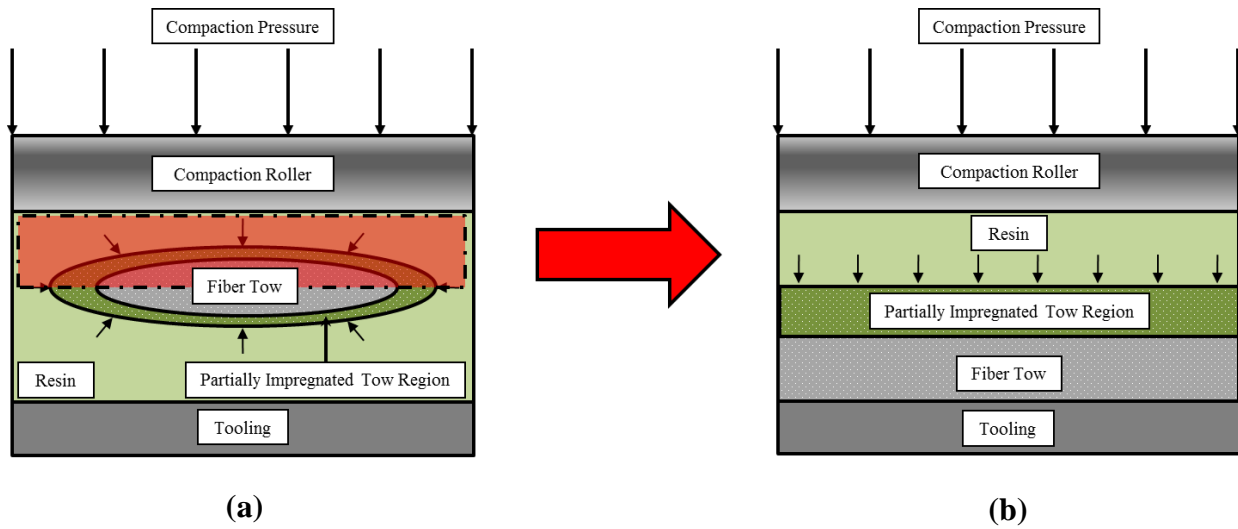
(a) **(b)**

Figure 40   Schematic and simplification of tape impregnation unit cell schematic: (a) original fiber tow unit cell model; (b) modified unit cell model

Many assumptions are made to simplify the modeling of the tape impregnation process. The tape deformation during phase 1 is neglected. Also, a linear pressure gradient assumed in region of the tow impregnated with the resin before the initiation of phase 2. The magnitude of this initial pressure is small and the depth of penetration is only a fraction of the initial preform thickness so linear pressure assumption is justifiable. The flow is modeled as one-dimensional flow through thickness. This is a reasonable assumption as the resin covers the entire surface of the tape on the outside as seen from Figure 2 and the roller moves in the thickness direction during compaction. The dry part of the preform is assumed to be stiff, due to the high tow speeds involved. In addition, the lubricated part of the impregnated tow visco-elasticity will be neglected. This is because the fiber volume fraction is assumed to be dependent only on the applied stress (applied to preform deformation). The following constitutive equation was cited by [12] to be suitable for describing the relationship between applied stress and fiber volume fraction,

$$v_f = v_{fo} + \left(v_{fmax} - v_{fo}\right)\tanh^n\left(\frac{p_{pref}}{p_{prefmax}m}\right) \tag{2.1}$$

where v_f is the fiber volume fraction, v_{fo} is initial fiber volume fraction, v_{fmax} is the maximum fiber volume fraction, p_{pref} is the applied tow pressure (e.g. compaction stress exhibited by the fiber tow), $p_{prefmax}$ is the maximum applied tow pressure, and m, n are empirical fitting parameters. Figure 41 displays sample compaction pressure curves based on equation (2.(2.1).
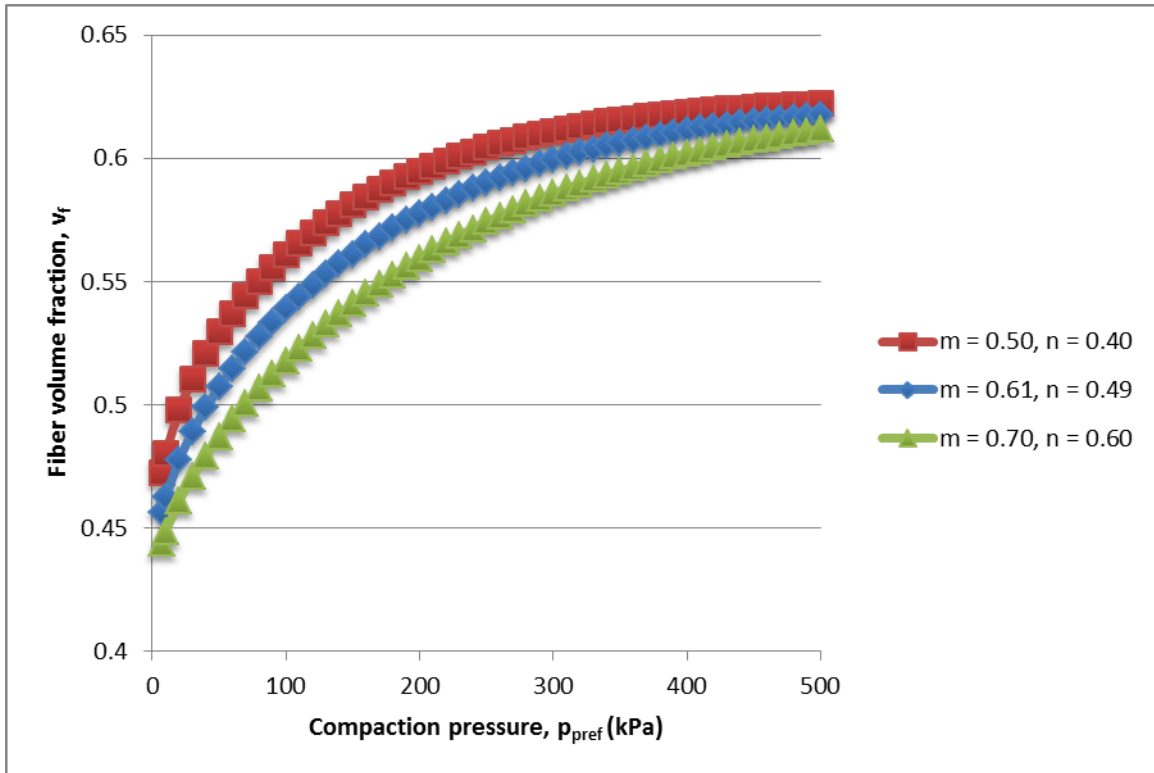
Figure 41   Compaction pressure curves based on equation [1]

Based on initial experimental work, it was found that the ideal empirical fitting parameters are at $m = 0.61$ and $n = 0.49$ to correlate with experimental results relating preform deformation and fiber volume fraction to applied pressure. Values were taken here with $v_{fo} = 0.425$, $v_{fmax} = 0.625$, and $P_{prefmax} = 500$ kPa. In addition, the Kozeny-Carman constitutive equation is assumed to describe the relationship of through thickness fiber permeability change with the fiber volume fraction of the tape as cited in [12, 14],

$$K_{zz}(v_f) = ko \frac{(1 - v_f)^3}{v_f^2} \tag{2.2}$$

where K_{zz} is through thickness (e.g. z-direction) permeability, v_f is the fiber volume fraction, and ko is the permeability coefficient. Here $ko = 5.8E\text{-}13$ m^2. The resin flow is assumed to follow Darcy's Law that describes the relationship between the flow rate and the pressure drop. Since the Reynolds number, Re <<1, the flow can be considered "quasi-steady" and the simulation can solve the steady state problem at each time step.

The primary physics that can be used to describe the resin flow through the porous tape unit cell region that is used within this work is Darcy's Law coupled with mass conservation of fluid elements under compaction. As noted in [12], once can find that at each time step,

$$\nabla \left(-\frac{K}{\eta} \cdot \nabla p \right) = -\frac{\partial \epsilon}{\partial t} \tag{2.3}$$

where ϵ is the volumetric strain, K is the tow fabric permeability, η is the resin viscosity, t is the process time, and p is the resin fluid pressure. Note it is assumed that the dry regions of the tow are much stiffer than the wetted regions of the tow and thereby do not influence the resin flow under the roller compaction force. Also, one can relate the fluid resin pressure (p) to the applied compaction pressure from the roller (p_{ap}) and the experienced compaction stress on the tow (p_{pref}) using the Terzaghi relation as found in [11, 15].

$$p_{pref} = p_{ap} - p \tag{2.4}$$

To simplify equation (2.(2.3)), once can rewrite the volumetric strain rate on the right hand side as follows,

$$\frac{\partial \epsilon}{\partial t} = \frac{\left(\frac{\partial \Delta V}{\partial t}\right)}{\Delta V} \tag{2.5}$$

with ΔV as an elementary volume. Since this model accounts for one-dimensional deformation of the tow elements, one can express the right hand side of equation (2.(2.5)) with the following,

$$\frac{\left(\frac{\partial \Delta V}{\partial t}\right)}{\Delta V} = \frac{\frac{\partial h}{\partial t}}{h_0} \tag{2.6}$$

where h is the tow element thickness and h_0 is the original thickness. Note that equation (2.(2.6)) serves as a linearized strain description of the tow. Since the volume of reinforcement within the tow is constant, the thickness change can be written with respect to fiber volume fraction.

$$h = \frac{h_0 v_{fo}}{v_f} \tag{2.7}$$

With this relationship, equation (2.(2.5)) can be written as the following result.

$$\frac{\partial \epsilon}{\partial t} = -\frac{v_{fo}}{v_f^2} \frac{\partial v_f}{\partial t} \tag{2.8}$$

Note one can rewrite the derivative of the fiber volume of fraction be a function of compaction pressure by using the chain rule.

$$\frac{\partial v_f}{\partial t} = \frac{\partial v_f}{\partial p_{pref}} \frac{\partial p_{pref}}{\partial t} \tag{2.9}$$

With this relationship, one can rewrite equation (2.2.8) as the following result.

$$\frac{\partial \epsilon}{\partial t} = -\frac{v_{fo}}{v_f^2} \frac{\partial v_f}{\partial p_{pref}} \frac{\partial p_{pref}}{\partial t} \tag{2.10}$$

Using a similar chain rule approach, one can arrive at an expression for the change in the tow permeability in the through thickness direction with relation to tow fiber volume fraction and compaction pressure.

$$\frac{\partial K_{zz}}{\partial z} = \frac{\partial K_{zz}}{\partial v_f}\frac{\partial v_f}{\partial p_{pref}}\frac{\partial p_{pref}}{\partial t}$$

(2.11)

Finally, for one dimensional through thickness resin flow (e.g. z-direction) in the fiber tow driven by the roller compaction pressure, one can rewrite equation (2.(2.3) using equations (2.2.10) and (2.2.11) to arrive at the following governing equation.

$$\frac{1}{\eta}\frac{\partial K_{zz}}{\partial v_f}\frac{\partial v_f}{\partial p_{pref}}\frac{\partial p_{pref}}{\partial z}\frac{\partial p}{\partial z} + \frac{K_{zz}}{\eta}\frac{\partial^2 p}{\partial z^2} = -\frac{v_{f0}}{v_f^2}\frac{\partial v_f}{\partial p_{pref}}\frac{\partial p_{pref}}{\partial t}$$

(2.12)

Equation (2.2.12) is a modified version of conventional Darcy's law that yields the resin pressure throughout the thickness of the tow as a function of fiber volume fraction, permeability, thickness, and time. To calculate the resin flow front progression with time through the depth of the tow, an expression can be determined based on the averaged velocity via Darcy's Law at the flow front position,

$$\frac{\partial L}{\partial t} = -\frac{(K_{zz})_{z=L}}{\eta \phi_{z=L}}\frac{\partial p}{\partial z}_{z=L}$$

(2.13)

where L is the flow front position or the resin penetration depth into the tow and ϕ is the porosity of the tow defined as $\phi = (1 - v_f)$. Note the subscript z=L implies values at the flow front position. Equations (2.2.12) and (2.2.13) are thus the two primary equations that the model solves to describe the physics of the tow unit cell roller compaction.

To solve the nonlinear governing equations, both equations (2.2.12) and (2.2.13) are solved numerically throughout the preform thickness and process time domains to generate the state of the tow after compaction, as detailed in [12]. The model generates information related to compaction of the tow unit cell and the dry tow space impregnated given a particular pressure profile. This allows one to perform parametric studies to evaluate the optimal processing parameters (e.g. compaction pressure profiles, tow speeds, etc.) to ensure nominal consolidation and impregnation of the tape during roller processing. To aid in this type of analysis, the governing equations have been adapted into a non-dimensional form. For this analysis, one can make the following non-dimensionalizations of dependent and independent variables of the governing equations,

$$\hat{L} = \frac{L}{H}$$

(2.14)

$$\hat{K}_{zz} = \frac{K_{zz}}{ko}$$

(2.15)

$$\hat{z} = \frac{z}{H}$$

(2.16)

$$\hat{t} = \frac{t}{t_c} \tag{2.17}$$

$$\hat{p} = 1 - \hat{p}_{pref} = \frac{p}{p_{ap}} \tag{2.18}$$

With H as the original tow thickness, t_c as the characteristic time, and other variables defined previously. With these non-dimensionalized variables, one can rewrite equation (2.2.12) in non-dimensional form.

$$\frac{kop_{ap}t_c}{v_{fo}\eta H^2} v_f^2 \left(-\frac{\partial \hat{K}_{zz}}{\partial v_f} \frac{\partial v_f}{\partial \hat{p}_{pref}} \left(\frac{\partial \hat{p}}{\partial \hat{z}}\right)^2 + \hat{K}_{zz} \frac{\partial^2 \hat{p}}{\partial \hat{z}^2} \right) = \frac{\partial \hat{p}}{\partial \hat{t}} \frac{\partial v_f}{\partial \hat{p}_{pref}} \tag{2.19}$$

Note one can choose a value of t_c such that the coefficient of the left hand side of the previous equation is made unity. With that, one can write t_c as the following result.

$$t_c = \frac{v_{fo}\eta H^2}{kop_{ap}} \tag{2.20}$$

One can now rewrite equation (2.2.12) into a simplified non-dimensional form using equations (2.(2.4), (2.2.19) and (2.2.20),

$$v_f^2 \left(-\hat{K}'_{zz} \left(\frac{\partial \hat{p}}{\partial \hat{z}}\right)^2 + \frac{\hat{K}_{zz}}{v'_f} \frac{\partial^2 \hat{p}}{\partial \hat{z}^2} \right) = \frac{\partial \hat{p}}{\partial \hat{t}} \tag{2.21}$$

with the following definitions:

$$\hat{K}'_{zz} = \frac{\partial \hat{K}_{zz}}{\partial v_f} = \frac{-3(1-v_f)^2 v_f - 2(1-v_f)^3}{v_f^3} \tag{2.22}$$

$$v'_f = \frac{\partial v_f}{\partial \hat{p}_{pref}} = \frac{(v_{fmax} - v_{f0})np_{ap}}{mp_{max}} \left(1 + \tanh^2\left(\frac{\hat{p}_{pref}p_{ap}}{mp_{max}}\right)\right) \left(\tanh\left(\frac{\hat{p}_{pref}p_{ap}}{mp_{max}}\right)\right)^{n-1} \tag{2.23}$$

Substitutions of the non-dimensionalized variables found in equations (2.2.14)-(2.2.18) coupled with equations (2.2.20) can yield a non-dimensionalized version of equation (2.2.13) to solve for the flow front position.

$$\frac{\partial \hat{L}}{\partial \hat{t}} = -\frac{(\hat{K}_{zz})_{z=L}}{\phi_{z=L}} \frac{\partial \hat{p}}{\partial \hat{z}_{z=L}} \tag{2.24}$$

The solver iterates with time and for each time step solves equation (2.2.21) for the resin pressure throughout the thickness domain of the tow. Note one can treat the tow impregnation problem as a steady state problem at each time step, since the problem is considered "quasi-steady" as mentioned previously. When this resin pressure is found, equation (2.2.24) advances the resin flow front with the next time step with the generated pressure information from the previous time step. For every time step increment, a new thickness mesh is generated with modified mesh spacing to reflect the change in tow deformation from the application of the

compaction roller. This process of iterating and solving both equations for pressure and flow front position continues until the end of the process time is reached. Details about the numerical analysis execution can be found in [22].

Unique to this work is the ability to supply arbitrary pressure profiles as functions of time. Previous work [22] has been limited to the application of constant pressure during processing for this type of analysis. Here, the roller tends to apply pressure in a parabolic or sinusoidal manner onto a given section of tape. Later results are based on a sinusoidal pressure profile of the following form.

$$P(t) = P_0 \sin(\omega t) = P_0 \sin\left(\frac{V}{R} t\right) \tag{2.25}$$

Here, P_0 is the initial compaction pressure, ω is the angular velocity of the roller, V is the tow speed of the roller, and R is the radius of the roller. Depending on the time scales involved, one may apply desired pressure profile to attain more accurate results. For example, high tow speed processing (e.g. V = 0.15 m/s) may be able to attain realistic results with the application of a constant pressure for a short time window that a section of tape is under the roller versus a parabolic pressure profile that may be more accurate for slower processing tow speeds and times (e.g. V = 0.015 m/s). The results that are generated and are of engineering interest from this analysis are the net displacement of the tow in the thickness direction, the wetted tow region distance through the tow thickness, the dry region distance through the tow thickness, the wetted and dry tow region fiber volume fraction and through thickness permeability. These results can be used to predict if processing conditions are optimum to ensure minimized defects by reducing the dry tow region sufficiently to eventually impregnate the remaining region during vacuum compaction and curing.

The presented model was run under sample parameters to evaluate its viability for realistic tape system geometries. Figure 42 shows a tape unit cell geometry schematic that serves as a sample representative tape cross section. Note values presented here are arbitrary but representative of sample tape placement system geometries. The schematic highlights an initial dry tow or void region characterized by the initial height, a_i and an initial overall tape height, h_i. It is important to note that the model is initialized with L_i, which is the initial impregnation depth into the dry tow. For this work, L_i is takes to be 1% of h_i.
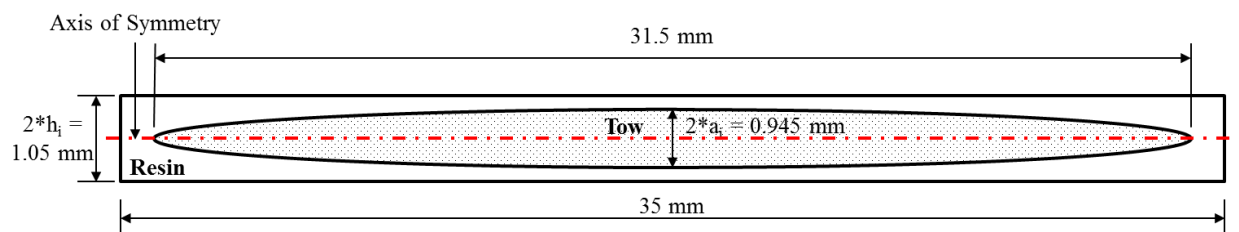

Figure 42   Tow unit cell initial sample geometry schemati

Figure 43 and Figure 44 display results of a parametric study performed with the presented model and the sample geometric inputs from Figure 42. The goal of the parametric study is to evaluate the degree of compaction and impregnation of the tow unit cell after the roller compaction cycle is completed. Here, the percentage reduction of the dry fiber region and percentage tow compaction results are presented with respect to tow speed for different cases

of initial compaction force. The results are presented in a non-dimensionalized manner for base comparisons between cases, with the void size non-dimensionalized with respect to the initial void size (a_i) and the tape size non-dimensionalized with respect to the initial tape height (h_i). Note, compaction forces are reported using their initial value of P_0 but are applied in a sinusoidal manner as shown in equation (2.2.25). Non-dimensionalized compaction time is taken with respect to the final compaction time, t_f.

The results show similar trends for both the percentage reduction of the dry fiber region and percentage tow compaction. The results indicate that as tow speed increases, the degree of compaction is reduced. This is due to the fact that a faster tow speed leads to a shorter time for consolidation and resin impregnation, thus leading to a lower degree of compaction after completion of the roller compaction cycle. This model allows for one to evaluate how tow speed can influence the degree of compaction and impregnation. Impregnation effects are characterized by reduction of the dry fiber region due to resin impregnation and fiber compaction. In addition, the model shows that by increasing the initial compaction force, one can achieve improved compaction overall. It is important to note that results become linear for higher tow speeds, but deviate non-linearly as tow speed decreases, with a threshold speed of approximately 0.1 m/s for this parametric study.
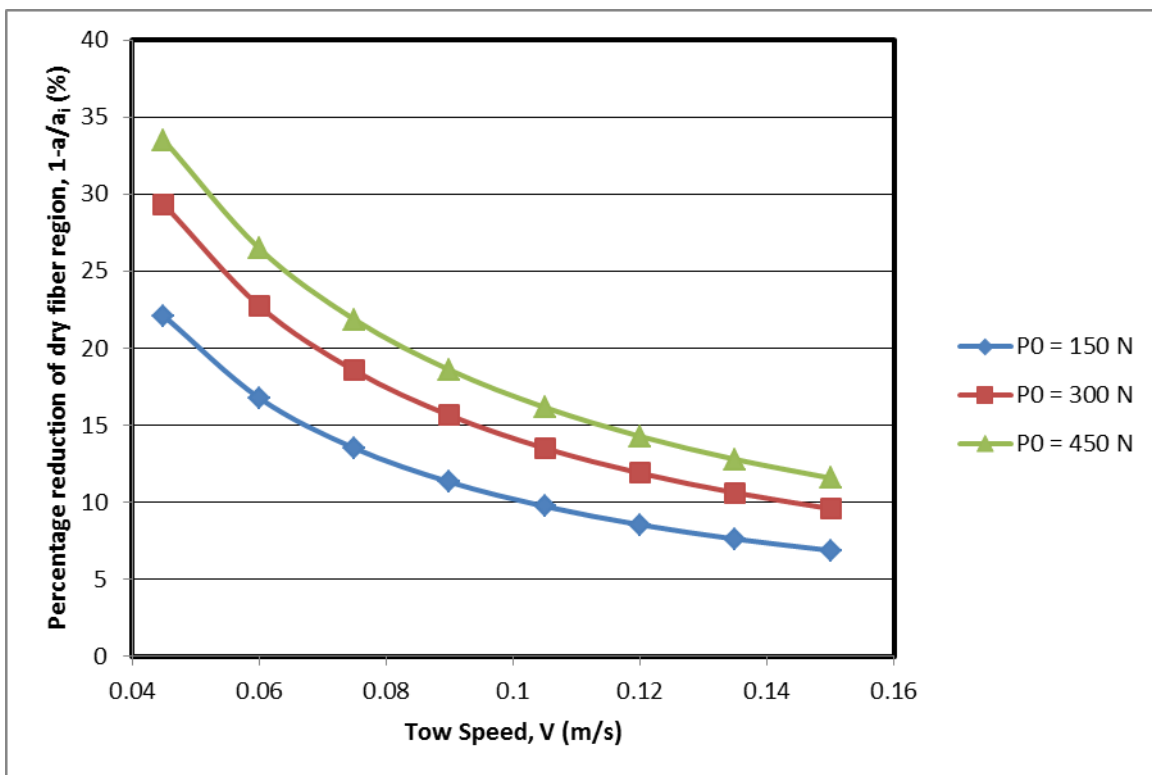

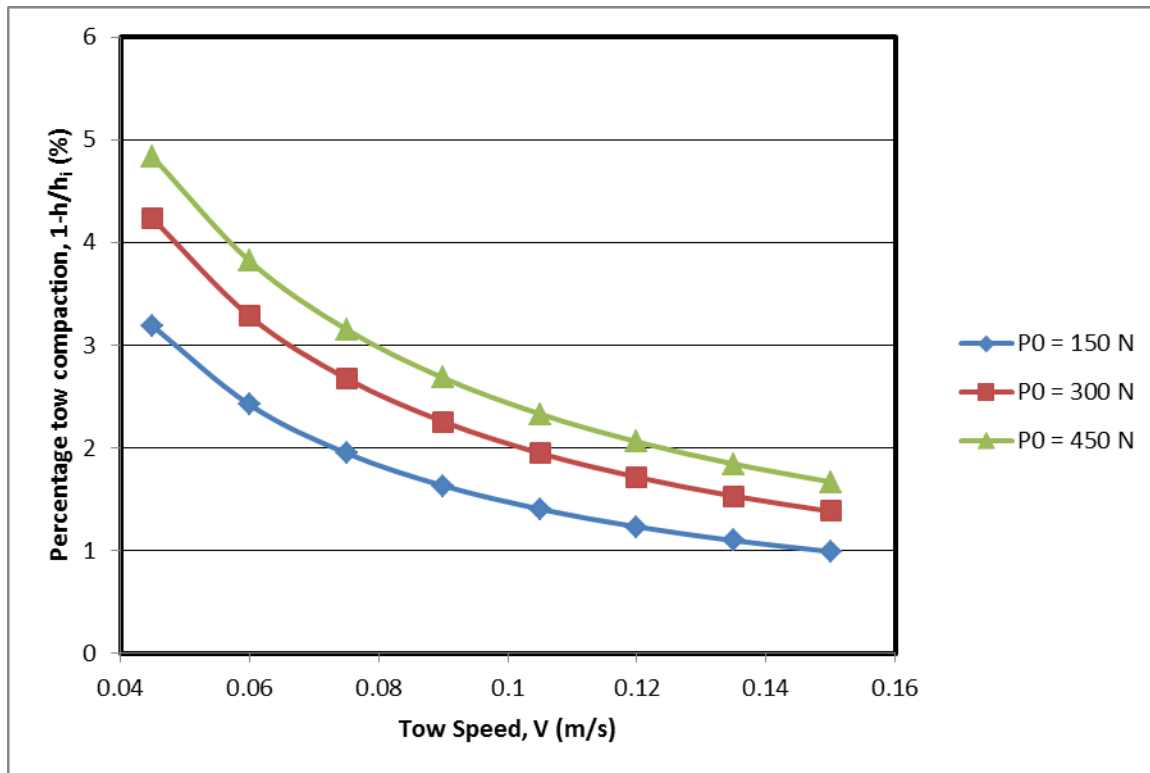Figure 43   Percentage reduction of dry fiber region at $t/t_f = 1$

Figure 44   Percentage tow compaction at $t/t_f = 1$

This threshold of linearity could be important for process engineering, as compaction and impregnation behaviors in the non-linear threshold of tow speed and compaction force may experience characteristic non-linear behaviors (e.g. visco-elasticity) when compared to processing at higher tow speeds within the linear region. Of further interest is that the effects of improved dry fiber and tow compaction with increased initial compaction force are reduced as one processes at higher tow speeds. This is characterized by the decreased spacing in between the different initial compaction force plots as tow speed is increased. This is important process as increase in compaction force by the roller may yield only marginal improvements in tape compaction and impregnation. The model allows one to explore the optimization of processing parameters to achieve the desired tape consolidation and impregnation state. Further parametric studies that can be performed are how changes in processing viscosity and fiber tow stiffness (e.g. m, n parameters from equation (2.(2.1)) are related to tow consolidation and impregnation as functions of compaction force and tow speed.

A process model has been presented that predicts the consolidation, impregnation, and tape dimensions of a partially impregnated thermoset prepreg tape during roller compaction. The model considers geometric, material, and process parameters with the goal of exploring the influence of process parameters on the final consolidated composite before curing. A parametric study has been performed to explore how changes in compaction force and tow speed impact the compaction and impregnation of the partially impregnated composite prepreg tape. The model is found to predict by how much a tow is consolidated and impregnated given an input pressure profile (e.g. sinusoidal pressure profile). Experimental verification and validation is necessary to ensure model outputs are consistent with real-life observations. The model will be compared to thermoset prepreg on-line consolidation processes to ensure validity. Future work

will seek to compare model accuracy and modifications will be made to optimize the model for thermoset composite material systems. Current work is exploring the implementation this model for not only roller processing but also vacuum bag compaction with a temperature ramp for the curing cycle.

Model 3: Tape Delamination

Tape delamination is a composites processing problem of research interest that the presented modeling can address. This problem arises within tape placement processing typically when one tape is placed on top of another tape and air is entrapped between the tapes. The research goal of this modeling is to determine a critical delamination gap height that would be filled with resin during the cure cycle. Also, this critical gap height would ensure designers that a delamination would not result after cure and it could be detected during processing inspection to take corrective action. Figure 45 displays a schematic of this model.
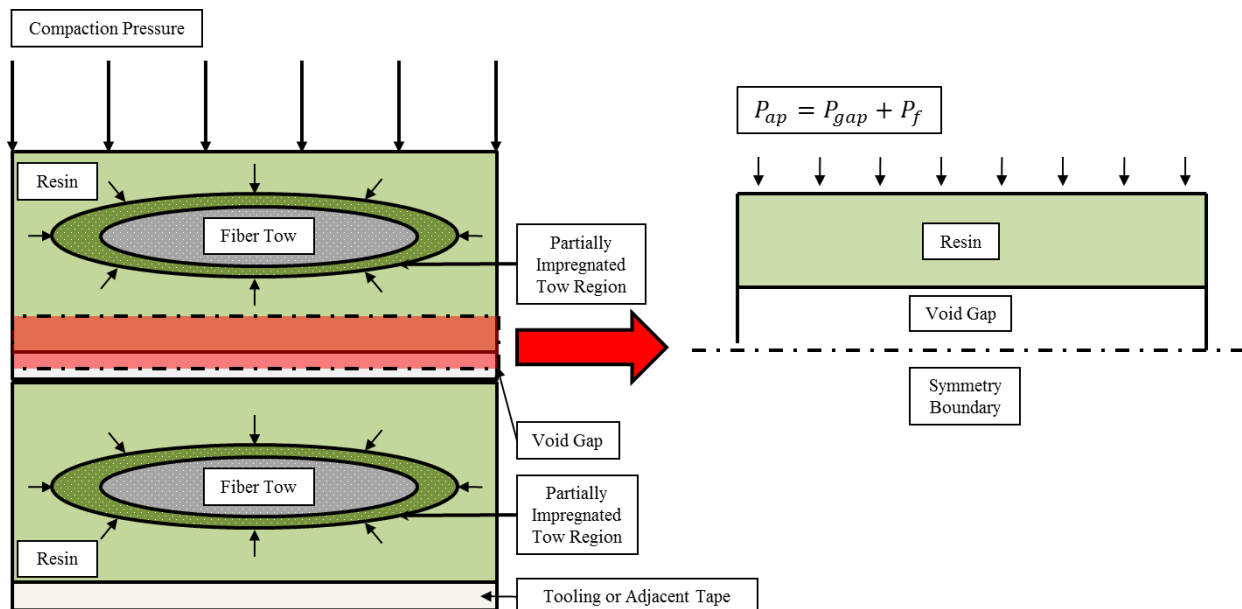

Figure 45   Tape delamination model schematic

The methodology for this model is based on an adaptation of the tape impregnation model, assuming the delamination air gap area is an idealized fabric preform of very high permeability and very low fiber volume fraction. One can run the tape impregnation model with parameters from the tape delamination model to find the thickness of the delamination of the gap after some time period with an applied pressure profile (e.g. sinusoidal, parabolic, constant, etc.). This is of engineering importance, because one can determine a critical tape delamination thickness within the green state that will permit for relief of the delamination from the composite upon a roller or vacuum compaction. One can also apply an internal delamination pressure for the void gap area, or it can be ignored for initial analysis. Also, one can account for tow presence with respect to the change in delamination height by applying resin pressure as a function of pressure losses from impregnating tows above the delamination. Work is in progress to develop the model and determine representative values to characterize critical delamination gap values

within the resin unit cell. Figure 46 and Figure 47 displays sample results for a sample unit cell with parameters identified in Table 6 **Initial model parameters**.

Table 6   Initial model parameters

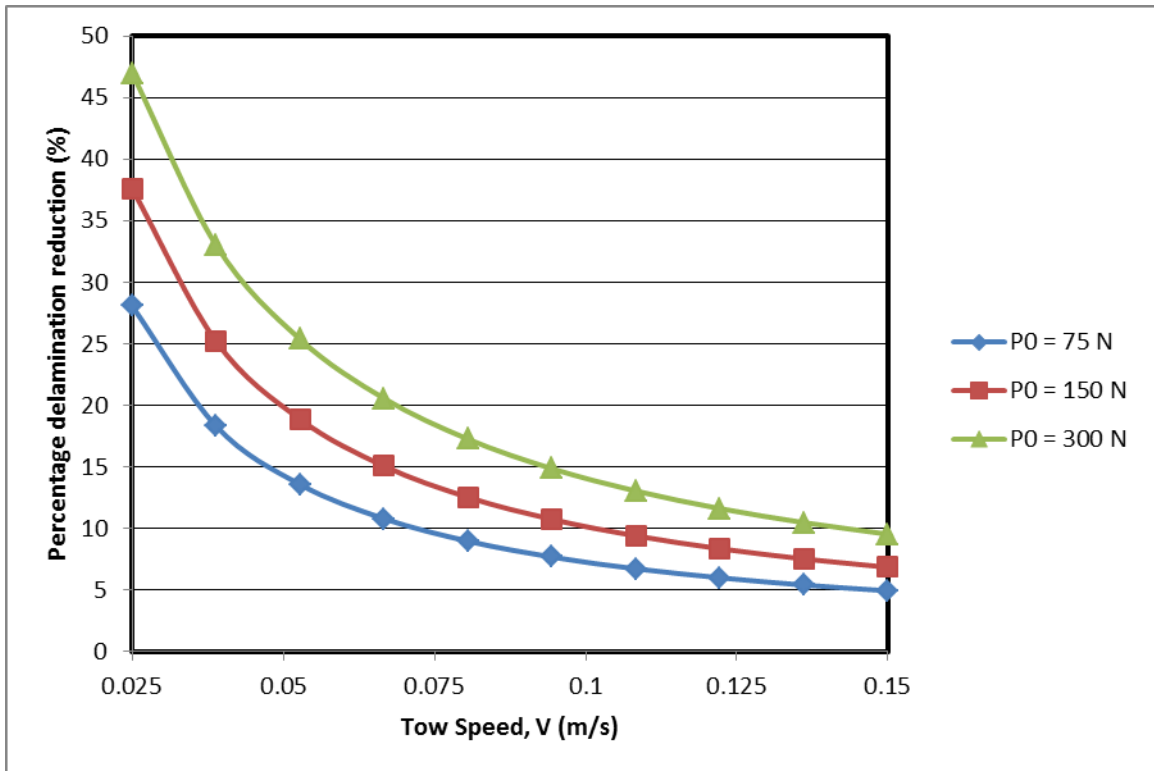|	
h_i (m)	4.73E-04
a_i (m)	4.68E-04
v_{fo}	0.425
K_{zz0} (m^2)	1.00E-7
η (Pa s)	28.5

Figure 46   Tape delamination results - percentage delamination reduction
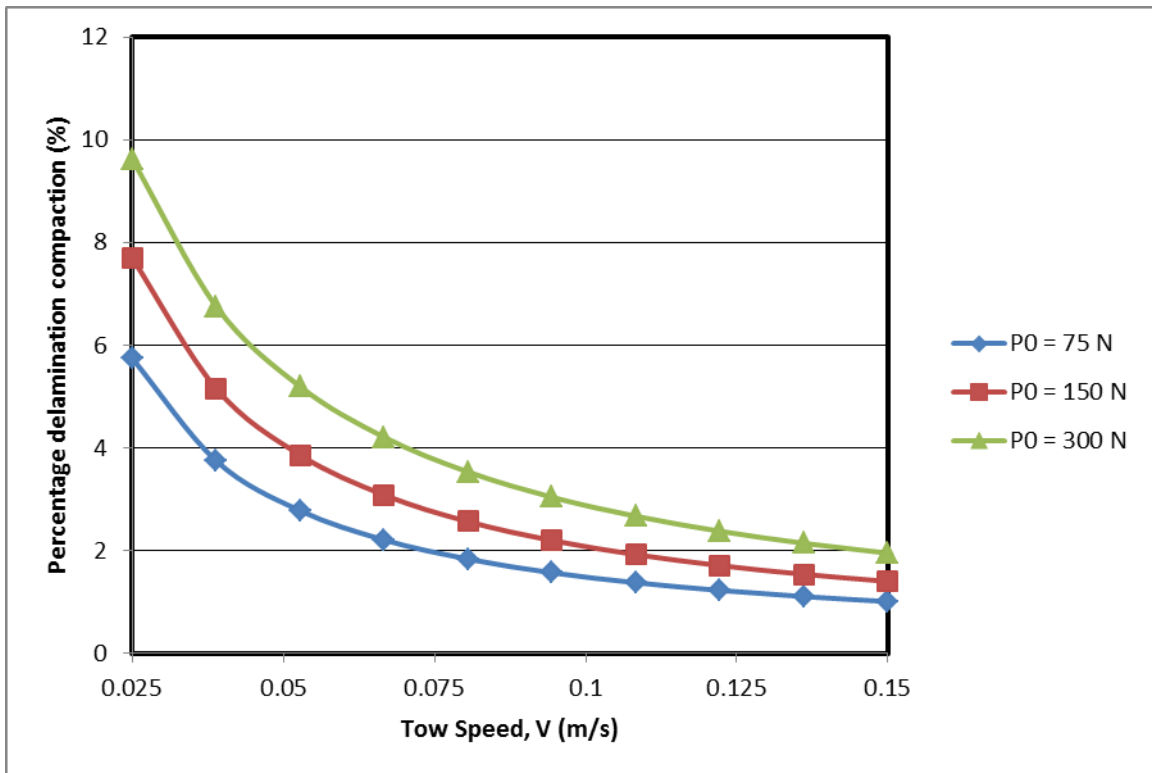
Figure 47   Tape delamination results - percentage delamination compaction

Here, parameters are defined as the following: initial resin + void gap height h_i, initial void gap height a_i, initial idealized fiber volume fraction of void gap v_{f0}, initial idealized permeability of void gap K_{zz0}, and resin viscosity η. Figure 46 displays a percentage delamination reduction as a function of tow speed V, for different initial compaction forces, P_0. Figure 47 displays a percentage delamination compaction, which includes the air gap and the resin that compresses the air gap during compaction. Here, the pressure profile was assumed sinusoidal to correlate with the act of the tape being compacted by the compaction roller.

The results show similar trends for both the percentage reduction of the air gap and percentage delamination compaction as in task 2. The results indicate that as tow speed increases, the degree of compaction is reduced. This is due to the fact that a faster tow speed leads to a shorter time for consolidation and resin impregnation for tows, thus leading to a lower degree of compaction after completion of the roller compaction cycle. This model allows for one to evaluate how tow speed can influence the degree of compaction and impregnation as seen in task 2. Impregnation effects are characterized by reduction in the dry fiber region from resin impregnation and fiber compaction. In addition, the model shows that by increasing the initial compaction force, one can achieve improved compaction overall.

It is important to note that results become linear for higher tow speeds, but deviate non-linearly as tow speed decreases, with a threshold speed of approximately 0.1 m/s for this parametric study. This threshold of linearity could be important for process engineering, as compaction and impregnation behaviors in the non-linear threshold of tow speed and compaction force may experience characteristic non-linear behaviors (e.g. visco-elasticity) when compared to processing at higher tow speeds within the linear region. Of further interest is that the effects of

improved dry fiber and tow compaction with increased initial compaction force are reduced as one processes at higher tow speeds. This is characterized by the decreased spacing in between the different initial compaction force plots as tow speed is increased. This is of important process engineering consideration, as increases in compaction force by the roller may yield only marginal improvements in tape compaction and impregnation. The model allows one to perform performance cost/benefit analysis for changes in processing parameters to optimize processing to achieve the desired tape consolidation and impregnation state.

Model 4: Tape Wrinkling

During prepreg placement on a tool surface, it is quite possible that a wrinkle may form due to improper lay up or poor prepreg tack or quality. Consecutive layers on top of the wrinkle will constrain this wrinkle when the entire structure is placed in a vacuum chamber at high temperature to cure the part. The goal of this paper is to determine the change in wrinkle radius embedded within the thermoset composite prepreg tape system during consolidation under vacuum. The system under investigation is based on unidirectional prepreg material. This is to ensure that the wrinkle can be compacted to a critical size such that is does not yield defects outside allowable tolerances that would compromise structural integrity after cure. The initial wrinkle radius can be measured with inspection. The model will determine the time needed to reduce the wrinkle radius to below a critical size that ensures defect free part after cure. Compaction can be applied with a selected pressure profile (e.g. sinusoidal, parabolic, constant, etc.) and the model will account for the elastic response of the resin/void boundary and consider the visco-elastic response of the resin.

A real wrinkle may be hemispherical but to simplify the geometry, consider a wrinkled prepreg ply (e.g. fibers + resin) which has a characteristic triangular domain with an effective aspect ratio, l/h as shown in Figure 48, where l is the characteristic length and h is the characteristic height. As schematically shown in Figure 48, the subsequent wrinkles on top of the primary wrinkle are assumed to decrease in wrinkle aspect ratio. It is idealized that after a certain layup thickness the wrinkling will be negligible. Note that the overall layup thickness is a function of the number of prepreg layers, N. The model will consider the extreme case in which the wrinkle originates in the bottom ply. We will characterize the horizontal and vertical displacement of the wrinkle as it is changes with an applied pressure, P_{ap}. Note the applied pressure can be a function of time as we assume a quasi-steady process and can be set to reflect roller compaction, vacuum compaction, or other compaction methods.
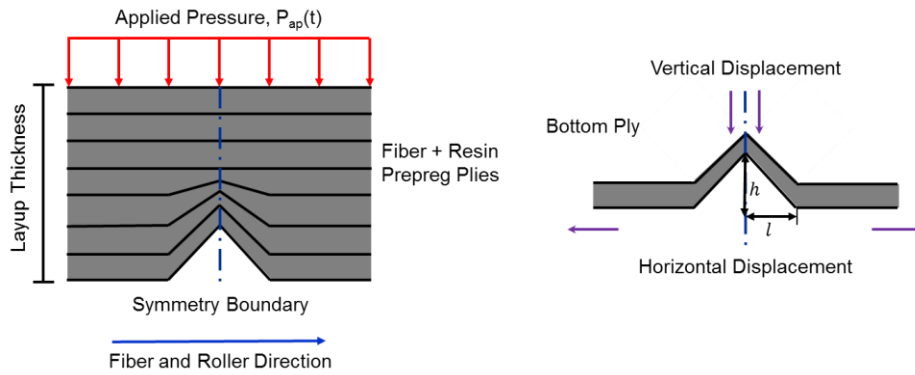
Figure 48   Schematic of simplified geometry to represent tape wrinkle

A model will be used to find $l(t)$ and $h(t)$ from applied pressure, P_{ap} and viscoelastic tape reactions. It will be assumed that the wrinkle comprises of linear elastic elements that are displaced by the applied pressure. It is assumed that the fibers within the prepreg plies do not buckle while under compaction as most of the tape is constrained by adjacent tapes to resist buckling. The no buckling assumption is reasonable for small displacements as is the case for this system; however, critical buckling loads can be evaluated later. For initial studies, a constant pressure will be applied to simulate uniform compaction.

Consider a wrinkled ply at a symmetric boundary as shown in Figure 49. This geometry represents the bottom ply of a prepreg layup. Based on trigonometric relations, one can resolve relations for $l, h, \dot{l}, \dot{h}$ as functions of θ as shown in the following equations:

$$l = L \cos(\theta) \overset{\frac{d}{dt}()}{\Longrightarrow} \dot{l} = -L \sin(\theta)\, \dot{\theta} \tag{4.1}$$

$$h = L \sin(\theta) \overset{\frac{d}{dt}()}{\Longrightarrow} \dot{h} = L \cos(\theta)\, \dot{\theta} \tag{4.2}$$

Note that $\dot{l}, \dot{h}$ are time derivatives of l, h. Also, the hypotenuse of the idealized triangular wrinkle is held constant. As pressure is applied to the top of the preform, it is supposed that the wrinkle height will decrease and the wrinkle length will increase with time. Once the kinematics of the problem are posed, one can address the dynamics to couple the wrinkle displacement with the resultant forces. An assumption will be made that inertial effects of the ply are negligible compared to viscous nature of the resin system. Figure 49 shows a free-body diagram of the symmetric ply system.
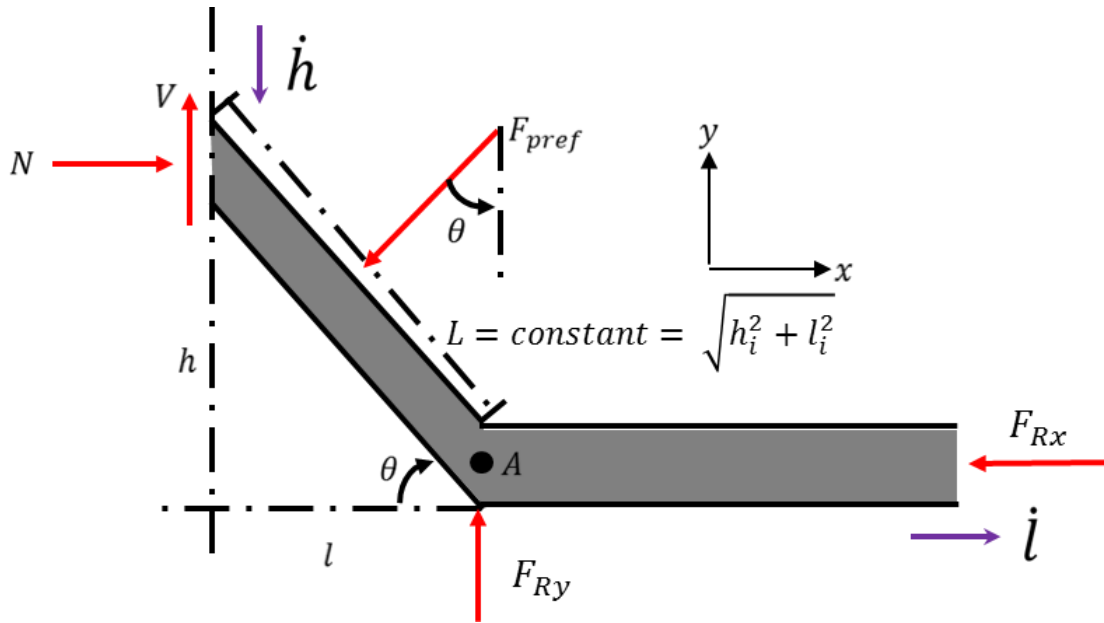
Figure 49   Kinematics and free body diagram of symmetric wrinkled ply for the bottom ply

Note that the applied pressure is applied to the angled area of the ply and results in an overall force on the preform labeled, F_{pref}. Since the system is a symmetric section, there is a resulting normal force, N, and resulting shear force, V, that comes from the internal reactions at the site of the section. Note the resulting shear force is equal to zero ($V = 0$), due to tape symmetry. The term F_{Rx} is the resultant viscous force that resists the tape-on-tape sliding inherent to the compaction of the wrinkle. The term F_{Ry} is the resultant support force acting at the bottom of the tape in the y-direction. One can resolve expressions for the normal and shear forces by force summation in the x and y directions as follows:

$$\sum F_x = 0 = N - F_{Rx} - F_{pref} \sin(\theta) \rightarrow N = F_{Rx} + F_{pref} \sin(\theta) \tag{4.3}$$

$$\sum F_y = 0 = V + F_{Ry} - F_{pref} \cos(\theta) \rightarrow F_{Ry} = F_{pref} \cos(\theta) \tag{4.4}$$

To resolve the governing equation of the system, one can take moments about point A (see Figure 49):

$$\sum M_A = 0 = -Nh + F_{pref}(L/2) \tag{4.5}$$

$$\rightarrow -F_{Rx}L \sin(\theta) - F_{pref}L \sin^2(\theta) + F_{pref}(L/2) = 0 \tag{4.6}$$

The result after substitution of the normal and shear force from equations (4.3) and (4.4) into the governing moment equation (6) with $\theta(t)$ is:

$$F_{Rx} = F_{pref} \frac{1 - 2\sin^2(\theta)}{2\sin(\theta)} \tag{4.7}$$

To account for material deformation, it is necessary to formulate a constitutive relationship that describes the material behavior. The first constitutive relationship will be designed to derive the reaction force from the viscous tape-on-tape sliding that resist compaction from the wetted plies. The relationship will be based on a two-parameter Voigt type spring-damper mechanical system that will represent the prepreg behavior as shown in Figure 50 below.
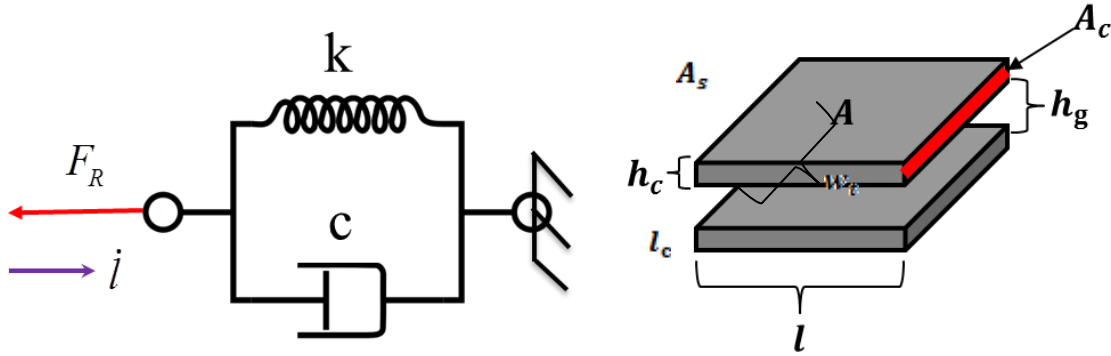

Figure 50   Two-parameter Voigt model and tape geometry definitions

Note, one can resolve and effective spring constant and an effective damping constant for the system with the following relationships:

$$\text{Effective spring constant, } k = E_{eff} A_c / l_c \tag{4.8}$$

$$\text{Effective damping constant, } c = \eta A_s / h_g \tag{4.9}$$

Note E_{eff} is the effective fiber modulus, A_c is the cross section area of the ply, l_c is the effective tape length, η is the resin viscosity, A_s is the contact area of the tape-on-tape sliding, h_c is the ply thickness, and h_g is the approximate resin gap between two plies of prepreg (see Figure 50). The spring constant relationship for the effective spring constant is derived from the spring constant relationship for elastic rod elements (e.g. effective fibers). The damping constant relationship for the effective damping constant is derived from the damping constant relationship for relative motion between parallel surfaces separated by a viscous fluid gap (e.g. tape-on-tape sliding). The overall viscoelastic reaction force can thus be written as follows:

$$F_{Rx} = k\,(l - l_i) + c\dot{l}(t) \tag{4.10}$$

A second constitutive relationship is necessary to approximate the through thickness distribution of the applied stress on the wrinkle. Note that although the pressure is applied to the top of the layup as P_{ap}, the wrinkle is actually compacted from the pressure that is distributed at the wrinkle directly located at bottom of the prepreg stack. It is understood that if the layup consists of a single layer of prepreg ($N = 1$), then the $P_{pref} = P_{ap}$; however, if there were an infinite number of layers of

prepreg ($N = \infty$), then $P_{pref} = 0$ or the wrinkle would not be able to experience the driving pressure to compact since it is too far away from the applied pressure location.

The following relation is used to characterize this distribution of pressure through the thickness of the layup to the wrinkle that matches the prescribed boundary conditions:

$$P_{pref} = \frac{P_{ap}}{N} \tag{4.11}$$

For the model, one needs to resolve the force on the wrinkle rather than the pressure. The force on the wrinkle can be resolved as follows:

$$F_{pref} = P_{pref} w_t L = \frac{P_{ap} w_t L}{N} \tag{4.12}$$

Note that if the model proves to be too inaccurate in its predictions of wrinkle state after compaction, the constitutive relations can be modified to be more physical if necessary to improve model accuracy.

After the establishment of the constitutive relations, one can resolve the governing equation of the system as an ODE for $\theta(t)$ by substitution of the constitutive relations into the governing moment equation (equation (4.7)) to yield the following:

$$c\dot{l}(t) + k(l - l_i) = F_{pref} \frac{1 - 2\sin^2(\theta)}{2\sin(\theta)} \tag{4.13}$$

Rearrangement of results and substitution of equation (4.1) leads to an ODE in $\theta(t)$,

$$\dot{\theta}(t) = \frac{d\theta}{dt} = \frac{k}{c}\left(\frac{\cos(\theta) - \cos(\theta_i)}{\sin(\theta)}\right) - \frac{F_{pref}}{cL}\left(\frac{1 - 2\sin^2(\theta)}{2\sin^2(\theta)}\right) \tag{4.14}$$

Substitution for k and c with equations (4.8) and (4.9) in equation (4.14) yields,

$$\dot{\theta}(t) = \frac{d\theta}{dt} = \frac{E_{eff}A_c h_g}{l_c \eta A_s}\left(\frac{\cos(\theta) - \cos(\theta_i)}{\sin(\theta)}\right) - \frac{F_{pref} h_g}{\eta A_s L}\left(\frac{1 - 2\sin^2(\theta)}{2\sin^2(\theta)}\right) \tag{4.15}$$

Or after further substitutions for F_{pref}, A_s and A_c from equation (4.12) and understanding that $A_s = w_t l_c$ and $A_c = w_t h_c$,

$$\dot{\theta}(t) = \frac{d\theta}{dt} = \frac{E_{eff} h_c h_g}{\eta l_c^2}\left(\frac{\cos(\theta) - \cos(\theta_i)}{\sin(\theta)}\right) - \frac{P_{ap} h_g}{N l_c \eta}\left(\frac{1 - 2\sin^2(\theta)}{2\sin^2(\theta)}\right) \tag{4.16}$$

The governing equation (4.16) will have to be integrated numerically due to non-linearity to resolve $\theta(t)$. Note the first term of the RHS of equation (4.16) represents the wrinkle's resistive response to the driving compaction represented by the second term of the RHS of equation (4.16). To resolve $l(t)$ and $h(t)$, one can apply equations (4.1) and (4.2) using $\theta(t)$. A convenient way to

express changes in wrinkle height and area is the non-dimensionalized wrinkle area, based on twice the area of the triangular domain (from symmetry of the characteristic triangular domain), with the following

$$Nondimnesionalized\ wrinkle\ area = \frac{l\ h}{l_i\ h_i} = \frac{\sin(2\theta)}{\sin(2\theta_i)}$$ (4.17)

At steady state or when $d\theta/dt = 0$, equation (16) reduces to

$$\frac{2\sin(\theta)}{1 - 2\sin^2(\theta)}(\cos(\theta) - \cos(\theta_i)) = \frac{P_{ap}\ l_c}{N\ E_{eff}\ h_c}$$ (4.18)

This equation shows what process parameters are primarily important for the overall final state of the wrinkle if the time window available was large. For such cases, the wrinkle angle is only dependent on the effective fiber stiffness, applied compaction pressure, number of layers present. The geometric parameters that are important are the initial wrinkle angle, ply thickness, and overall tape length. The right hand side of equation (4.18) provides a nondimensional wrinkle compaction parameter that will be used in parametric studies later to provide insight in wrinkle shrinkage behavior.

Table **7** displays sample inputs for the model representative of a typical carbon / epoxy prepreg used for automated tape placement systems. Note grayed values indicate calculated parameters and whited values indicate selected values.

Figure 51 displays results as predicted by the model using the parameters listed in Table 7. Results are reported with respect to nondimensionalized wrinkle area, which is defined in equation (4.17). These are plotted with respect to nondimensionalized time defined as t/t_f, Note t_f represents the final compaction time. It was chosen at 2.0 seconds for this parametric study to be representative of a typical roller process and to allow visualization of the steady state results properly (i.e. to show convergence). The results show that one can shrink the wrinkle to a limited extent. For example the percentage area reduction of the initial wrinkle is approximately to 65% the original area for the material and processing conditions listed in Table 7. The fiber stiffness and viscous reactions counter the compaction force with time and will influence the shrinkage of the wrinkle. Parametric studies are presented in a non dimensionalized manner to allow us to understand the scaling issue.

Table 7   Sample inputs for process model

Geometric Parameters:		
Tape length	l_c (m)	1.22E+00
Tape width	w_t (m)	6.99E-02
Ply thickness	h_c (m)	1.05E-03
Wrinkle initial length	l_i (m)	3.49E-03
Wrinkle aspect ratio	$l_i/h_i =$	8
Wrinkle initial height	h_i (m)	4.37E-04
Wrinkle hypotenuse	L (m)	3.52E-03
Total wrinkle contact area	A_{tot} (m^2)	8.54E-02

| Wrinkle compaction area	A (m^2)	2.46E-04
Process Parameters:		
Final compaction time	t_f (s)	2.00
Spring Constant Data:		
Effective fiber stiffness	E_{eff} (Pa)	2.31E+09
Ply cross sectional area	A_c (m^2)	7.33E-05
Effective spring constant	k (kg/s^2)	1.39E+05
Damping Constant:		
Resin viscosity	η_{resin} (Pa s)	2.85E+01
Resin gap height	h_g (m)	5.25E-05
Tape sliding area	A_s (m^2)	8.52E-02
Effective damping constant	c (kg/s)	4.62E+04
Compaction Force:		
Applied compaction pressure	P_{ap} (Pa)	-7.60E+04
Applied pressure on wrinkle	P_{pref} (Pa)	-9.50E+03
Number of plies	N	8
Applied force on wrinkle	F_{pref} (N)	-2.34E+00
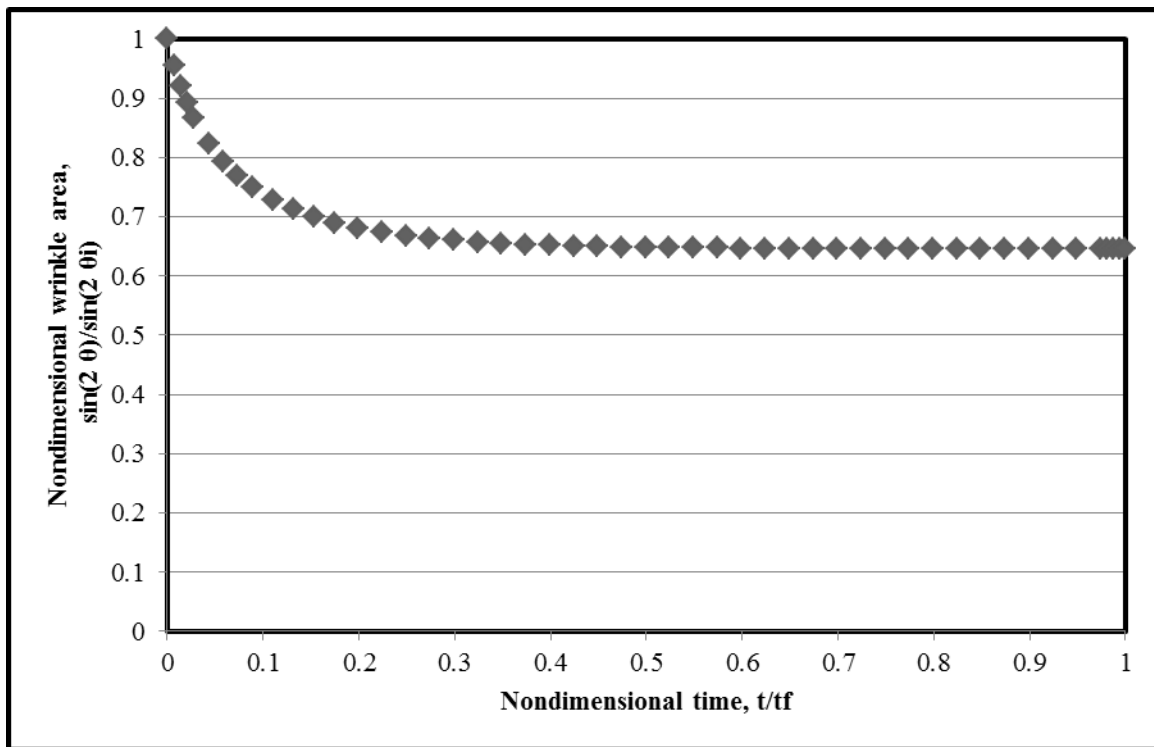
Figure 51   Results showing reduction in wrinkle area for input values listed in Table **4** Parametric Study

A parametric study has been performed to identify important process and material parameters and their effect on wrinkle compaction. The parametric study was conducted using MATLAB to solve equation (4.16) and then analyze the results with respect to the nondimensional wrinkle compaction term identified by the RHS of equation (4.18) which we will refer to as the compaction

number. Figure 52 displays results for the nondimensionalized wrinkle area for different values of
the nondimensional wrinkle compaction term. The results demonstrate that increase of the wrinkle
compaction number increases the wrinkle shrinkage. The compaction number can be increased by
increasing the applied load or the tape width or by reducing the ply thickness or if the fibers have
less effective stiffness. Also the shrinkage will reduce as the wrinkled ply is buried further into the
consolidated layers. Also note higher the compaction number, longer it takes to achieve the steady
state. The change in wrinkle compaction is non-linear with compaction number as shown in Figure
53. Future work will require a quantitative comparison of the model to experimental observations
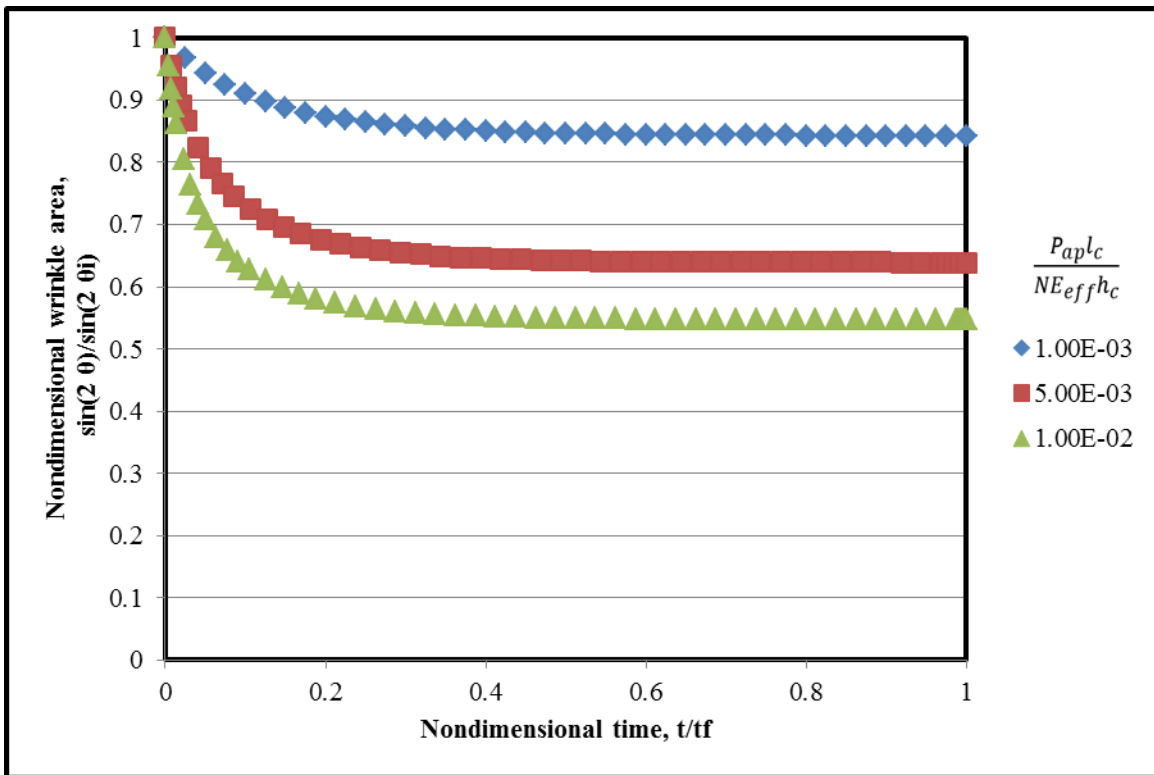for verification and validation of the model.

Figure 52   Parametric study of wrinkle compaction number with nondimensional wrinkle area
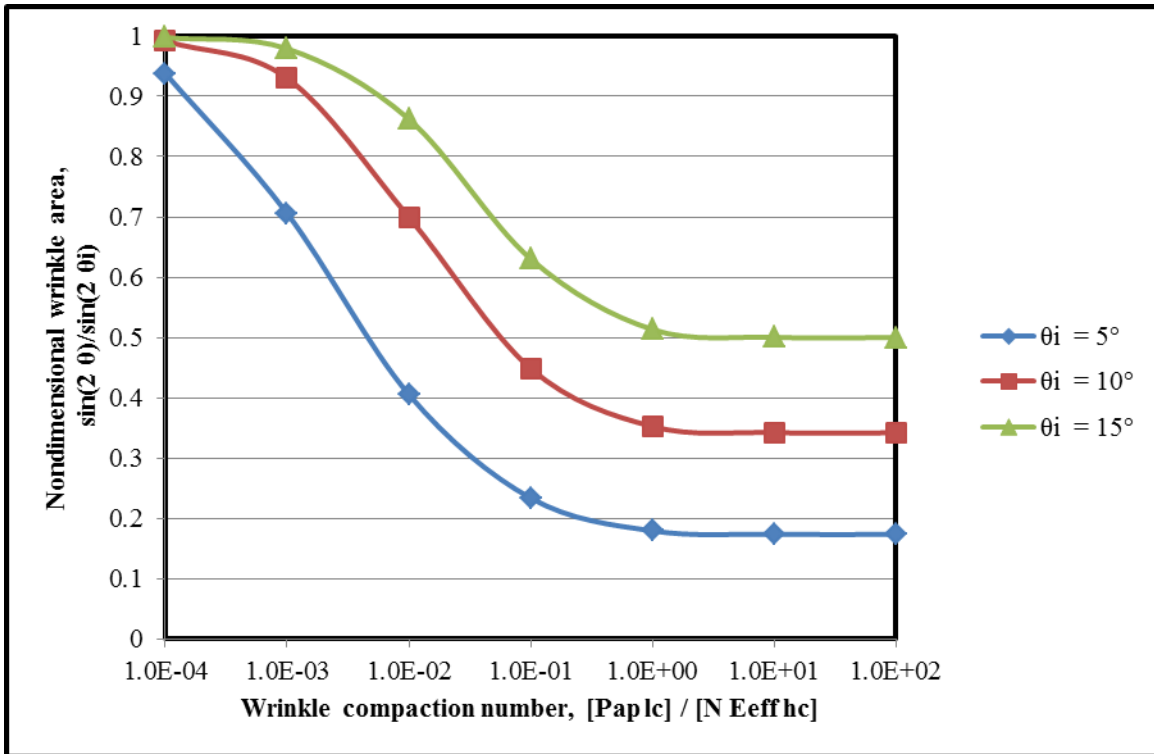
Figure 53   Effect of wrinkle compaction number on nondimensional wrinkle area at steady state ($t/t_f = 1$) with respect to θ_i

A process model has been presented that models the compaction of a trapped wrinkle in an uncured composite thermoset prepreg material, consisting of fibers and resin, being subjected to compaction by a pressure boundary condition in the presence of other layers. The model approximates a typical wrinkle as a triangular geometry with a characteristic height, length, and angle. The model uses constitutive relations to account for viscous reactions and through thickness pressure distribution on the wrinkle as a function of layup thickness. The governing equation is an ODE that was solved numerically. Results have been presented with typical processing parameters for carbon/epoxy tapes, including a sample parametric study. The results provide designers insight into the degree of compaction one can achieve with given process and prepreg parameters. The compaction seems to be non-linear and increases with increase in the wrinkle compaction number and with initial wrinkle orientation. Future work is required to verify and validate the model with experimental observations.

Process Model Integration

Figure 54 describes the process modeling organization for the thermoset tape roller compaction problem as described by GE Global Research. The first step is the definition of the initial tape state. This definition is based on initial inspection of the tape geometry (e.g. overall height, wet region height, dry region height), material properties (e.g. permeability, fiber volume fraction), and processing parameters (e.g. applied pressure, tow speed, resin viscosity) taken of the tape before processing. The next step is to model the tape compaction roller, where the tape geometry model (task 1) model is run. Models run under the tape compaction roller process phase are characterized by sinusoidal or parabolic applied pressure profiles. This model uses the output of the previous tape infusion step as input to capture the geometric changes in the tape cross section (e.g. height, width). Since the tape impregnation model is 1D with respect to height, the width change physics are captured with this model. The tape geometry, material properties, and processing parameters from the previous tape infusion step are run as inputs for the tape impregnation model under the compaction roller, with the change in width captured via a reduced available resin for infusion within the tape impregnation model (e.g. resin "smear" effect). In parallel, the tape delamination model (task 3) model is run with the tape impregnation model to determine the change in delamination geometry under the compaction roller. The next step is to run the tape impregnation and tape delamination models again under vacuum consolidation pressure conditions (e.g. constant vacuum pressure) using the outputs from the models from the compaction roller as inputs for the vacuum consolidation phase. After the conclusion of this step, the tape reaches the final tape state.
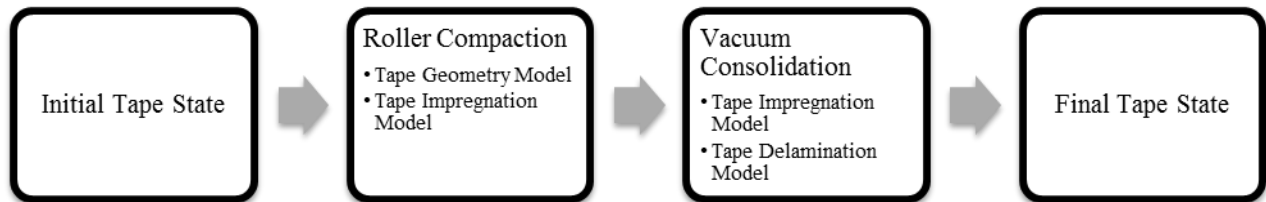

Figure 54   Process model integration flow chart

Table V and Figures 29 & 30 show results from a sample run of the integrated process model. Table V displays the thicknesses of the dry fiber, wet fiber, and resin layer regions of the tape after roller and vacuum compaction. Figure 29 displays the distribution of the wet fiber and dry fiber regions of the tape after roller compaction with respect to the fiber preform pressure, fiber volume fraction, and through thickness permeability. Similarly, Figure 30 displays the distribution of the wet fiber and dry fiber regions after the vacuum compaction with respect to the fiber preform pressure, fiber volume fraction, and through thickness permeability.
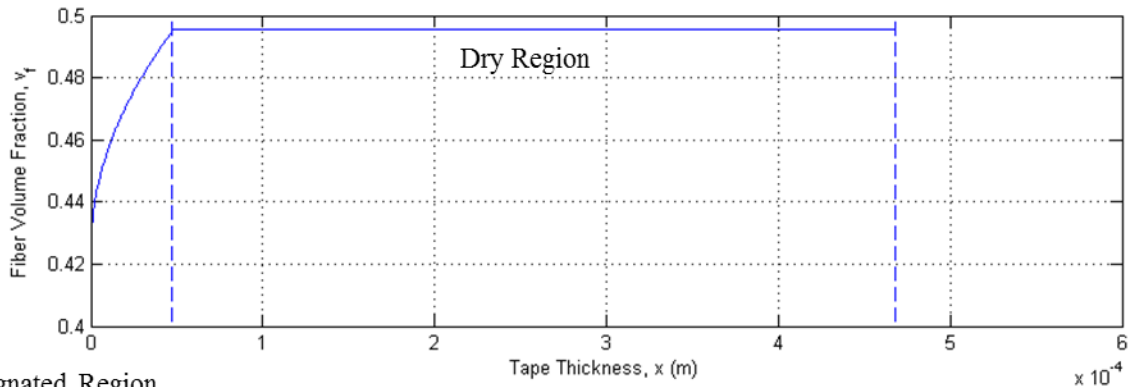
Table 8   Results of integrated model at P0 = 150 N, V = 0.1 m/s, η_{roller}=10 Pa s, η_{vac} = 1000 Pa s, L_i = 0.1 h

Process Stage	Dry Fiber Thickness (m)	Wet Fiber Thickness (m)	Resin Thickness (m)	Total Thickness (m)
Initial	4.725E-04	4.725E-05	5.250E-05	5.250E-04
Roller	4.204E-04	4.740E-05	5.779E-05	5.256E-04
Vacuum	1.568E-04	2.321E-04	1.357E-08	3.889E-04

Impregnated Region
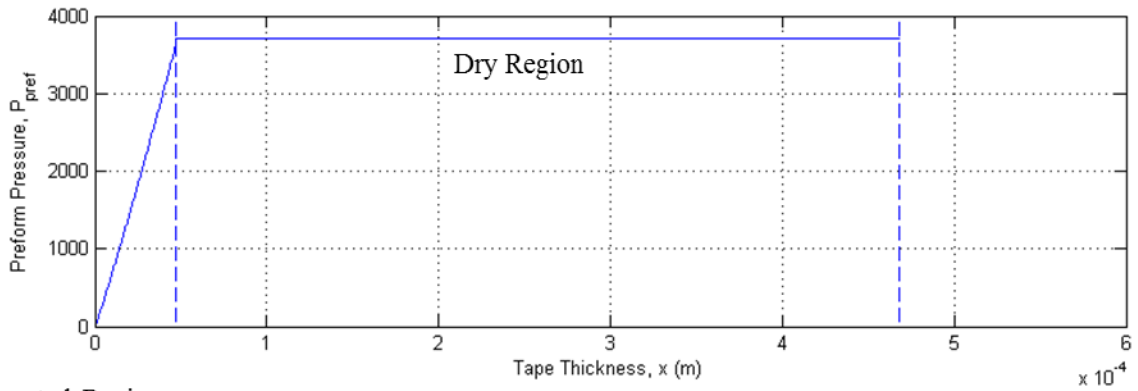
Impregnated Region

Impregnated Region
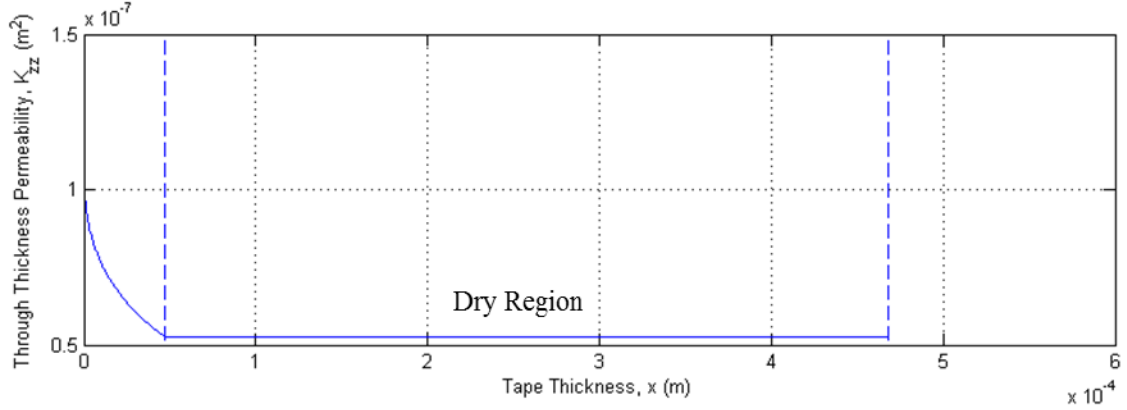
Tape Top   Tape Bottom

Figure 55   Tape state after roller compaction at P0 = 150 N, V = 0.1 m/s, η_{roller}=10 Pa s, η_{vac} = 1000 Pa s, L_i = 0.1 h
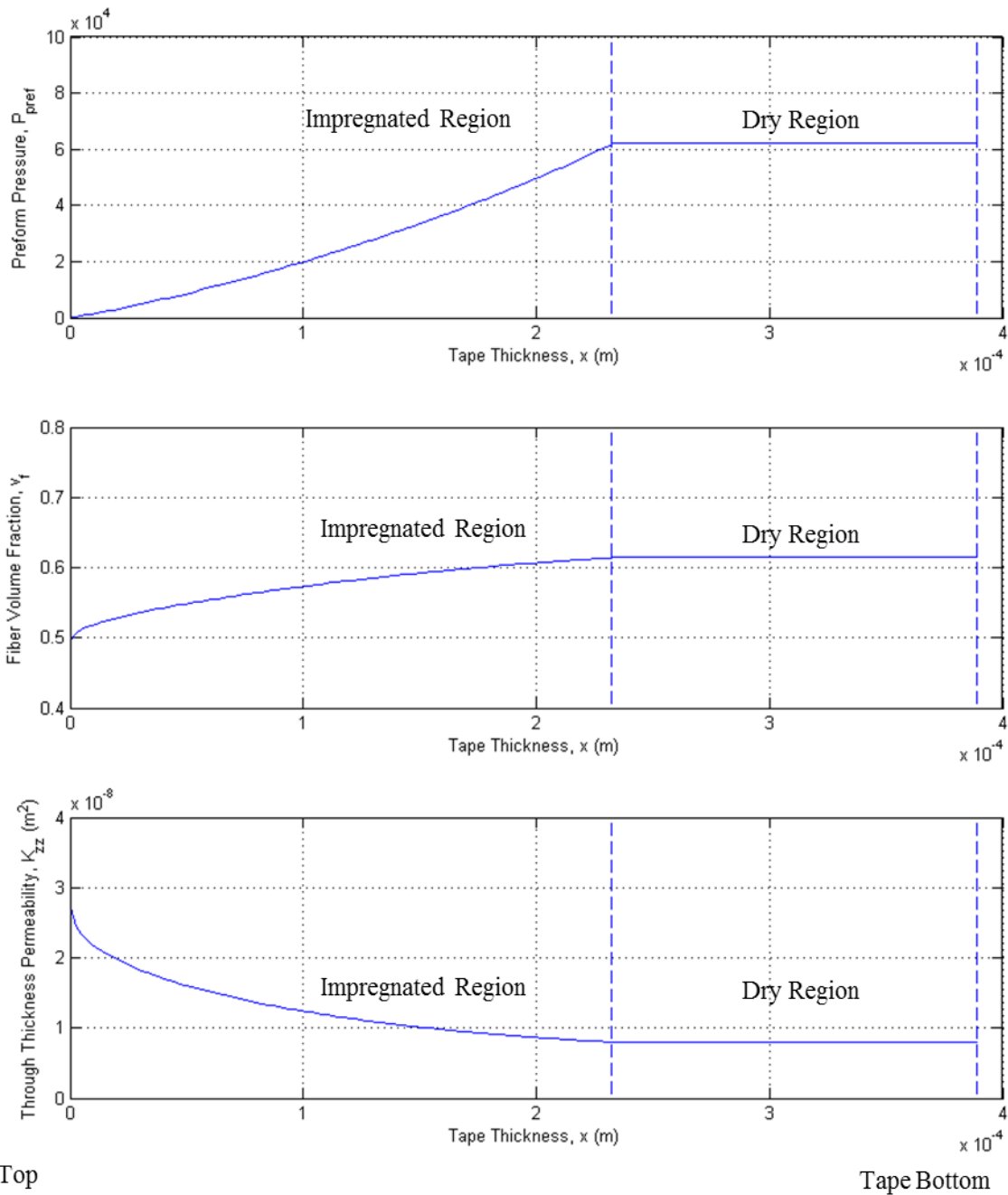
Figure 56   Tape state after roller and vacuum compaction at P0 = 150 N, V = 0.1 m/s, η_{roller}=10 Pa s, η_{vac} = 1000 Pa s, L_i = 0.1 h

The results show a decrease in the dry fiber thickness with a corresponding increase in the wet fiber thickness with each processing step. This corresponds to the tape becoming infused after running the roller and vacuum processing stages. In addition, the overall tape thickness (wet + dry fibers) is reduced. Note, the compaction time for the roller step is a function of the tow speed V, while the compaction for the vacuum was taken at t = 300 seconds or 5 min. This was to simulate initial debulking of the prepreg before the layup is exposed to temperature changes. The figures also show the distribution of preform pressure, fiber volume fraction, and through thickness permeability broken down for the wet and dry regions of the tape. This is of interest for understanding how the process parameters evolve with each process step, for which the model can provide detail.

Of interest is the observed increase in the resin layer thickness after the roller compaction and elimination of the resin layer after vacuum compaction. The increase in the resin layer is hypothesized to be a result of a "bounce back" in the tape after the roller compaction step that had been observed during processing. The uniform compaction by vacuum for significantly longer time scales forces the resin into the dry fibers. The larger time scale for vacuum compaction gives enough time for the resin to "work into" the dry fibers and eliminates the resin layer. The short roller time scale does not give enough time for the resin to work itself into the tape and thus there is enough dry fiber to resist overall tape compaction.

Appended to the report is a series of process maps that show the evolution of the tape after roller and vacuum compaction with varying process parameters. The parameters that were chosen for the process maps are applied pressure (P_{ap}), tow speed (V), resin viscosity (η), and initial resin impregnation distance (L_i). Note, figures similar to Figures 29 and 30 can be generated for each combination of process map parameters. The process maps can be used to gauge the influence of process parameter changes on the overall thickness and the degree of infusion for the roller and vacuum stages of processing.

Experimental Verification and Validation

In order to ensure proper validation of the model, it is necessary to experimentally verify the model outputs. Each model contains material constitutive relations that need to be experimentally verified for accuracy to GE materials. Results presented in this report used material constitutive values that are experienced by typical unidirectional carbon fiber –epoxy resin composites; however, validation will be necessary to compare presented results with GE materials. Table **9** displays parameters with respect to the models they are used in to be verified.

Table 9   Parameters to be verified by experiment

Model	Parameters to be Verified	Symbol
Tape Geometry	volume fraction of compressed voids	v_{fo}
Tape Impregnation	permeability coefficient	k_o
Tape Delamination	idealized fiber volume fraction of void gap	v_{fo}
Tape Wrinkling	effective fiber modulus/effective tape length	E_{eff}/l_c

For the tape geometry model, if void physics is to be taken into account, one must determine a particular volume fraction of voids present in the tape after roller compaction. This can be evaluated by taking tape samples after rolling and freezing them such that their void content can be determined under a microscope after sectioning. For the tape impregnation model, one must determine the permeability coefficient and ensure that it is accurate for the unidirectional carbon fiber and epoxy resin used in the process. This can be determined by performing through thickness permeability experiments in conjunction to the measurement of applied pressure with respect to fiber volume fraction. Permeability values at a given applied pressure can be plotted against fiber volume fraction values at that same applied pressure. One can measure the curve fit from these results to get a measurement of the permeability coefficient. For the tape delamination model, one must determine an idealized fiber volume fraction of the void gap. Since the gap in empty of fibers in reality, one must assign a permeability value to the model that leads to a best match with experimental observations for a given gap size if one wants to extrapolate results for model runs with unknown gap sizes. For the tape wrinkling model, one must determine an effective fiber modulus divided by effective tape length to capture the elastic reactions of tape-on-tape sliding. The experiment would involve sliding a tape in between two separate tapes with a known compaction force and known sliding driving force in the axial fiber direction. The tapes would be positioned in a lap joint configuration so that proper tape-on-tape sliding in captured and permitting the ends of each tape to be connected to force measurement equipment. Keeping track of the force versus displacement can allow one to determine the effective fiber modulus and also determine the effective tape length where the fibers resist axial displacement without buckling. It is important to constrain the tape such that buckling is minimized (i.e. laterally from the fiber direction). Proper verification of the material parameters will assist in the validation process of the model for application.

Summary and Conclusions

A series of process models has been presented that seek to address the problem of online consolidation of thermoset prepreg tapes. The models are based on adaptations of conventional process models used for composites manufacturing. The provided models provide a theoretical framework in addition to example solutions from given material and process parameters provided by GE. The results show that for each modeling problem, one can evaluate the state of the tape during processing as a function of material and processing parameters. The models can be linked together to simulate the physics of the tape in the real process. Future work will involve verification and validation of the models and corresponding materials constitutive relationships employed throughout. Additional future work will involve the integration of temperature and degree of cure physics into the modeling framework to provide further insight into the composite processing problem.

REFERENCES

1. H.M. Hsiao, I.M. Daniel. Effect of fiber waviness on stiffness and strength reduction of unidirectional composites under compressive loading. Composites Science and Technology, 1996, Vol. 56 (5), pp. 581-593.
2. C. S. Yerramalli, A. M. Waas. The Effect of Fiber Diameter on the Compressive Strength of Composites - A 3D Finite Element Based Study. Computer Modeling in Science and Engineering, 2004, VOL 6; NUMB 1, pages 1-16.
3. J.F. Mandell, D.D. Samborsky, L. Wang. Effects of fiber waviness on composites for wind turbine blades, Int. SAMPE symposium, 2003.
4. I.M. Daniel, H.M. Hsiao. Is there a thickness effect on compressive strength of unnotched composite laminates? International Journal of Fracture, 1999, Vol. 95, pp. 143-158.
5. J. Lee, C. Soutis. Thickness effect on the compressive strength of T800/924C carbon fibre–epoxy laminates. Composites: Part A, 2005, Vol. 36, pp. 213-227.
6. S.H. Ward, H. Razi. Effect of thickness on the compression residual strength of notched carbon fiber/epoxy composites. 28th International SAMPE Technical Conference, 1996.
7. E.T. Camponeschi. Compression testing of thick-section composite materials. Composite materials: fatigue and fracture (third volume), ASTM STP 1110. Philadelphia, PA: American Society for Testing and Materials, 1991, pp. 439-456.
8. H.M. Hsiao, I.M. Daniel, S.C. Wooh. A new compression test method for thick composites. Journal of Composite Materials, 1995, Vol. 29 (13), pp. 1789-1806.
9. H.J. Garala. Experimental evaluation of graphite/epoxy composite cylinders subjected to external hydrostatic compressive loading. Proceedings of the Spring Conference on Experimental Mechanics, 1987, Society for Experimental Mechanics, Bethel, CT, pp. 948-951.
10. P.Z. Bazant, J.H. Kim, I.M. Daniel, B.G. Emilie, G. Zi. Size effect on compression strength of fibre composites failing by kink band propagation. International Journal of Fracture, 1999, Vol. 95(1-4), pp. 103-141.

11. Advani S. G. & Sozer E. M., *Process Modeling in Composites Manufacturing*, New York: Marcel Dekker, Inc., 2003.

12. Merotte J., Simacek P. & Advani S.G. "Resin flow analysis with fiber preform deformation in through thickness direction during Compression Resin Transfer Molding." *Composites Part A: Applied Science and Manufacturing* 41(7) (2010): 881-887.

13. Merotte J, Simacek P & Advani S.G. "Flow analysis during compression of partially impregnated fiber preform under controlled force." *Composites Science and Technology*. 70(5) (2010): 725-733.

14. Carman P. "Fluid flow through granular beds." *Trans Inst Chem Eng.* 15 (1937): 150-66.

15. Terzaghi K. & Peck R.B. *Soil Mechanics in engineering practice.* 2nd Ed. New York: Joh Wiely & Sons, 1967.

16. Bhat P., Merotte J., Simacek P. & Advani SG. "Process analysis of compression resin transfer molding." *Composites Part A: Applied Science and Manufacturing* 40(4) (2009): 431-441.

17. *Li M., Gu Y., Zhang Z. and Sun Z. "A Simple Method for the Measurement of Compaction and Corresponding Transverse Permeability of Composite Prepregs."* Materials Science*. (2007*